



UNIVERSIDADE D  
COIMBRA

Andreia Filipa de Moura Fernandes

STUDIES ON SECONDARY  
SCINTILLATION FROM XENON  
ADMIXTURES WITH HELIUM

PhD thesis in Physics Engineering, in the field of Instrumentation,  
performed under scientific guidance of Doutora Cristina Maria Bernardes  
Monteiro and Doutor Carlos Alberto de Oliveira Henriques, presented to  
the Physics Department of the Faculty of Sciences and Technology of the  
University of Coimbra

December 2020



UNIVERSIDADE DE COIMBRA  
FACULDADE DE CIÊNCIAS E TECNOLOGIA  
DEPARTAMENTO DE FÍSICA

STUDIES ON SECONDARY SCINTILLATION FROM  
XENON ADMIXTURES WITH HELIUM

Andreia Filipa de Moura Fernandes

*PhD thesis in Physics Engineering, in the field of Instrumentation, performed under scientific guidance of Doutora Cristina Maria Bernardes Monteiro and Doutor Carlos Alberto de Oliveira Henriques, presented to the Physics Department of the Faculty of Sciences and Technology of the University of Coimbra*



UNIVERSIDADE D  
COIMBRA



Coimbra, December 2020



## Acknowledgements

I would like to express my deep gratitude to Doutora **Cristina Monteiro**, my research supervisor, for her patient guidance, enthusiastic encouragement and useful critiques of this work, as well as to Doutor **Carlos Henriques**, my research co-supervisor, for his valuable and constructive suggestions during the planning and development of this work, for his friendship, availability and patience. His willingness to give his time so generously has been very much appreciated.

I would also like to thank Professor **Joaquim Santos**, for his advice and assistance in keeping my progress, and for so generously teach me and help me with the data analysis and the whole experimental campaign as well. My grateful thanks are also extended to Doutor **Luís Fernandes** who accompanied me for a long time, for his support and availability.

My special thanks are extended to NEXT, specially to Professor **Juan José Gomez-Cadenas** for the opportunity given so I could work on this project and be part of the amazing team that NEXT Collaboration is. The assistance provided by Doutor **Carlos Azevedo** was greatly appreciated.

I would also like to extend my thanks to the technicians of GIAN department, Doutor **Fernando Amaro**, Doutora **Elisabete Freitas** for their help in offering me the resources in running the program. I wish to acknowledge the help provided by **Daniel Mano** and **Pedro Silva**, I'm really grateful for their contribution, knowledge sharing and for making me feel part of this team since the very first day.

I would like to offer my deep gratitude to Lieutenant Colonel **Rui Rocha** for allowing me some time to work on this project and mainly for not doubt me and my abilities to successfully fulfil my mission.

I am particularly grateful for the advice given by **Rodrigo Cardoso** and Lieutenant **João Ramos**, who accompanied me and gave me the strength I needed in the most critical moments.

To **Liliana Rebelo** for her unconditional friendship, **Mariana Jaloto**, a wonderful person, and 2<sup>nd</sup> Lieutenant **Rita Amaral**, the most amazing girls I've met so far, who have been a great help in this whole journey. A sincere acknowledge to **Diogo Bastos**, **Felipe Trenk**, **Manuel Garrido** and 2<sup>nd</sup> Lieutenant **Fábio Simões**, for their friendship and willingness for help whenever they could.

Finally, I wish to thank my parents, **Teresa Fernandes** and **Messias Fernandes** for their support and encouragement throughout this journey, for always being present at their own way. And my brother **Paulo Fernandes** for inspiring me every single day and mainly for have not doubted me, allowing me to get here. I hope to make you all proud.



## Abstract

High Pressure Time Projection Chambers (HP-TPC) based on secondary scintillation, also called electroluminescence (EL) signal amplification are being proposed for rare event detection, such as directional dark matter search, double electron capture and double beta decay detection. In the last few years, the Neutrino Experiment with a Xenon-based TPC (NEXT) has been developing its technology, achieving an energy resolution  $< 1\%$  FWHM at the  $Q_{\beta\beta}$  of the double beta decay of  $^{136}\text{Xe}$ , 2458 keV. The good energy resolution, the use of the event topology reconstruction for improved background suppression and the possibility to scale up to larger masses are the main strengths for the success of this experiment.

The discrimination of the rare event through its topological signature of primary ionisation trails is a major asset for this type of TPC when compared to liquid or double phase TPCs. However, it is limited mainly by the high electron diffusion in pure xenon. In order to overcome this limitation, some studies have been performed with the addition of sub-percent concentrations of molecular species to xenon in order to reduce the electron diffusion. From the studied species,  $\text{CH}_4$  appears to be a good candidate, since it allows to achieve a good energy resolution, as well as a good electron cooling efficiency. Nevertheless, the continuity of studies with additives to be used with xenon, to decrease the electron diffusion, has a primordial importance for this experiment.

Recently, simulation studies have shown that helium can also be a potential candidate for reducing the electron diffusion in xenon-based mixtures. Therefore, the use of helium as an additive to pure xenon has been assessed, since its characteristics as a noble gas are a major advantage, e.g. in terms of gas purification and, in opposition to xenon admixtures with molecular additives, where the high quenching of xenon excited states and dissociative electron attachment induced by some molecular species will not occur in helium. Therefore, the EL output of xenon-helium mixtures is expected to be similar as that of pure xenon. Thus, the helium admixtures with xenon might be an attractive solution to significantly reduce the electron diffusion and improve the discrimination efficiency of these optical TPCs.

Experimental studies of the impact of helium addition to xenon on the gas EL yield and on the respective EL statistical fluctuations have not yet been carried out, being, thus, of great importance to investigate these issues. In this work, the electroluminescence yield of Xe-He mixtures in the range of 0 to 30 % helium is investigated. The impact of helium addition on the gas EL output is demonstrated to be small and its impact on the EL statistical fluctuations has been found to be negligible, within the experimental uncertainties.

The EL yield is reduced by  $\sim 2\%$ ,  $3\%$ ,  $6\%$  and  $10\%$  for  $10\%$ ,  $15\%$ ,  $20\%$  and  $30\%$  of helium concentration, respectively, for a typical reduced electric field of  $2.5 \text{ kV/cm/bar}$  in the scintillation region. This decrease is lower than had been anticipated by the most recent simulation data presented in the literature. Furthermore, it was demonstrated that the energy resolution remains unchanged, relative to that obtained in pure xenon. Nevertheless, there is a disadvantage with the TPC operation at higher pressures having more than  $10\text{-}20\%$  helium concentrations, because the amount of xenon available as source of neutrinoless double beta decay will be reduced, in contrast to the addition of sub-percent levels of molecular additives, where the amount of xenon remains the same, an issue that will also be discussed in the present work.

The present PhD project will have impact on the choice of the NEXT-100 detector technology and, in addition, its relevance goes beyond NEXT, being of relevance to any HPXe optical TPC where the reduction of electron diffusion is of significant importance. Moreover, the present results are a main benchmark for the simulation tools to be applied to future optical TPCs based on Xe-He mixtures.

**Keywords:** Gas Scintillation Proportional Counter, secondary scintillation, helium, Time Projection Chamber, electron diffusion, Xe scintillation, optical HPXe TPC, Xe additives, Neutrinoless double beta decay, rare event detection.

## Resumo

As câmaras de projeção temporal de alta pressão (HP-TPC) baseadas em cintilação secundária, também chamada de sinal de amplificação por eletroluminescência (EL) têm sido propostas para detecção de eventos raros, tais como pesquisas sobre matéria negra direcional, decaimento por dupla captura de elétrons, e detecção do decaimento beta duplo. Nos últimos anos, a colaboração NEXT (Neutrino Experiment with a Xenon TPC) tem vindo a desenvolver a sua tecnologia baseada num HP-TPC, tendo já atingido uma resolução em energia  $< 1\%$  FWHM para a energia,  $Q_{\beta\beta}$ , do decaimento beta duplo do  $^{136}\text{Xe}$ , 2458 keV. A boa resolução em energia, a utilização da reconstrução topológica dos eventos para uma supressão de fundo e a possibilidade de escalar para grandes massas são os principais pontos fortes para o sucesso desta experiência.

A discriminação dos eventos raros através da sua assinatura topológica do rasto da ionização primária é um grande trunfo para este tipo de TPC, quando comparado com TPCs de fase líquida ou dupla. Contudo, esta discriminação está limitada principalmente pela elevada difusão de elétrons em xénon puro. De forma a ultrapassar esta limitação, têm sido realizados alguns estudos com adição ao xénon de espécies moleculares com concentrações sub-percentuais, de forma a reduzir a difusão de elétrons. Das espécies moleculares estudadas, o  $\text{CH}_4$  parece ser um bom candidato, uma vez que permite a obtenção de uma boa resolução em energia, assim como uma boa eficiência no arrefecimento dos elétrons. Não obstante, a continuação dos estudos com aditivos a ser usados com xénon para reduzir a difusão de elétrons tem uma importância primordial para esta experiência.

Recentemente, estudos de simulação têm mostrado que o hélio pode ser um potencial candidato para reduzir a difusão de elétrons em misturas baseadas em xénon. Portanto, a utilização do hélio como aditivo ao xénon puro tem vindo a ser avaliada, já que as suas características como gás nobre são uma grande vantagem, e.g. em termos de purificação do gás, e em oposição às misturas de xénon com aditivos moleculares, onde os efeitos de inibição dos estados excitados de xénon e perda de elétrons induzidos por espécies moleculares não vão ocorrer em hélio. Portanto, é expectável que o resultado de eletroluminescência das misturas de xénon-hélio seja semelhante ao do xénon puro. Por conseguinte, as misturas de hélio com xénon podem ser uma solução atrativa para reduzir significativamente a difusão de elétrons e melhorar a eficiência de discriminação destas TPCs óticas.

Estudos experimentais do impacto da adição de hélio ao xénon no rendimento de eletroluminescência do gás e nas respetivas flutuações estatísticas da eletroluminescência ainda não foram realizados, sendo, desta

maneira, de grande importância para a investigação destas questões. Neste trabalho, o rendimento de eletroluminescência de misturas de Xe-He é investigado para hélio em quantidades de 0 a 30 %. É demonstrado que o impacto da adição de hélio no resultado da eletroluminescência no gás é pequeno e o seu impacto nas flutuações estatísticas de eletroluminescência foi igualmente demonstrado ser insignificante, dentro das incertezas experimentais.

O rendimento de eletroluminescência é reduzido em ~2%, 3%, 6% e 10% para concentrações de hélio de 10%, 15%, 20% e 30%, respectivamente, e para um campo elétrico reduzido típico de 2.5 kV/cm/bar na região de cintilação. Esta diminuição é menor do que tinha sido antecipado pelos dados mais recentes de simulações apresentados na literatura. Além disso, ficou demonstrado que a resolução em energia se mantém inalterada, relativamente àquela obtida em xénon puro. Não obstante, existe uma desvantagem com a operação de uma HP-TPC contendo hélio em concentrações de 10-20 %, porque a quantidade de xénon disponível como fonte do decaimento beta duplo sem emissão de neutrinos vai ser menor, em contraste com a adição a nível sub-percentual de aditivos moleculares, onde a quantidade de xénon se mantém igual, um problema que também será discutido no presente trabalho.

O presente projeto de doutoramento terá impacto na escolha da tecnologia do detetor NEXT-100 e, além disso, a sua relevância vai além do NEXT, sendo de relevância para qualquer TPC ótico de xénon de alta pressão, onde a redução da difusão de eletrões tem uma importância significativa. Além disso, os presentes resultados são uma marca de referência importante para ferramentas de simulação a ser aplicadas em futuras TPCs óticas baseadas em misturas de Xe-He.

**Keywords:** Contador gasoso de cintilação proporcional, cintilação secundária, hélio, Câmara de projeção temporal, difusão de eletrões, cintilação em xénon, TPC ótica de xénon a alta pressão, aditivos para Xe, decaimento beta duplo sem emissão de neutrinos, deteção de eventos raros.

# Contents

<b>Acknowledgements</b>	<b>i</b>
<b>Abstract</b>	<b>iii</b>
<b>Resumo</b>	<b>v</b>
<b>Nomenclature</b>	<b>ix</b>
<b>1 Introduction</b>	<b>1</b>
<b>2 Neutrinoless double beta decay</b>	<b>9</b>
2.1 Majorana neutrinos . . . . .	9
2.2 Neutrinoless double beta decay . . . . .	9
2.3 Current experiments on double beta decay studies . . . . .	10
<b>3 The NEXT Experiment</b>	<b>15</b>
3.1 The NEXT experiment roadmap . . . . .	15
3.1.1 The NEXT detector . . . . .	16
3.1.2 Background . . . . .	20
3.2 Topological signature . . . . .	22
3.2.1 Limitations in the tracking plane . . . . .	24
3.3 Topology reconstruction . . . . .	24
3.3.1 NEXT prototypes results . . . . .	25
3.4 Electron diffusion . . . . .	27
3.5 Molecular additives . . . . .	29
3.5.1 Scintillation with molecular additives . . . . .	30
3.5.2 Previous studies with molecular additives . . . . .	31
<b>4 Electroluminescence in noble gases</b>	<b>37</b>
4.1 Primary scintillation . . . . .	37
4.2 Secondary scintillation . . . . .	38
4.2.1 Electroluminescence yield . . . . .	39
4.3 Energy resolution . . . . .	40
<b>5 Helium</b>	<b>45</b>
5.1 Previous studies with helium . . . . .	46
5.1.1 Diffusion . . . . .	46
5.1.2 Drift velocity . . . . .	50
5.1.3 Energy resolution . . . . .	50
5.1.4 Primary scintillation . . . . .	51
5.1.5 Electroluminescence yield . . . . .	51
<b>6 Experimental setup and methodology</b>	<b>53</b>

6.1	Experimental setup . . . . .	53
6.1.1	Gas mixture system . . . . .	55
6.2	Experimental methodology . . . . .	56
6.2.1	Gas mixing procedure . . . . .	56
6.2.2	Data taking and analysis methodology . . . . .	57
6.2.3	Waveform analysis methodology . . . . .	59
<b>7</b>	<b>Experimental results: validation of the experimental methodology and obtained results</b>	<b>63</b>
7.1	GPSC performance with pure xenon filling . . . . .	63
7.2	Intrinsic energy resolution . . . . .	66
<b>8</b>	<b>Experimental results: Xe-He mixtures</b>	<b>71</b>
8.1	Electroluminescence yield . . . . .	71
8.2	Energy resolution . . . . .	74
8.2.1	Intrinsic energy resolution . . . . .	76
<b>9</b>	<b>Drift velocity and longitudinal diffusion</b>	<b>79</b>
9.1	Primary scintillation: x-rays . . . . .	80
9.2	Primary scintillation: alpha particles . . . . .	82
9.3	Electric field . . . . .	85
9.4	Electron transport theory . . . . .	86
9.5	Geometric efficiency . . . . .	87
9.6	Electronics and xenon scintillation . . . . .	87
9.7	Waveforms simulation . . . . .	88
9.8	Results: electron drift time . . . . .	89
9.9	Results: longitudinal electron cloud size . . . . .	91
<b>10</b>	<b>The relevance of helium contrasting with molecular mixtures</b>	<b>93</b>
<b>11</b>	<b>General conclusions</b>	<b>97</b>
11.1	Future work . . . . .	99
	<b>List of Figures</b>	<b>103</b>
	<b>Bibliography</b>	<b>107</b>

# Nomenclature

$\beta\beta 0\nu$	Neutrinoless double beta decay
$\beta\beta 2\nu$	Standard neutrino mode of double beta decay
APD	Avalanche Photodiode
CL	Confidence level
CUORE	Cryogenic Underground Observatory for Rare Events
DBD	Double Beta Decay
EL	Electroluminescence
ER	Energy Resolution
EXO	Enriched Xenon Observatory
F	Fano factor
FWHM	Full Width at Half Maximum
GPSC	Gas Proportional Scintillation Counter
HPXe	High Pressure Xenon
ITO	Indium Tin Oxide
LAAPD	Large Area Avalanche Photodiode
LN <sub>2</sub>	Liquid Nitrogen
LSC	Laboratorio Subterráneo de Canfranc
LXe	Liquid Xenon
MCA	Multi-Channel Analyser
MIP	Minimum Ionising Particle
NBrS	Neutral Bremsstrahlung
NEW	NEXT-White
NEXT	Neutrino Experiment with a Xenon-based TPC
NIR	Near Infra-red Region
PMT	Photomultiplier Tube

$Q_{\beta\beta}$  Energy released in the  $\beta\beta$  decay  
R-T Ramsauer–Townsend  
RAS Radon Abatement System  
ROI Region Of Interest  
S1 Primary scintillation signal  
S2 Secondary scintillation signal  
SiPM Silicon Photomultiplier  
SRIM Stopping and Range of Ions in Matter  
TPC Time Projection Chamber  
VUV Vacuum Ultra Violet

# Chapter 1

## Introduction

At present, whether we consider the Majorana or Dirac nature of Dark Matter and Neutrinos, they both hold a major importance for human knowledge. Neutrinos can have a Majorana-type mass and be its own antiparticle. If this statement is true, the neutrinoless double beta decay ( $\beta\beta 0\nu$ ) is allowed, since the two emitted anti-neutrinos can annihilate each other and only two electrons are emitted. While the two-neutrino mode of double beta decay ( $\beta\beta 2\nu$ ) has already been measured in several isotopes, the neutrinoless mode remains unobserved and holds important implications regarding the neutrinos nature. The unambiguous observation of this decay would demonstrate leptonic number violation and prove the Majorana nature of neutrino, presenting a breakthrough for new physics, beyond the Standard Model.

Since the  $\beta\beta 0\nu$  decay mode is very slow, when compared to other sources of background, as well as to the  $\beta\beta 2\nu$  decay mode, the experimental requirement for the energy resolution achieved in the Time Projection Chamber (TPC) is significantly stringent. Neutrinoless double beta decay events are detected by the sum of the kinetic energies released by the two electrons, which is always the same and equal to the mass difference between the original nucleus mass and the one created in the process ( $Q_{\beta\beta}$  - the energy released in  $\beta\beta$  decay). Due to the finite energy resolution of any detector,  $\beta\beta 0\nu$  events are reconstructed within an energy range centred at  $Q_{\beta\beta}$ , typically following a Gaussian distribution. However, there are other processes occurring inside the detector that may fall in that energy range, contributing to the background and compromising the experiment sensitivity. This drawback can only be suppressed by means of good energy resolution, and additional experimental signatures that allow the signal distinction against the background, mandatory for a good outcome.

In order to address these issues, xenon optical-TPCs based on the promotion of secondary scintillation and its readout as a mean for the amplification of the primary ionisation signal resulting from the radiation

interaction are being developed for rare event detection, such as directional dark matter [1–3] and double beta decay (DBD) detection [4, 5]. Many of these experiments involve operation in high pressure xenon (HPXe).

Xenon has no long-lived radioactive isotopes and is intrinsically radioactive clean. It has two natural occurring isotopes, namely:  $^{134}\text{Xe}$  and  $^{136}\text{Xe}$  which can decay by  $\beta\beta$  processes with  $Q_{\beta\beta}$  equal to 825 keV and 2458 keV, respectively [6]. A high Q-value is preferred, since the radioactive backgrounds are less abundant for higher energies. Therefore, the high Q-value of  $^{136}\text{Xe}$ , its relatively high natural abundance and the relatively inexpensive and simple enrichment process of this isotope [7], as well as the straightforward scalability offered by xenon as target and, simultaneously, detector medium, make the  $^{136}\text{Xe}$  isotope a very suitable choice for the  $\beta\beta 0\nu$  studies. The scalability of xenon is an advantage for covering the entire inverted hierarchy, which will require ton-scale xenon masses in order to reach a sensitivity of about 15 meV for the effective Majorana mass of the electron neutrino.

Taking into account that the energy resolution achieved in xenon is much better in the gas phase than in liquid, xenon is characterised by a small Fano factor (F - the ionisation fluctuations resulting from a given interaction event have a sub-Poissonian behaviour) [8], operation in HPXe is favoured relative to liquid xenon (LXe). In addition,  $\beta\beta 0\nu$  event detection in the gas phase allows for discrimination of the rare event through its topological signature, as demonstrated for double electron capture and double beta decay detection [9–13], which is much more effective when compared to LXe-based TPCs due to the reduced dimensions of the ionisation traces in LXe. A typical  $\beta\beta 0\nu$  event interaction results in a continuous trail of ionisations, produced by the two electrons emitted in opposite directions, with a Bragg peak appearing at both ends of the ionisation trail. The determination of two Bragg peaks at the end of a single continuous ionisation trail is an effective tool for  $\beta\beta 0\nu$  discrimination against gamma-ray interactions, which result in ionisation trails having only one Bragg peak at one of the ends, as a consequence of the photoelectron or Compton electron emission resulting from the gamma-ray interaction. Nevertheless, it is noted that the background due to  $\beta\beta 2\nu$  events cannot be discriminated by topology, being a low energy resolution the only mean for reducing the background of these events.

As a detection medium, xenon provides primary signals of both primary scintillation and ionisation [14], resulting from radiation interactions. In optical-TPCs the primary scintillation provides the  $t_0$  signal of the event, i.e. the start-of-event time-stamp, while the primary electrons produced along the trail of the ionising particles are drifted towards a scintillation region by a

weak electric field (of the order of few tens of V/cm/bar). In the scintillation region, the electrons are accelerated by a high electric field (of the order of few kV/cm/bar). Upon crossing this region, each electron attains, from the electric field, enough kinetic energy to excite but not ionise the gas atoms, by electron impact, leading to high scintillation-output (electroluminescence - EL) ensuing the gas deexcitation processes, without charge avalanche formation.

The amplification of ionisation electron signals through xenon electroluminescence allows the achievement of both higher detector signal-to-noise ratio [6, 7], due to the additional gain of the photosensor, and lower statistical fluctuations, when compared to charge avalanche multiplication [8]. At 10 bar, the best energy resolution achieved with a 1 kg scale prototype based on Micromegas was extrapolated to around 3%-Full width at half maximum (FWHM) at the xenon  $Q_{\beta\beta}$  [15], while a 1 kg- and a 10 kg-scale EL-based TPC achieved energy resolution values consistently below 1%-FWHM [16, 17]. In addition, the EL readout by means of photosensors electrically and mechanically decouples the amplification region from the readout, providing a system that is more immune to electronic noise, radiofrequency pickup and high voltage inconveniences.

The x- and y-positions of the primary electrons arriving at the EL region are determined by reading out the EL with a 2D-pixelated plane of photosensors while, from the difference in time between the primary scintillation and the EL pulses, the z-position at which the primary electrons have been produced can be determined.

EL yield values for xenon and argon have been measured for uniform electric fields [18–21], as well as for electron avalanches produced in modern micropatterned electron multipliers, e.g. GEM, THGEM, MHSP and Micromegas [15, 22, 23].

It is to be noted that the excellent energy resolution that can be obtained with the EL readout, e.g. needed for efficient background discrimination in  $\beta\beta0\nu$  detection, is only reached for the EL produced in electric fields of values that are below or near the onset of electron multiplication. The statistical fluctuations in the EL produced at electric field values below the onset of electron multiplication are negligible, when compared to those associated with the primary ionisation formation, while the statistical fluctuations of the EL produced in electron avalanches are dominated by the much larger variance of the total number of electrons produced in the avalanches [24, 25].

The topological signature in HPXe TPCs based on EL was already demonstrated [26–28], despite the large electron diffusion in pure xenon being an actual limitation, particularly for large drift distances. Diffusion

conceals the finer details of the ionisation trail, partially degrading the effectiveness of the discrimination based on the topological signature [29]. The pattern recognition of the primary ionisation trail for the 1 m drift scale becomes more difficult to achieve, since the electron transverse diffusion may be as high as  $10 \text{ mm}/\sqrt{m}$  for the low electric fields used in the TPC by Neutrino Experiment with a Xenon-based TPC (NEXT), i.e. a few tens of V/cm/bar [29].

Overall, the TPC spatial resolution depends both on the charge spreading through diffusion as electrons drift in the gas, as well as on the tracking plane granularity. Meaning that the longer the drift distances, the bigger the challenges of diffusion with the arriving charge distribution size rising as the square root of the drift distance, for any specific gas or admixture. Since detectors are becoming larger in size, the diffusion effects become a huge concern.

Recent studies have demonstrated that the addition to pure xenon of molecular gases, like  $\text{CO}_2$ ,  $\text{CH}_4$  and  $\text{CF}_4$ , in sub-percent concentration levels, reduces the electron diffusion down to  $\sim 2 \text{ mm}/\sqrt{m}$ , without jeopardising the TPC's performance in terms of EL yield and energy resolution, with  $\text{CH}_4$  found as the most suitable candidate [30–32].

On the other hand, it is necessary to take into account that standard xenon purification through hot getters may not be suitable for the chosen molecular additive, or else, the getters operating temperature may have to be lowered in order to prevent molecular absorption, which may affect the gas cleaning efficiency. In addition, the cryogenic separation of the molecular additive has to be made efficiently enough to prevent any loss of the expensive, enriched xenon. In addition,  $\text{CH}_4$  also presents some degree of excimer-quenching [31, 32], which could limit the primary scintillation yield and, therefore, the calibration for low energy events. While the aforementioned aspects are yet to be studied in higher detail in real-size detectors, and may be certainly overcome, the addition of a noble gas such as helium could offer an alternative solution, free from those limitations [33, 34].

Therefore, helium, as a noble gas, is being considered as a potential choice for additive and some studies on both electron drift parameters and EL yield of Xe-He mixtures have been carried out [34]. Helium atoms have a much lower mass, when compared to xenon atoms, which allows a more efficient cooling of electrons along the drift path. In addition, some advantages inherent to the use of helium as an additive are the use of exactly the same purification system as with pure xenon and it still brings the possibility to achieve a straightforward full xenon cryogenic recovery with liquid nitrogen ( $\text{LN}_2$ ). On the other hand, the use of such mixture will reduce the amount of

the source isotope in the detector because of the need for significantly higher helium concentrations. Thus, the chosen helium concentration must be a compromise between an improvement of the background rejection factor and a reduction of the active mass needed to maximise sensitivity [34].

Simulation studies of electron drift parameters, as well as primary and secondary scintillation yields of Xe-He mixtures have been carried out recently [34]. The simulation results show that a transverse diffusion of  $2.5 \text{ mm}/\sqrt{m}$  is achievable for a helium concentration of 15 %, without jeopardise the intrinsic energy resolution or the EL-yield.

Furthermore, experimental studies for the electron drift parameters in Xe-He mixtures were recently published by [35]. The impact of helium on the electron diffusion was not as substantial as anticipated, especially in the region corresponding to the Ramsauer minimum (around 10 V/cm/bar for pure xenon and 25 V/cm/bar for 15 % helium admixture) but remained in agreement with simulations outside that region. On the other hand, the impact of the helium additive on the xenon EL yield had yet to be determined experimentally in order to understand the scope of the use of these mixtures in EL-TPCs.

In this document we present experimental studies on EL yield of xenon and helium mixtures with helium concentrations from 0 to 30 %, as well as the impact of the helium addition on the TPC energy resolution and in the electron drift velocity. In addition, the impact on the reduction of the TPC sensitivity to  $\beta\beta 0\nu$  detection due to the reduction on the overall  $^{136}\text{Xe}$  mass and a comparison with the necessary improvement achievable through the enhancement of the topological discrimination is discussed.

This R&D was the main goal of this PhD program.

The layout of this document is as follows.

In chapter 2, a brief introduction to neutrinoless double beta decay is given, as well as some current experiments upon the double beta decay.

In chapter 3, the concept and objectives of the NEXT experiment are described, together with the constraints and strengths of the technology for the search of neutrinoless double beta decay. The results obtained with several prototypes already investigated are reported as well as the NEXT-100 detector prospects. The main limitation on NEXT experiment, relative to signal topology determination, is explained in detail. The results achieved with the addition of molecular species to pure xenon are presented in the end of this chapter.

In chapter 4, the theory behind the electroluminescence is also explained.

In chapter 5, the helium role as an additive in the improvement of gaseous mixtures in a TPC is presented. The results on several parameters achieved on

previous studies on xenon-helium mixtures are described in this chapter.

Chapter 6 presents the experimental setup and discusses the methodology followed for the xenon-helium gas mixing, the data acquisition and the waveform analysis as well.

In chapter 7 the results achieved for energy resolution and electroluminescence yield with pure xenon are presented, as well as the validation for the whole methodology of data taking and associated analysis.

In chapter 8 the results for the energy resolution and the electroluminescence yield are presented for the studied mixtures of helium addition to xenon.

Chapter 9 presents the constraints on the primary scintillation studies, either with x-rays or with alpha particles. The longitudinal diffusion and the drift velocity studies are described and the obtained results are presented.

The chapter 10 is dedicated to the discussion of the relevance of xenon-helium mixtures, comparing the obtained results with those obtained for other xenon mixtures with molecular species.

Finally, the chapter 11 is dedicated to the conclusions of these studies and the prospects of future work.

My main contributions to the work presented in this thesis was as follows:

The system assembly for the helium mixtures, including the real-time monitoring possibility of the detector operation characteristics, e.g. pulse amplitude and energy resolution, starting with the pure xenon filling and its respective studies, then performing the helium addition for a specific concentration and its respective studies, followed by a second mixture with another helium concentration. This system allows the possibility of ensuring the same operation conditions without the need for interruption on the voltages applied to the detector electrodes, while keeping the total pressure without significant pressures changes in the detector. The assembly allows the xenon recovery and respective purification as well.

The whole experimental execution, data acquisition and respective analysis, as well as the presentation and discussion of the results obtained to the NEXT collaboration.

I still had the opportunity to take part on the experimental campaign in operation and data acquisition, as well as in problem solving related with the NEXT-NEW TPC and its ancillary systems maintenance, at the Laboratorio Subterráneo de Canfranc (LSC), Huesca, Spain.

A first huge and crucial challenge that was needed to overcome in this work was the ability to demonstrate that the experimental system we have in GIAN provides reliable and repeatable results, since from the beginning our results did not reproduce exactly what simulations had foreseen.

Another challenge was the measurement, in our setup, of other parameters, such as the electron drift velocity in pure xenon and in the xenon-helium mixtures as well, in order to validate the performed analysis, so it could give some robustness and credibility to this work as well as to the followed methodology.

Another concern was the estimation of the experimental uncertainties associated with the achieved results for both the electroluminescence yield and energy resolution of the detector.

The core of this thesis resulted in one publication in a major journal of the first quartile:

Low-diffusion Xe-He gas mixtures for rare-event detection: Electroluminescence Yield, A. F. M. Fernandes, C. A. O. Henriques, R. D. P. Mano et al. (NEXT Collaboration), *Journal of High Energy Physics* 4(2020)034



# Chapter 2

## Neutrinoless double beta decay

### 2.1 Majorana neutrinos

Unlike other known fermions, neutrinos can actually be truly neutral particles, meaning they are indistinguishable from their antiparticles. Therefore, the proof of Majorana-type mass neutrinos would imply that a new energy scale of physics characterises new dynamics behind the Standard Model and explains why neutrino masses are so much lighter than the charged fermions [36, 37]. This could be a contribution to understand leptogenesis - the symmetry breaking mechanism, and the origin of mass as it could be the origin of the matter-antimatter asymmetry observed in the Universe. The existence of Majorana neutrinos would also imply that the quantum lepton number is not conserved [38–40].

In order to accomplish this major objective, there are two conditions needed to be proven experimentally: the violation of the lepton number and the charge-parity violation in the lepton sector.

### 2.2 Neutrinoless double beta decay

One way to experimentally verify that neutrinos are their own antiparticle is the detection of neutrinoless double beta decay. This is a very slow process where a nucleus with  $Z$  protons decays into a nucleus with the same mass number and  $Z + 2$  protons, emitting two electrons which carry the total energy released in the process ( $Q_{\beta\beta}$ ). This process can only occur if the neutrinos are really massive Majorana particles.

The standard two-neutrino mode consists in two simultaneous beta decays,  ${}^A_Z X \rightarrow {}^A_{Z+2} X + 2 e^- + 2 \bar{\nu}$ , which has been observed in several isotopes with typical half-lives in the range of  $10^{18} - 10^{21}$  years [41], where two neutrons transform into two protons plus two electrons and two antineutrinos. Lepton number is therefore conserved because the electrons

and antineutrinos have opposite lepton number. However, if neutrinos were Majorana particles, double-beta decay could occur without the emission of antineutrinos, meaning the lepton number would change. In addition to other features, the measurement of the decay rate of  $\beta\beta 0\nu$  would provide direct information on the mass of neutrinos.

The detectors used to search for this decay are thought and designed in order to measure the emitted radiation energy of a  $\beta\beta 0\nu$  source. In a real detector the  $\beta\beta 0\nu$  events are reconstructed within an energy range centred at  $Q_{\beta\beta}$ , due its finite energy resolution, following a Gaussian distribution. There are other processes which are part of the intrinsic background occurring in the detector that fall in the same energies region compromising the experiment sensitivity and can only be suppressed by a good energy resolution [42].

The underground operation of these detectors solves the problem of cosmogenic origin backgrounds, however, the signal peak can easily be overwhelmed by natural radioactivity emanating from the detector's materials and surroundings, which makes it essential that the chosen materials are radiopure [8].

The most important characteristics of an experiment like this one are optimal energy resolution, in order to constrain the region of interest as much as possible, and a good detector shielding as well, in order to get rid of the spurious events with almost the same energy as the  $Q_{\beta\beta}$ . The topological information as experimental signature is a bonus to further provide improved results [43], by background rejection.

The addition of molecular gases to pure xenon is a solution to improve the spatial resolution, since it reduces the electron diffusion. Nonetheless, this will imply degradation of the scintillation parameters on the HPXe TPC projected by the NEXT collaboration.

In addition to the energy resolution and background control, there are other factors that must be taken into consideration in a project like this, as the detection efficiency and scalability to larger masses. The optimisation of these parameters is most of the time conflicting, the reason why so many different experimental techniques have been proposed so far.

## 2.3 Current experiments on double beta decay studies

Most of the experimental searches for  $\beta\beta 0\nu$  have been dominated by germanium calorimeters, mainly due its excellent energy resolution. In particular, for about a decade the best limit to the half-life of  $\beta\beta 0\nu$  was the one set by the Heidelberg-Moscow (HM) experiment:  $T_{\frac{1}{2}}^{0\nu}({}^{76}\text{Ge}) \geq 1.9 \times 10^{25}$  years

at 90 % confidence level (CL) [44].

Some experiments have demonstrated new sensitivity levels to the neutrinoless double-beta decay, reporting new lower limits on the decay's half-life, all of which exceed years. Those experiments determine the decay half life by monitoring a large number of atoms for a given double-beta decay isotope and looking for a peak in the two-electron energy.

One of the most important features in sensitivity is exposure, the product of the active isotope amount and the measurement time. The ability to recognise the electron peak inside the background is a major element in this search. To overcome this obstacle, the experiments typically narrow the search to energies in a small region of interest around the decay energy. Thus, the better the energy resolution of a detector, the more false counts can be excluded [45].

Additional efforts are ongoing with different isotopes that use thin foils in a gaseous tracking detector (NEMO-3 [46] and SuperNEMO [47]), scintillating bolometers (CUPID [48], LUCIFER [49], AMoRE [50]) and solid TPCs (COBRA) [51, 52], among others.

## **CUORE**

The Cryogenic Underground Observatory for Rare Events (CUORE) [53, 54] is a ton-scale cryogenic detector located at Laboratori Nazionali del Gran Sasso (LNGS) in Italy and uses cooled TeO<sub>2</sub> crystals made of natural tellurium, 34 % of which is the double-beta decay isotope <sup>130</sup>Te. The experiment consists of an array of 988 TeO<sub>2</sub> crystals operating as cryogenic calorimeters [55–57] (also called bolometers) at  $\sim 10$  mK temperature.

This experiment observed a background of  $(1.38 \pm 0.07) \times 10^{-2}$  counts/(keV kg yr) in the region of interest for the neutrinoless double beta decay [58]. With a total exposure of 372.5 kg yr a median exclusion sensitivity of  $1.7 \times 10^{25}$  was achieved. For a 90 % CL, a lower limit of  $3.2 \times 10^{25}$  yr on the <sup>130</sup>Te half-life was set. Assuming the Majorana neutrinos as the mediators in the neutrinoless double beta decay, the effective Majorana mass will result on an upper limit of 75-350 meV [58].

The CUORE experiment has a very good energy resolution and scalability as well. Its complicated cryogenics, the background contamination, mainly near the crystal surfaces, and signal readout are their main drawback.

## **SNO+**

The SNO+ is a large multipurpose detector upgraded from the previous Sudbury Neutrino Observatory (SNO), placed 2 km underground at SNOLAB in Sudbury, Canada [59]. It now performs an ultra-pure liquid

scintillator, using  $^{130}\text{Te}$  as detection medium with a high natural abundance of  $\beta\beta$  source, with the great advantage to scale up to larger masses.

As a pure water Cherenkov detector, SNO+ has been taking data for more than one year, while preparing for filling with scintillator. Then, the strategy is to load 3900 kg of tellurium in the detector volume, with a low background level surrounded by a high optical coverage, to search for the neutrinoless double beta decay. All this commissioning is planned into three experimental phases [60].

The SNO+ water phase was successfully completed. The next step will be the pure scintillator phase, when the required achievement of high purities will be checked, and after that the tellurium loading will be performed [60]. Therefore, in phase I, SNO+ has projected a sensitivity of  $T_{\frac{1}{2}}^{0\nu} > 1.9 \times 10^{26}$  for 90 % CL, after 5 years of data taking [61], which corresponds to a limit of  $m_{\beta\beta} < 41\text{-}99$  meV [61]. In a second phase is expected at least a  $T_{\frac{1}{2}}^{0\nu}$  limit of  $10^{27}$  years. This could be achieved with increased  $^{130}\text{Te}$  loading [62]. Furthermore, in the absence of signal, the expected limit is  $T_{\frac{1}{2}} > 1.9 \times 10^{28}$  years at 90 % confidence level, for neutrinoless double beta decays [60].

### **KamLAND-Zen**

The KamLAND-Zen experiment is a modification of KamLAND neutrino detector (Kamioka Liquid Scintillator Anti-neutrino Detector) using its ultra-low background environment with xenon (enriched to 91 % in  $^{136}\text{Xe}$ ) [63]. The KamLAND-Zen 800 project was prepared with a cleaner container for xenon loaded liquid scintillator, with  $\sim 750$  kg of xenon. This container production begun in 2017 and its data acquisition was started in early 2019 [64]. The data analysis relative to 132.7 days brings a lower half-life limit of  $4 \times 10^{25}$  years with 90 % CL for the  $0\nu\beta\beta$ , with a sensitivity of  $8 \times 10^{25}$  years [64].

In the future, the collaboration proposes a major detector upgrade, using 1 ton of enriched xenon, aiming to improve its energy resolution, using high quantum efficiency PMTs. They predict it will improve the energy resolution down to  $< 2.5$  % at the Q-value of the  $^{136}\text{Xe}$  decay. With these improvements, they hope to cover the inverted neutrino mass hierarchy down to 20 meV [65, 66].

### **EXO-200**

The EXO-200 (Enriched Xenon Observatory) is an upgraded detector using a symmetric liquid xenon TPC with 150 kg of xenon enriched to 80.6 % in  $^{136}\text{Xe}$  as both source and detection medium.

From the full data set acquired before the upgrades, by applying it some

analysis improvements, the  $0\nu\beta\beta$  half-life sensitivity achieved was to  $1.8 \times 10^{25}$  yr with 90 % confidence level, with no observed statistically significant evidence for  $0\nu\beta\beta$  [67]. The data from individual phases I and II set lower limits of  $1.0 \times 10^{25}$  and  $4.4 \times 10^{25}$  yr at the 90 % CL, respectively, with a median sensitivity of  $2.9 \times 10^{25}$  yr and  $1.7 \times 10^{25}$  yr, respectively [67].

Further operation of the upgraded detector is expected to improve the  $0\nu\beta\beta$  sensitivity, holding promise for the called nEXO (next EXO) [68], a ton-scale TPC that will use enriched xenon in liquid state, designed to reach a half-life sensitivity in the order of  $\sim 10^{28}$  years, with a Majorana neutrino mass sensitivity of 7 - 18 meV [67].

## GERDA

The GERmanium Detector Array (GERDA) experiment uses germanium diodes enriched in  $^{76}\text{Ge}$ , in an active liquid argon shield. So far, a low background index of  $5.2 \times 10^{-4}$  counts/(keV kg yr) was achieved in the signal region, thus meeting the design goal to collect an exposure of 100 kg yr in a background-free regime [69]. However, the enrichment process of germanium is hard, since it is solid at room temperature, compromising the experiment scalability to larger masses.

Joining the data from phases I and II, the limit on the half-life of  $\beta\beta 0\nu$  decay in  $^{76}\text{Ge}$  is  $T_{1/2} > 1.4 \times 10^{26}$  yr at 90 % CL, having obtained a  $m_{\beta\beta}$  limit  $< 79 - 180$  meV [69].

According to [70], in the second phase 20 kg were added, hoping to increase the half-life sensitivity beyond  $10^{26}$  years.

GERDA improved the sensitivity by one order of magnitude with respect to previous  $^{76}\text{Ge}$  experiments [44], having relied on digital pulse-shape analysis for the signals from HPGe, like Compton scatters, and single-site events that might be an indication for the neutrinoless double beta decay. Thus, it was proved the feasibility of a background-free experiment based on  $^{76}\text{Ge}$  [69].

## Majorana Demonstrator

The Majorana Demonstrator experiment consists on a low-background modular array of high-purity germanium detectors to search for neutrinoless double-beta decay of  $^{76}\text{Ge}$  to excited states in  $^{76}\text{Se}$ . This experiment is based in germanium at ton-scale, complementing GERDA [71], being located at the Sanford Underground Research Facility in Lead, South Dakota [72].

The experiment is now using 41.9 kg yr of isotopic exposure, having reached half-life limits in the range of  $(0.75 - 4.0) \times 10^{25}$  yr for each excited state decay of  $^{76}\text{Ge}$ , with 90 % CL [73].

Under the assumption of light neutrino exchange, upper limits on  $|m_{\beta\beta}|$  of 3.2 - 7.7 eV were calculated [74, 75], applying nuclear matrix elements calculated for  $\beta\beta 0\nu$  to the  $0_1^+$  excited state.

# Chapter 3

## The NEXT Experiment

### 3.1 The NEXT experiment roadmap

The NEXT collaboration aims at the detection of neutrinoless double beta decay in xenon enriched with the isotope  $^{136}\text{Xe}$  [4] and, currently, operates the largest HPXe optical-TPC at (10-15 bar), based on EL for ionisation signal amplification [76]. Its concept combines a very good energy resolution with a topological signature discrimination capability and a radioactive clean detector.

The NEXT collaboration has already developed a R&D program with the specific goal of proving the performance of its technology. This program resulted in the assembly and operation of three prototypes: NEXT-DBDM, NEXT-DEMO and NEXT-NEW. NEXT-DEMO was designed as a proof of concept and test-bed for the technology of the NEXT-100 detector.

The NEXT roadmap was designed in four stages:

i) Construction, commissioning and operation of NEXT-DEMO and NEXT-DBDM prototypes; demonstration of the HPXe technology deploying a mass of natural xenon in the range of 1 kg. Both prototypes have demonstrated the robustness of the technology of high pressure xenon gas time projection chambers with electroluminescent amplification (HPXe-EL) for neutrinoless double beta decay searches with an excellent energy resolution.

ii) Background characterisation and measurement of the signal with the NEXT-White detector, deploying 10 kg of enriched xenon and operating at the *Laboratorio Subterráneo de Canfranc* (LSC); demonstration that energy resolutions below 1 % can be reached in large HPXe TPCs, as well as demonstration of the topology discrimination efficiency and measurement of the  $\beta\beta_{2\nu}$  decay half-life [28];

iii) Search for  $\beta\beta_{0\nu}$  decays with the NEXT-100 detector, which deploys 100 kg of enriched xenon;

iv) Search for decays with the NEXT detector, which will deploy masses

in the range of the ton scale and will introduce two additional handles: a) A magnetic field, capable of further enhancing the topological signal of NEXT; and b) barium-tagging (a technique pioneered by the EXO experiment which is also accessible to NEXT).

NEXT-White (NEW) allowed the validation of the background model with actual data, as well as a study of the evolution of the energy resolution with the event's energy. The resolution near  $Q_{\beta\beta}$  was measured using a thorium source, which provides 2.6 MeV gammas. It is also intended to reconstruct the spectrum of  $\beta\beta 2\nu$ , whose events are topologically identical to signal events  $\beta\beta 0\nu$  and can be also used in order to demonstrate with the recorded data and respective results the real power of the topological signature [77].

The NEXT-100 detector will have a readout system for calorimetry and tracking different from the ones used in the prototypes and in order to distinguish signal from background, it will use energy resolution and event topology.

Given the imposed conditions of energy resolution and high background rejection power for the observations of the two electrons, the technology behind a HPXe TPC, to be used in NEXT-100, is exceptional and will be a starting point for the next generation of ton scale HPXe experiments [8].

### 3.1.1 The NEXT detector

The NEXT collaboration aims the construction and operation of the NEXT-100 detector at high pressure with gaseous xenon with a Time Projection Chamber. This detector will be used to search for neutrinoless double beta decay events, using 100 kg of enriched xenon at 90 % in its  $^{136}\text{Xe}$  isotope. This experiment will be performed at the LSC [8].

NEXT-100 offers major advantages on the search of neutrinoless double beta decay, such as:

- Energy resolution with an intrinsic limit of  $\sim 0.3$  % FWHM at  $Q_{\beta\beta}$  and  $< 1$  % already demonstrated in NEXT-White;
- Tracking capabilities with the power to discriminate the topological signature between the signal (two electrons) and background (single electrons);
- Homogeneous and fully active detector with the ability to make 3-dimensional reconstructions, making possible to locate the events in a fiducial region away from surfaces, where the background is higher;
- Scalability to larger masses, with the use of a noble gas suitable for detection and with no intrinsic radioactivity (xenon).

In order to cover the inverse neutrino mass hierarchy, are required sensitivities to effective neutrino masses in the range of 20 meV, which weren't achieved yet for the  $\beta\beta 0\nu$  experiments in operation. This sensitivity must be improved by one order of magnitude in the effective neutrino mass, or two magnitude orders in the  $\beta\beta 0\nu$  decay period. This requires the increase of the one hundred factor of the exposure from the typical current generation values of experiments, which means to go from  $\sim 100$  kg yr to  $\sim 1$  ton per ten years and decrease the residual backgrounds by a 100 factor ( $\sim 0.1$  events per ton) [8].

Thus, a detector able to implement a large source mass of pure isotope at a reasonable cost is needed. Until now, only xenon has demonstrated this capability [8]. Unlike almost any other  $\beta\beta$  source, one ton of xenon can be acquired at a reasonable cost. In fact, one ton of enriched  $^{136}\text{Xe}$  already exists, combining the KamLAND-Zen, EXO and NEXT experiments. The HPXe technology has the potential to provide the most sensitive detector at this scale, by scaling the detector to a mass in the range of one ton and joining additional handles to further suppress the background [77, 78].

### **NEXT-100 concept**

NEXT-100 is a high-pressure xenon electroluminescent Time Projection Chamber with separated planes for energy measurement, with photomultiplier tubes (PMTs) and for tracking, with silicon photomultipliers (SiPMs). It will operate in the Canfranc Underground Laboratory facilities, in the Spanish Pyrenees.

On the side of the energy resolution, the Fano factor of gaseous xenon is much lower than the one of liquid xenon. Moreover, the electroluminescence used to attain signal amplification, has very low fluctuations in gain.

The use of xenon at 10 bar brings the possibility to take advantage of the event topological signature: a track of about 15 cm is left by two electrons released in the neutrinoless double beta decay, with almost constant energy deposition and two blobs of energy at the end of its tracks, caused by the stopping electron's Bragg-peaks. This signature is a major advantage which allows the background rejection [43].

A Scalable Readout System (SRS) is the modular architecture of the NEXT-100 data acquisition system (DAQ) used [79]. As shielding, a lead castle made in two moving halves protects the detector from external flux of high energy gamma rays. It has an open and closed position, (see fig. 3.1) being the latter used in usual operation [8].

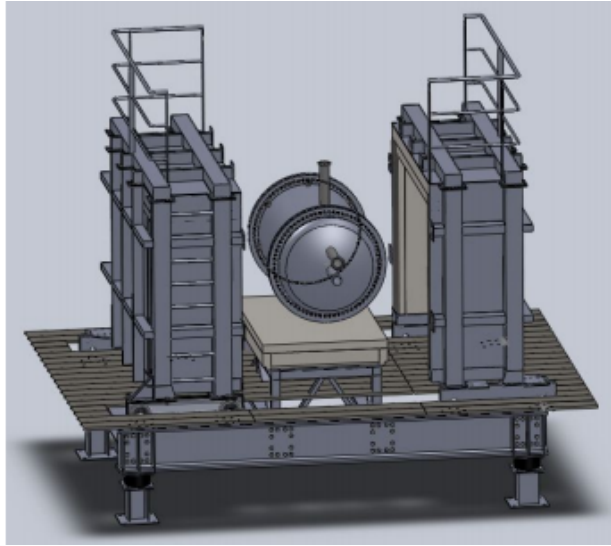


Figure 3.1: Drawing of the NEXT-100 lead castle shield in its open configuration [8].

For NEXT-100, the target electron life-time is  $\sim 5$  ms, with a drift length of 1 ms. This requires the control of impurities, particularly oxygen, at the level of 1 ppb [80, 81], only achievable with careful selection of TPC materials that contact with the gas, as well as a continuous circulation and purification of the gas [28, 82].

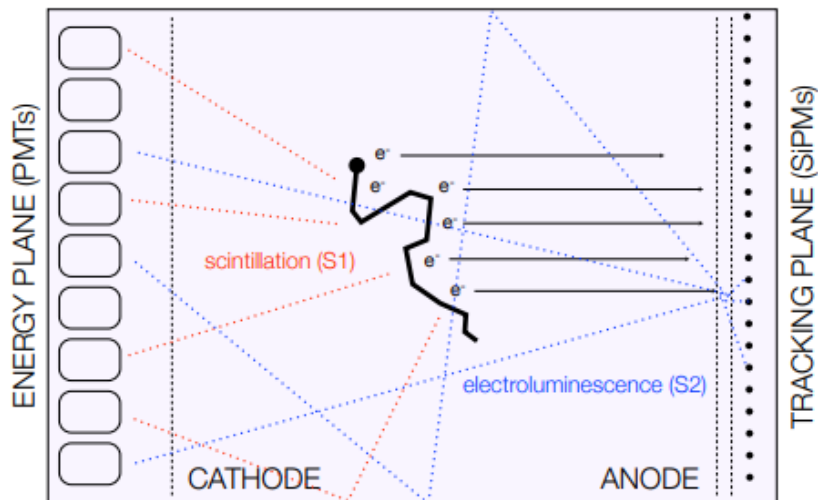


Figure 3.2: The concept in NEXT experiment [8].

The ionisation signal is amplified in NEXT by electroluminescence in order to achieve the best energy resolution possible. The EL signal provides both tracking and energy measurement.

The chamber will have separated detection systems for tracking and calorimetry, illustrated in figures 3.2 and 3.3 following the ideas introduced in the studies from [79, 83].

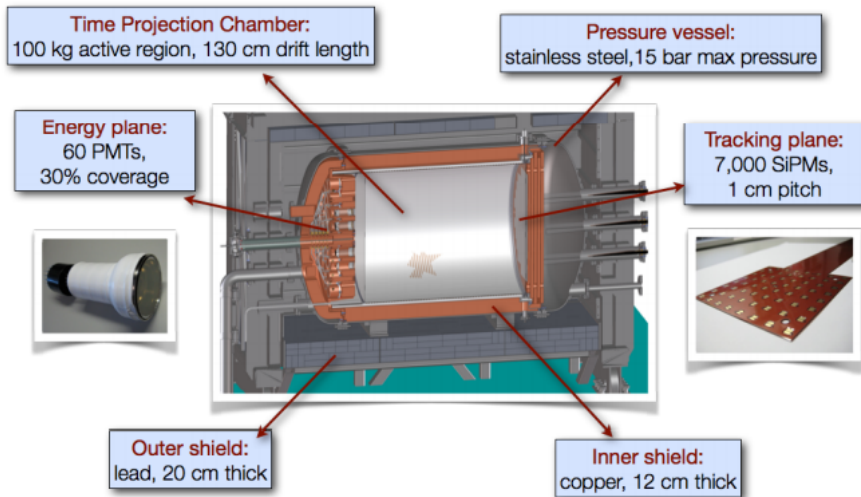


Figure 3.3: The NEXT-100 apparatus from [77].

The particles interacting with the HPXe will transfer their energy by ionisation and excitation processes. The excitation energy manifests by vacuum ultra violet (VUV) scintillation light ( $\sim 178$  nm) from excimers, created in a three-body collision of two neutral atoms and one excited atom produced by electron impact.

Therefore, the products of ionisation left by the particle, positive ions and electrons, are prevented from recombination with an applied electric field in the range of 0.03-0.05 kV/cm/bar. Then, the electrons released by ionisation will drift toward the TPC anode, going into another region with an electric field much higher (3 kV/cm/bar), defined by a stainless steel mesh and a grounded quartz plate coated with indium tin oxide (ITO) and thin films of tetraphenyl butadiene (TBT). VUV photons are generated isotropically at this region by electroluminescence. Thus, an optical signal is produced by both scintillation and ionisation which is detected at the PMT's plane located right behind the cathode. The starting event is registered with the primary scintillation detection and the energy measurement is provided by EL light detection. This latter also allows the tracking reconstruction, since the EL signal is also detected at the anode plane [8].

Recent studies in xenon TPCs revealed the presence of a new photon emission mechanism, in addition to VUV scintillation light from excimers, presenting arguments in favour of neutral bremsstrahlung (NBrS), as the responsible for that emission [84]. This mechanism is produced by ionisation electrons when they are scattered on neutral atoms, even if they haven't sufficient energy in order to induce excitation. NBrS ranges from the UV to the near infra-red region (NIR), depending on the electron energy and on the reduced electric field, hence competing with electroluminescence when electrons have energies around and above the xenon excitation threshold. For

low electron energies, the NBrS intensity can be shown to be proportional to the elastic electron-atom cross section [85], a universal interaction mechanism during electron drift in gases.

In [84] is presented the first NBrS luminescence unambiguous identification in xenon, supported by a predictive theoretical model of this light-emission process. NBrS emission is intrinsically broadband and immune to quenching mechanisms, unlike conventional excimer-based EL emission. Since it does not create additional electrons nor ions, NBrS is expected to be free from ion feedback or ageing issues. Hence, it is seemingly of relevance in a range of reduced electric field values employed for secondary scintillation, extending from 1 kV/cm/bar to typical drift fields of 100 V/cm/bar, arguably down to the thermal limit (around  $E/p = 10$  V/cm/bar in pure xenon, at room temperature). Nevertheless, the NBrS contribution to the EL scintillation is less than 1 %, for nominal EL-field values above 1 kV/cm/bar, i.e., it is insufficient to modify the calorimetric response of xenon TPCs. Similarly, for typical drift fields below 50 V/cm/bar, the NBrS emission falls below the sensitivity range of conventional photomultipliers (PMTs) [84].

### 3.1.2 Background

In order to predict the background events that may be misidentified as signal, a background model was created, where both the possible sources of radioactive contaminants and their activity in the detector materials have been described by simulation [8].

Thus, the detector radio-purity evaluation and the detector simulation make the base of this background model.

With this model is possible to determine the sensitivity to do measurements of the  $\beta\beta 2\nu$  mode in NEW, as well as the search of  $\beta\beta 0\nu$  in NEXT-100. Backgrounds from material's natural radioactivity and with cosmogenic origin justify the reason why the choice of radiopure materials and the underground operation are a must. Therefore, an extra background (B) rejection, better detector efficiency ( $\epsilon$ ) and larger exposure ( $M.t$ ) are additional experimental features in order to improve the detector sensitivity [41]. This relation is summarised as:

$$T_{\frac{1}{2}} \propto a.\epsilon\sqrt{\frac{M.t}{\Delta E.B}} \quad (3.1)$$

In order to evaluate all the main backgrounds that can mask the  $\beta\beta 0\nu$  signal, coming from the materials to be used in NEXT-100 construction, a detailed simulation of the detector performance has been implemented in NEXUS, the Geant4-based simulation program used in NEXT experiment. The accuracy of

this model will be validated and improved by NEW operation and its results [78].

Backgrounds from ambient sources can be further reduced through combination of particle identification and fiducial cuts [26].

The expected background rate is at most  $4 \times 10^{-4}$  counts/keV/kg/yr, meaning 1 event per year for 100 kg of xenon. The expected sensitivity is  $6 \times 10^{25}$  years to the  $\beta\beta 0\nu$  decay process within 5 years running [86].

## Radioactive contaminants

The decay of  $^{214}\text{Bi}$  into  $^{214}\text{Po}$  emits de-excitation gammas with energies beyond 2.3 MeV, and the gamma line at 2447 keV, with 1.57 % intensity is too close to the Q-factor of  $^{136}\text{Xe}$ .

There is also the decay of  $^{208}\text{Tl}$  into  $^{208}\text{Pb}$  where de-excitation photons of 2614 keV and 100 % intensity are emitted. The Compton edge of this gamma is under the  $Q_{\beta\beta}$ , at 2382 keV, but the scattered gamma can still interact and produce another electron tracks close enough to the initial Compton electron, being reconstructed as single objects in the energy region of interest (ROI).

The photoelectric electrons are produced upward the ROI, but they can lose its energy by bremsstrahlung effects and populate the window (in case of emitted photons escape out from the detector). In this situation single-track events cannot be produced by pair-creation events.

## Radon

The radioactive isotopes  $^{222}\text{Rn}$  and  $^{220}\text{Rn}$ , from the  $^{238}\text{U}$  and  $^{232}\text{Th}$  chains, may decay into  $^{214}\text{Bi}$  and  $^{208}\text{Tl}$ , respectively. The Radon suffers an alpha decay into polonium and produces positive ions which are drifted to the cathode by the TPC electric field. In this way, there will be contamination of  $^{214}\text{Bi}$  and  $^{208}\text{Tl}$  deposited in the cathode surface.

Radon is a potential background for double beta decay experiments, so, the full control of radon is the key for low background [17]. An inner lead castle was installed in 2018 in order to provide further shielding against external backgrounds. Furthermore, a radon abatement system (RAS) by ATEKO A.S. has been flushing radon-free air into the air volume enclosed by the lead castle [87]. From recent analysis, it was verified that the  $^{222}\text{Rn}$  content in the flushed air is 4-5 orders of magnitude lower, when compared to the air environment in NEXT-NEW [88]. Such a reduction allows the detector operation in a virtually airborne-Rn-free environment [87].

## Cosmic rays and rock backgrounds

The main reason why double beta decay experiments are performed underground is the production of high energy photons produced by cosmic particles, which also may activate materials. The detector is placed at a depth for which the only surviving cosmic ray particles are muons, although, their interactions with the rock produces neutrons and electromagnetic showers. The rock itself also acts as an intense source of neutrons and  $^{208}\text{Tl}$  and  $^{214}\text{Bi}$  backgrounds [8].

The shielding reduces considerably the mentioned backgrounds as well as the residual muon and neutron background are not significant for the experiment, having into account the topological capabilities of NEXT [8].

### 3.2 Topological signature

Electrons moving through gaseous xenon at a pressure of 10 bar (the pressure used in the studies related in the present work) lose their energy at an approximately fixed rate, during the travelled path length. At the end of the trajectory the rise in  $1/v^2$ , with  $v$  the speed of the particle, caused by the loss of energy, which leads to a significant energy deposition in a compact region (where multiple scattering occurs in a short distance), usually referred as 'blob'. More than 20 % of the event energy is splitted between both blobs due to the Bragg-like peaks in the  $dE/dx$  of the stopping electrons [26, 77].

The neutrinoless double beta decay signal involves two electrons whose energy sum to  $Q_{\beta\beta} \sim 2.45$  MeV. Although the good energy resolution is enough to discriminate such events from the more abundant  $\beta\beta 2\nu$ , there still are backgrounds originated by high energy gammas which convert in the gas through Compton, photoelectric and pair production processes, emitted from the decay of  $^{208}\text{Tl}$  and  $^{214}\text{Bi}$  whose signals are single electrons with energy similar to  $Q_{\beta\beta}$ , whose tracks have just one blob of energy at one extreme [26, 89].

Thus, a topology with two electrons with a common vertex and a single continuous trajectory with a blob at each end is the searched signal event (depicted in figure 3.4 left) which is discriminated from the backgrounds described before, whose signal has a single electron track with only one blob (depicted in figure 3.4 right).

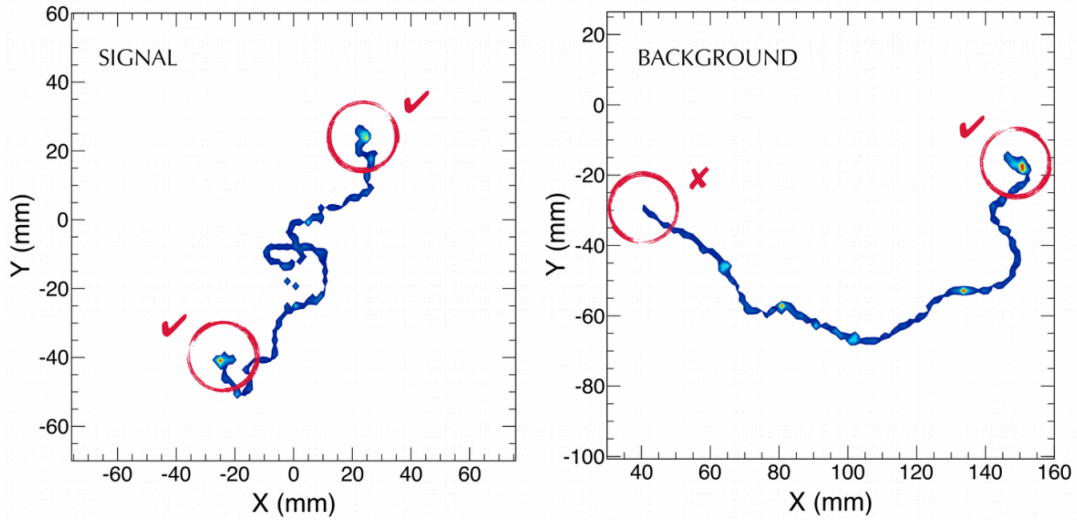


Figure 3.4: A  $\beta\beta 0\nu$  event (at left) and a single electron background event (at right). Both events were simulated in Monte Carlo at 15 bar gas pressure [26].

In order to accomplish the design of the tracking plane, there are several effects inherent to electron's interaction in the gas, causing energy fluctuations of the electron track. Those effects are resultant from the readout signal that must be taken into account, namely: the bremsstrahlung photons or delta rays emitted by electrons and the electron cloud diffusion during drift. Therefore, the reconstruction topology of two electrons with a common vertex will bring the power requirement so the clear description of the end-point blob energy deposit and minimum ionising particle (MIP) regions might be possible, so a clear distinction can be made relatively to a single electron track [89].

For the purpose described, it is then required a good position resolution in order to separate the blob and the MIP track regions and also because the electrons path length regions with high energies cannot be added together, misidentifying the deposit of a false blob. Thus, a fine grained tracking would be useful if the blurring of the track due to delta electron and photon emission, and also the following electron cloud drift, could remove any useful information at this level [89].

As aforementioned, the topology signal is limited by the effect of electron diffusion during drift, whose improvement was already proved with molecular additives. This is explained in more detail further in this document.

Caltech-Neuchâtel-PSI Collaboration was the pioneer using this topological signature aiming to eliminate the background in  $\beta\beta 0\nu$  experiments [90].

### 3.2.1 Limitations in the tracking plane

There are physical and instrumental limitations which could limit the spatial resolution of a gaseous detector. With regard to instrumental constraints, the pitch of SiPMs sensors used in NEXT as tracking plane limits the transverse resolution. This problem could be solved by adding more SiPMs to the tracking plane, decreasing the sensor's pitch. In NEXT detector, having 1 mm<sup>2</sup> SiPM with 1 cm pitch, the spatial resolution is 3.5 mm and can still be reduced with the use of reconstruction algorithms [29].

Furthermore, the longitudinal resolution is dependent on the timing between the initial event provided by the primary scintillation signal (S1) and the arrival time of the primary electrons to the electroluminescence region provided by the secondary scintillation signal (S2).

When electrons get into the EL region, each one will produce light during a time given by the ratio between the EL region gap size and the drift velocity. In NEXT-100 this time is 3  $\mu$ s for a reduced electric field of 3.5 kV/cm/bar at the EL region, leading to a longitudinal resolution of 1-1.5 mm [29]. These results can still be improved by reducing the EL region gap, but for the dimensions of the NEXT-100 detector this would not be easy to accomplish.

## 3.3 Topology reconstruction

The reconstructed electron tracks show a random walk through the gas and a clear end-point with higher energy deposition. Thus, the possibility to reconstruct the event topology is a major advantage of the NEXT design.

The readout plane must be a few millimetres away from EL production region, for which blurring would be in the order of 1 cm, considering the expected transverse diffusion of 10 mm/ $\sqrt{m}$ . Furthermore, a pitch of 1 cm was described at [79] as the best compromise in order to prove a good discrimination between the two blobs with a reasonable number of channels at 10-15 bar pressure of pure xenon. These results justified the pitch used at NEXT-DEMO and NEXT-NEW tracking planes [89].

In previous publications, the event topology reconstruction was performed by dividing the z-dimension in time slices and for each slice was reconstructed a single xy point. A width slice of 4  $\mu$ s was used, as it is the time needed so an electron cross the EL gap and gives enough information in order to achieve a reliable xy reconstruction. The xy position of a slice was reconstructed by means of the medium position with higher scintillation signal recorded by SiPMs weighted with their collected integrated charge. For the same time interval, the energy associated with this position is then recorded [8].

The drift velocity of electrons and the time relative position of S1 and S2 signals were used to unambiguously define the  $z$  position. In order to reconstruct the  $xy$  position of a charge deposit was used the barycentre method, indicated as optimal by Monte Carlo studies, since it uses the signals from  $\sim 20$  SiPMs with greatest charge.

Reconstruction of tracks in an electroluminescent TPC is complicated not only due the diffusion of the charge cloud during drift, but also by the readout nature. Scintillation light is produced over the whole width of the EL gap (5 mm in NEXT-DEMO) spreading the signal from a single electron over a time inversely proportional to the drift velocity within the gap ( $\sim 2 \mu\text{s}$ ). Additionally, the EL light is produced isotropically and, therefore, the signal produced by an electron going through the gap is expected to arrive at the tracking plane ( $\sim 7.5$  mm behind the anode) over the area defined by the intersection of the plane with the sphere of light [26].

In a previous paper [12], the NEXT collaboration demonstrated that a point-like deposition of charge due to the absorption of a  $K\alpha$  X-ray is expected to be detected over a transverse region which can be parameterised as a two dimensional Gaussian with a standard deviation of  $\sim 8$  mm where the spread due to EL light production is the dominant effect with subdominant contributions from the charge transverse diffusion. Longitudinally, the expected spread has a noticeable dependence on the drift distance since the diffusion dominates.  $K\alpha$  events are expected to have widths in  $z$  with standard deviations between 0.5 mm, for very short drifts, and 1.7 mm at the drift field settings used. In order to optimise the tracks reconstruction, these values must be taken into account by dividing the signal information into appropriate time slices and using charge information from clustered SiPM channels [26].

### 3.3.1 NEXT prototypes results

The NEXT Collaboration demonstrated the topological signature power in an EL xenon-based TPC using NEXT-DEMO prototype [26]. This prototype has been running since 2011 using several radiation sources with different characteristics.

The best energy resolution obtained in NEXT-DEMO, extrapolated to  $Q_{\beta\beta}$ , was 0.8 % FWHM, improving on the target defined in the paper TDR - Technical Design Report [91] of 1% FWHM at  $Q_{\beta\beta}$  with only basic corrections to the detected signals. The NEXT-DEMO has been providing perfect high voltage operation and a great stability against sparks. The gas system with hot getters has demonstrated to be leak-proof with continuous gas re-circulation and purification, measuring electron lifetimes up to tens of

milliseconds, demonstrating the getters efficiency, by removing the electronegative impurities from the gas when this is re-circulated [92]. The tracking plane with SiPMs was used to improve the results from [92] and it was observed a significantly increasing in the fiducial region size as it allowed a better understanding of events' topology. In those studies an high gas quality was also demonstrated and an electron lifetime of 10 ms was measured [89].

Latter, with the calculation of a corrected weighted sum of the observed energy resulted in a  $^{22}\text{Na}$  photopeak, an energy resolution of 1.62 % was obtained, which extrapolated to  $Q_{\beta\beta}$  becomes  $\sim 0.63$  % [12]. These values represent a slight improvement on previously published results [89].

There are two main effects affecting the energy resolution which were corrected during the data analysis. One effect is related with the electron trapping along the drift region, producing losses of ionisation electrons, reducing the electroluminescent light. The other effect is related with the PMTs, since there is a radial dependence of the EL light collection in the PMT plane, i.e. the detected number of photons (by the PMT plane) decreases with increasing the event radial position [43].

The reconstruction methods have been presented in [26]. Monte Carlo was found to reproduce the topological features in data to a high degree of accuracy for the track lengths and for the high energy blob candidate shown for data and Monte Carlo. The algorithm capabilities of topological signature and background rejection have demonstrated the adequate performance for the proposed NEXT-100 experiment, with an expected reduction of one order of magnitude in background [26]. It was measured a signal efficiency of  $66.7 \pm 0.9$  (stat)  $\pm 0.3$  (fit) % for a background acceptance of  $24.3 \pm 1.4$  (stat) % [26], which is in agreement with the Monte Carlo simulations. This study was particularly limited by the small size of the NEXT DEMO detector, where the event selection gave priority to less extended events, with a more difficult reconstruction.

Next-White is the NEXT-100 detector's first stage, working since 2016. Several calibration and background run measurements were performed with depleted xenon, and it was demonstrated the capability to achieve an energy resolution of  $\sim 1$  % FWHM at the xenon  $Q_{\beta\beta}$  [13, 93], which can still be improved, according to the published results at lower energies [12, 16]. In 2019 started the first run with xenon enriched in the isotope 136, aiming the measurement of the two neutrino double beta decay spectrum. The signal topological discrimination from its background has been explored with NEW. A signal efficiency of  $71.6 \pm 1.5_{stat} \pm 0.3_{sys}$  % was achieved for a background acceptance of  $20.6 \pm 0.4_{stat} \pm 0.3_{sys}$  % [94]. This result is an improvement to

the one reported in [26], thanks to the larger detector dimensions, as well as a better track reconstruction [94].

Several electron transport properties were studied with NEW, namely, the drift velocity, longitudinal and transverse diffusion. For the first time, all those parameter were measured simultaneously and with the same experimental setup. The agreement achieved is a proof that the use of pressure scaling for the diffusion parameters can be trusted for operating pressures up to  $\sim 10$  bar [95], suggesting that the dimers' role and higher order xenon clusters in electron transport will still be minor for higher pressures. The longitudinal diffusion measured in the NEXT-White calibration campaign was  $318.9 \pm 1.8_{stat} \pm 20.1_{sys} \mu\text{m}/\sqrt{\text{cm}}$ , while the transverse diffusion value is  $1279 \pm 3_{stat} \pm 40_{sys} \mu\text{m}/\sqrt{\text{cm}}$  [95]. The minimum 10 bar aiming pressure for the upcoming runs implies a longitudinal diffusion of  $267.3 \pm 1.5_{stat} \pm 16.9_{sys} \mu\text{m}/\sqrt{\text{cm}}$  and a transverse diffusion of  $1072 \pm 3_{stat} \pm 34_{sys} \mu\text{m}/\sqrt{\text{cm}}$  [95]. All these values are compatible with the design requirements and expectations for the NEXT-100 detector [8, 79, 91].

The internal Radon-induced background assumptions were validated in [88] for the data collected with the NEXT-White detector, whereas a first measurement was actually used to validate the Monte Carlo model for that inclusive background model [87]. The expected background in a 200 keV window around the  $Q_{\beta\beta}$  with  $^{136}\text{Xe}$  is  $0.75 \pm 0.12_{stat} \pm 0.02_{syst}$  in 37.9 days [87], achieved through the information on the events' topology. This topological selection allows a reduction in background of  $16.8 \pm 2.2$ , with the anode region being the main contribution for the remaining events [87]. Concerning the NEXT-100 design and installation, aiming the best achievable background levels, those data identified the anode region, i.e., the tracking plane, as the main area to be improved in upcoming works [87]. The use of a radon abatement system shown the negligibly of the backgrounds contribution, coming from airborne  $^{222}\text{Rn}$  to  $\beta\beta 0\nu$  [87].

### 3.4 Electron diffusion

Concerning the physical limitations, in a detector with a drift distance of one meter, the diffusion of the electrons in pure xenon will contribute with an effect of the order of  $\sim 10$  mm to the transverse resolution and  $\sim 4$ -5 mm to the longitudinal resolution, whereas the finer details of the track are lost, and by consequence the topological signature of the events will have a weaker effect. The physical nature of electron diffusion in pure xenon is the biggest concern for the spatial resolution and this is of the utmost importance for the two blobs topology identification [29].

In the figure 3.5 is shown the diffusion influence on the tracking plane of NEXT detector. There are presented simulated events for signal and for background with different electron diffusion applied. For 2 mm diffusion is still possible to see the details of the real track, whereas for 10 mm diffusion most of details are lost [29].

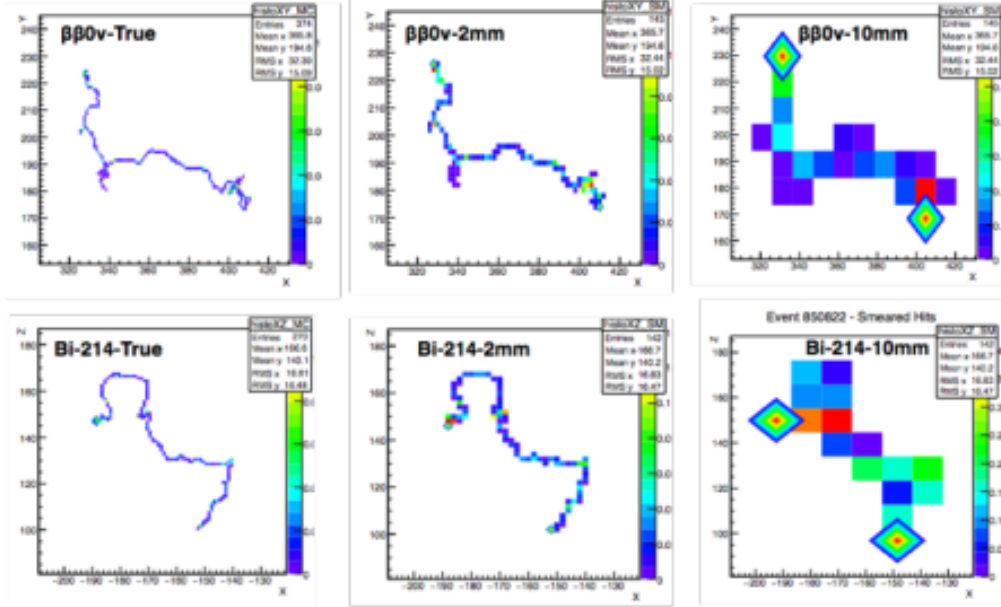


Figure 3.5: The effect of 2 mm (at the centre images) and 10 mm (at the right) diffusion where the details lost at the diffusion can be seen against the ‘true’ track [29].

When moving in a gaseous medium, the electrons scatter isotropically in random directions after each collision due to its light mass. When an electric field is applied, the electrons will then drift in the field direction with a mean drift velocity  $u$ , much smaller than  $v$ .

The diffusion is not isotropic anymore and along the electric field is observed a coefficient for longitudinal diffusion  $D_L$ , that can be different from  $D_T$ , the transverse diffusion. The electron medium energy also depends on the applied electric field intensity because this electrons are accelerated between collisions. Their mean energy given by  $\epsilon = \frac{mv^2}{2} = \frac{3kT}{2}$  will depend on the balance between the lost energy in each collision and the energy gained between them [96–100].

As xenon is a noble gas and it does not present any vibrational states, the drift electrons may perform only elastic collisions with the gas atoms. When the applied electric field is strong enough, the electrons will acquire more energy between collisions which may lead to another ways of energy transfer, exciting or ionising the gas atoms. This is why, at the drift region of a TPC, the electric field is kept below the excitation and ionisation thresholds but it still

has to be high enough in order to prevent ion recombination. In NEXT the applied  $E/p$  is smaller than 0.1 kV/cm/bar.

The possibility of event discrimination based on the topological signature of the ionisation trail depends on the progress achieved for the large electron diffusion in xenon due to the low electron drift velocity. The diffusion makes it difficult to describe in detail the ionisation trail for the drift distances in the NEXT detector and the discrimination based on the events topological signature loses effectiveness [27]. Due to interference effects, a deep minimum exists in the electron–atom elastic cross-section for collisions of electrons with argon, krypton, and xenon (but not for neon nor helium), known as the Ramsauer–Townsend (R-T) minimum. For xenon, the R–T minimum occurs near 1 eV. This quantum mechanical effect also has a substantial impact on electron transport, leading to rapidly varying diffusion characteristics in the eV range. The diffusion depends on both electric field and electron temperature [83].

### 3.5 Molecular additives

In elastic collisions with xenon atoms, the loss of energy of electrons is extremely inefficient because they are much lighter than the atoms and their average kinetic energy remains high, which increases the diffusion, especially at the range of the electric fields of interest. For molecular gases, even at low kinetic energies, new freedom degrees are created and available for energy transfer. This rises the idea of adding molecular gases to pure xenon, in order to allow the drift electrons to lose more energy between collisions.

The electron diffusion may be efficiently reduced, even with minute concentrations of molecular additives because the electron energy distribution may become mildly non-thermal, tending to build up around the energy of the first vibrational levels of molecular additives (usually  $\sim 0.1$  eV), demonstrated by simulation for  $\text{CO}_2$ ,  $\text{CF}_4$  and  $\text{CH}_4$ . These concentrations are below the sub-percent level, which implies a precise gas monitoring equipment [29].

Therefore, the addition of molecular gases to pure xenon is a solution to improve the spatial resolution in gaseous TPCs. Nonetheless, this will imply the scintillation parameters degradation of the HPXe TPC projected by the NEXT collaboration.

In order to be used in NEXT, a suitable gas mixture should previously fill some key requirements: from what concerns the primary and secondary scintillation, it should have low quenching, high transparency to VUV light and low electron attachment; in the drift region, for low electric fields, the

mixture needs to have low charge recombination and a high efficiency electron cooling in order to reduce the electron diffusion. Those molecular species also need not to be reactive with the detector materials, easy to handle (not to be toxic nor explosive) and its mixture with xenon should be easy to purify and also be compatible with the use of getters.

It is known from previous studies that molecular additives, even at low concentrations, degrade the energy resolution and amplification performance of EL detectors. When the electron probability to collide with molecules becomes significant it means that the electrons may lose energy for vibrational or rotational excitations and they won't be able to produce electroluminescence. Studies with argon may be consulted in [101, 102] and related studies in [103–105].

### 3.5.1 Scintillation with molecular additives

The performance of scintillation processes could be affected by the addition of molecular species. In the NEXT experiment, the primary scintillation is used as trigger, so it has to be noticeable after gas molecular addition and the secondary scintillation needs to be strong enough, since it provides information about the event energy and its fluctuations should be as low as possible after adding molecular species to the gas.

The most relevant parameters for NEXT which could be affected by the addition of molecular species are the energy resolution and the electroluminescence yield.

Although the electrons cooling in mixtures is efficient due to vibrational excitations with molecules of the gas, for the same electric field, the energy of electrons is lower for gas mixtures, and by consequence the number of xenon excitations will be lower, reducing also the EL yield ( $\bar{N}_{EL}$ ).

Molecular additives may be electronegative, providing the occurrence of attachment, and the  $\bar{N}_{EL}$  is reduced, so the fluctuations in its value may be bigger. It is necessary that the electrons reach a well defined energy range to become attached and, for the studied molecular additives, the probability of this to happen in the EL gap is bigger than under the effect of the drift electric field. Anyway, for the large drift region of NEXT, this mechanism might reduce the number of primary electrons.

The quenching effects may also contribute for the reduction of  $\bar{N}_{EL}$  in mixtures because the excited atoms, which are produced in the secondary scintillation process can be deactivated by two or three body collisions with the molecular additive inhibiting the formation of scintillation emitting xenon dimers. The probability of quenching mechanisms may vary with the absolute pressure of the gas.

### 3.5.2 Previous studies with molecular additives

#### EL yield

From [101] it is expected that the presence of molecular species in a noble gas would dramatically reduce the EL yield.

From the experimental measurement performed with Xe-CO<sub>2</sub>, Xe-CH<sub>4</sub> and Xe-CF<sub>4</sub> mixtures, there is a linear dependence between the EL reduced yield and the reduced electric field. The figure 3.6 presents  $Y/p$  as function of the reduced electric field ( $E/p$ ) applied to the scintillation region, for different concentrations of the mentioned molecular gases added to pure xenon.

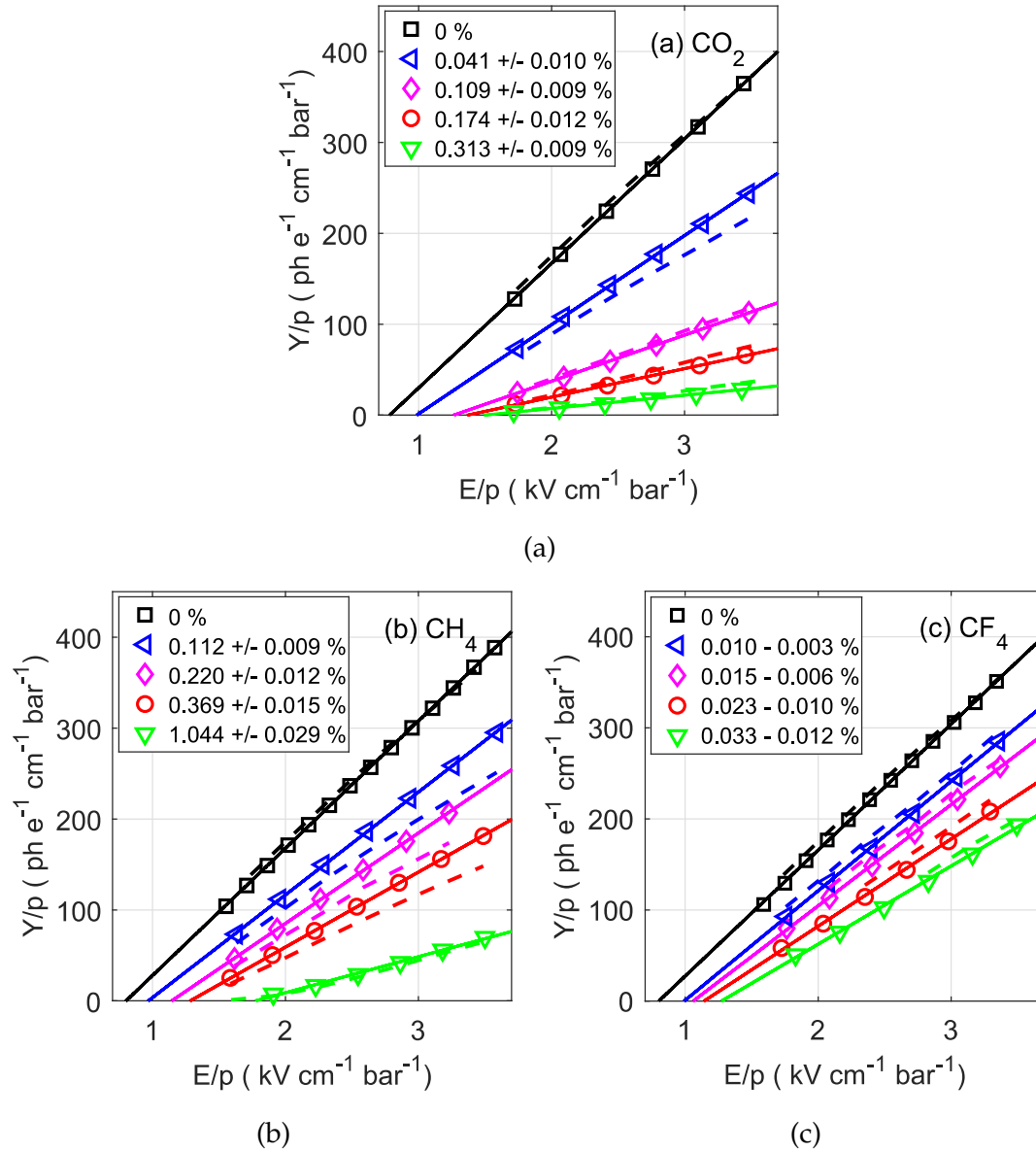


Figure 3.6: Reduced EL yield obtained for 5.9 keV x-rays,  $Y/p$ , as a function of the reduced electric field,  $E/p$ , for different types and concentrations of molecular gases added to pure xenon: (a) CO<sub>2</sub>; (b) CH<sub>4</sub>; (c) CF<sub>4</sub>. Total pressures of 1.13, 1.25 and 1.24 bar were used, for Xe-CO<sub>2</sub>, Xe-CH<sub>4</sub> and Xe-CF<sub>4</sub> mixtures, respectively. Solid lines show linear fits to the data, while dashed lines are simulation values obtained with the code developed in [31]. Results taken from [32].

The EL yield decreases as the additive concentration increases for all three additives, for the same E/p value.

As an example, it was observed that for a reduced electric field of 2.5 kV/cm/bar in the TPC there is a 50 % drop in EL, compared to pure xenon results, for concentrations of 0.05 % CO<sub>2</sub>, 0.3 % CH<sub>4</sub> and 0.02 % CF<sub>4</sub>.

However, the EL reduction may be acceptable for specific concentrations of each additive in cases where the energy resolution is not compromised and the secondary scintillation is large enough. For those concentrations, the EL threshold increases with the increase of additive concentration in gas and the slope of EL reduced yield decreases. For concentration values up to 0.1 % for CO<sub>2</sub>, 0.4 % for CH<sub>4</sub> and 0.02 % for CF<sub>4</sub>, the reduction of the EL yield and its respective statistical fluctuations are still acceptable, being the electron cooling efficiently reduced almost to the thermal limit for these concentrations. This behaviour in the secondary scintillation threshold reveals the efficiency of electron cooling until concentration values of 0.1 % for CO<sub>2</sub>, 0.4 % for CH<sub>4</sub> and 0.02 % for CF<sub>4</sub>. Those results have then proven that there is a possible compromise between electron cooling and excimer quenching [32].

### Energy resolution

It were performed Magboltz simulations for xenon at 10 bar for different concentrations of CO<sub>2</sub>, CH<sub>4</sub> and CF<sub>4</sub>, whose elementary cross-sections are well known. For those simulations both transverse and longitudinal diffusion were studied, as it were the drift velocity and the effects on the amount of light produced in the EL region and the energy resolution for different electric fields [29]. These molecules are highly transparent to xenon scintillation, except CO<sub>2</sub>, for which, at the concentrations studied, the transparency for 1 m length can be as low as 50 % [29].

In figure 3.7, the energy resolution extrapolated for the NEXT-100 TPC for an EL field of 2.5 kV/cm/bar is plotted as a function of 3D diffusion, defined as the characteristic size of the electron diffusion ellipsoid,  $\sqrt[3]{xyz}$  after 1 m drift through the TPC,  $D_{3d} = \sqrt[3]{D_L \times D_T^2}$  (mm/ $\sqrt{m}$ ), for the three additives at several concentrations. This diffusion was obtained from Magboltz simulations for a drift field of 20 V/cm/bar by [106]. The shadowed areas represent the error intervals from experimental measurements. The energy resolution (ER) uncertainty is also affected by the error bars of Q-factor (see below), as well as systematic errors in Xe-CO<sub>2</sub> and Xe-CF<sub>4</sub> performed mixtures. There is still a possible overestimation of Q-factor in the attachment-inducing mixtures, as suggested by the results in this same work [106].

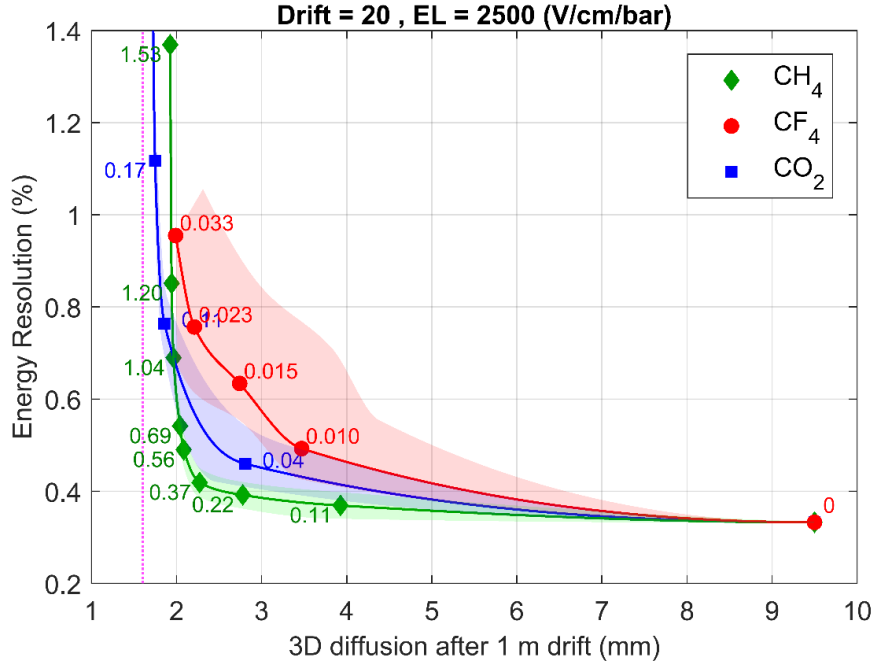


Figure 3.7: Energy resolution extrapolated for NEXT-100 for the  $\beta\beta 0\nu$  energy as function of 3D diffusion for the labelled additive concentrations, with a drift reduced electric field of 20 V/cm/bar and and EL reduced electric field of 2.5 keV/cm/bar [106].

When the three additives are compared between concentrations for which the electron diffusion is equally reduced, CF<sub>4</sub> reveals to be the worst additive, despite showing smaller deterioration on the EL signal intensity. For the used operating conditions, CH<sub>4</sub> is clearly the most promising candidate for NEXT-100, at least within the region of interest, i.e.  $D_{3d}$  between 2 and 3 mm/ $\sqrt{m}$ . This tendency seems to be well established, even considering the large errors represented by the shadowed areas. CO<sub>2</sub> may also be a viable additive, although it does not overtake CH<sub>4</sub>. In addition, the energy resolution is further degraded in CO<sub>2</sub> through the Q-factor [106]. For those studies, the energy resolution wasn't significantly affected, since the statistical fluctuations linked to EL production were a 6 factor lower than the Fano factor contribution and for higher concentrations, the intrinsic resolution deteriorates with the increase of CO<sub>2</sub> amount [30, 32].

Studies from [32] also present the results of the impact that molecular additives (CO<sub>2</sub>, CH<sub>4</sub> and CF<sub>4</sub>) have on the energy resolution by comparison to pure xenon. For concentrations until 0.1 % CO<sub>2</sub> and 1 % CH<sub>4</sub> the energy resolution is not significantly degraded and for high electric fields CH<sub>4</sub> presented the best results. For CF<sub>4</sub> the energy resolution is strongly degraded, even for concentrations around 0.02 %. For this additive the pulse height distribution was shown to be asymmetric in the right side, due to electron attachment, getting worse for higher concentrations [32]. It were also performed simulations, for the same additive concentrations, at this time, for

the operation conditions of NEXT-100 TPC [31]. The best compromise between energy resolution and electron diffusion is  $2.75 \text{ mm}/\sqrt{m}$  for the concentrations of additives of 0.04 %  $\text{CO}_2$ , 0.2 %  $\text{CH}_4$  and 0.015 %  $\text{CF}_4$ .

Nevertheless, it was found that for a long time operation of  $\text{CO}_2$  mixtures, these molecules reveal to be unstable due to the absorption in getters, leading to CO formation. This is a major problem for the use in a large chamber and for long time operations. For  $\text{CH}_4$  and  $\text{CF}_4$  the getters temperature has to be reduced in order to prevent the break and absorption of this molecules. This could be a drawback since it may jeopardise the gettering efficiency of the gas in the TPC [32].

For  $\text{CO}_2$  also were achieved good energy resolution values but its performance is affected by the low transparency and by the long term instability. For  $\text{CF}_4$ , although the low quenching effect, the electron attachment affects the energy resolution. The energy resolution is better for  $\text{CH}_4$ , even having shown high quenching effects, becoming the best molecular candidate to be used in NEXT-100 TPC so far.

The latter will be the first additive to be studied in NEXT-DEMO detector. The simulations revealed that both Q-factor and PMT signal fluctuations can be kept at the level of Fano factor for 10 bar and at the concentration mentioned above in order to remain the diffusion at  $2.75 \text{ mm}/\sqrt{m}$ . Concerning the primary scintillation yields, it is expected a reduction of a 5-10 factor for the same concentrations [31].

## Q-factor

Regarding the production of scintillation, these fluctuations are described by  $J = \frac{\sigma_{EL}^2}{\bar{N}_{EL}}$ , the fluctuations in the number of EL photons produced per primary electron, described as the ratio between the variance in the number of emitted photons per primary electron, and the variance considering that the process is described by the Poisson model, i.e., the average number of photons per primary electron. This J parameter can also be described by  $Q = J/\bar{N}_{EL}$  in the literature.

The fluctuations related with the productions of scintillation, J, are much smaller than those related with the generation of primary charges, F, in pure xenon, being the number of produced photons per primary electron high. Therefore, the energy resolution is, in most of the cases, explained by the fluctuations in the primary electron cloud arrangement and the fluctuations related to the photon detection system.

The higher  $N_{ep}$  (i.e., average number of primary charges produced in APD, by number of photons), proportional to  $\bar{N}_{EL}$  (i.e., average number of EL photons produced by primary electron) and  $\bar{N}_e$  (i.e., average number of

primary electrons produced by x-ray), the lower will the energy resolution be. This is the reason why strong electric fields are preferred, since more photons per primary electron are produced. Still, the J fluctuations become bigger above the charge multiplication threshold.

The relative variance in the number of EL photons produced per primary electron in the EL region ( $Q$ ) was calculated by [32], varying the reduced electric field in the region of interest, for all three additives. For pure xenon,  $Q$  is negligible and its value increases with the amount of molecular additive.

For  $\text{CO}_2$ ,  $Q$  has revealed not to be strongly dependent on the reduced electric field, keeping under the Fano factor up to concentrations of 0.1 %. It was expected that the  $Q$ -factor had decreased with the rise of EL electric field and this did not happened for  $\text{CO}_2$ , whose effect is probably due to dissociative electron attachment with the additive molecules [32].

For  $\text{CH}_4$  there is a clear dependence of  $Q$  with the reduced electric field ( $E/p$ ) and for concentrations below 1 %, the  $Q$ -factor becomes negligible ( $< 0.05$ ) for  $E/p$  values above 2.5 kV/cm/bar. This explains the good results obtained for energy resolution with  $\text{CH}_4$  from figure 3.7. For  $\text{CF}_4$ ,  $Q$  becomes higher than Fano factor for concentrations as low as 0.01 %, increasing abruptly with increasing concentrations [32].



# Chapter 4

## Electroluminescence in noble gases

There are two signals of major interest to study in the NEXT TPC, namely, the primary scintillation and the secondary scintillation. The first is produced by highly energetic charges while interacting with xenon atoms and is used in order to establish the start-of-event trigger, whereas the second is produced in the electroluminescence region by electrons, providing information on the event energy. Therefore, fluctuations in this latter signal are a factor to minimise as much as possible.

### 4.1 Primary scintillation

In pure xenon, the primary scintillation is produced while the primary electron cloud is being formed, following the absorption of radiation and the thermalisation of the resulting ionisation electrons.

When energetic charged particles cross a volume of gaseous xenon, its atoms can be ionised or excited by those particles producing a wide distribution of xenon excited states that quickly will end up on both the lowest metastable state ( $^3P_2$ ) and the resonant state ( $^3P_1$ ) [97]. For pressures above tens of mbar, the main process around which the excited atoms will depopulate is through three-body collisions with ground state xenon atoms, creating excimers [107], as described by:



with  $Xe^*$  the excited state of a xenon atom and  $Xe_2^{**}$  the created excimer. However, for pressures above 400 mbar, the excimers quickly lose their highly vibrational energy through collisions with ground state atoms, as stated by [108], then:



In turn, the lowest vibrational states will decay and emit a scintillation photon

[109]:



being  $hv$  the scintillation photon. These photons will form a vacuum ultraviolet continuum, the so-called second continuum, centred at 172 nm, with a FWHM of 14 nm [108].

Thus, a sufficiently high electric field ( $E/p > 6$  V/cm/bar) is applied in the TPC drift region [110], in order to avoid recombination of electrons. Nevertheless, for particles experiencing high energy loss per unit of path length, electron-ion recombination still could occur. Going further, this is a process consisting in the formation of a molecular ion ( $Xe_2^+$ ) in three body collisions and the consequent electron thermalisation through elastic collisions, excitation or ionisation, leading to dissociative recombination:



Then, when the relaxation of the resultant highly excited atom takes place, giving rise to a xenon atom on its excited state and heat release, the reactions previously mentioned can also occur, leading into a VUV photon emission in the xenon second continuum [111]. Nevertheless, the recombination is expected to be minimal in the NEXT experiment due to low ionisation charge density generated in the beta emission.

The signal amplitude of primary scintillation is very low and, thus, it is hard to distinguish from the noise background. Nevertheless, the detection of primary scintillation is the most convenient way to obtain the  $t_0$  needed to place an event properly in a three-dimensional space in a TPC [83], as referred in chapter 3.

The average energies needed to produce a VUV photon,  $w_s$ , and an electron pair,  $w_i$ , are both used to quantify the primary scintillation and ionisation yields. A  $w_i$  value of  $22 \pm 1$  eV, using x-rays, gammas or electrons, was reported by [112–114], whereas the  $w_s$  value reported in the literature is in the range of 34–111 eV [14, 31, 92, 115], with the lower values having been obtained with alpha particles and the higher values using x-rays. This is a tendency that is still not fully understood.

## 4.2 Secondary scintillation

The electric field applied to the drift region is also used to drive the electrons to the EL amplification region. The secondary scintillation happens when the thermalized free electrons acquire enough kinetic energy between collisions with the atoms, in order to cause excitation of the atoms, through

inelastic collisions. Since these are low energy electrons, xenon is predominantly excited in the lowest metastable,  $^3P_2$ , and resonant,  $^3P_1$ , states. Thus, the aforementioned de-excitation processes involved in the primary scintillation will happen here as well. Finally, the VUV photon emission in the xenon second continuum ( $\sim 172$  nm) promoted by the low energy electron impact when accelerated under an external electric field is the so-called electroluminescence or secondary scintillation. Despite the photon emission also happening in the 829-885 nm range [116], the VUV continuum is one order of magnitude more intense than the near infrared one, although most of the photosensors are not even sensitive in this range.

As the lost energy in elastic collisions is really small, the electroluminescence process is very effective, since the energy acquired by the electrons from the electric field is efficiently spent exciting the xenon atoms ( $\sim 95$  % efficiency), and, afterwards, producing VUV photons in the de-excitation processes. References [20, 102] refer to excitation efficiencies of  $\sim 95$  % and photon production efficiencies of  $\sim 80$  %, for an applied E/p value of 4 kV/cm/bar. Nonetheless, this efficiency is decreased for lower applied electric fields ( $< 2$  kV/cm/bar). The scintillation threshold for which the electrons have no longer enough energy to excite the xenon atoms occurs around  $E/p < 0.76$  kV/cm/bar [18].

More detailed information on the xenon electroluminescence, as well as another noble gases can be found in the following theoretical and experimental studies [14, 20, 24, 102, 108, 117, 118].

#### 4.2.1 Electroluminescence yield

The reduced electroluminescence yield ( $Y/p$ ) is defined as the average number of VUV photons emitted per primary electron and per unit of drift length of electrons in the scintillation region, divided by the gas pressure. The reduced electric field ( $E/p$ ) is the ratio between the electric field intensity and the gas pressure.

EL yield can be represented as a function of the applied electric field ( $E$ ). Nonetheless, this relation depends on the gas atomic density ( $N$ , i.e. the number of atoms per unit of volume) due to the increase in energy that is transferred to the electrons by the electric field between their collisions, as its mean free path becomes longer with decreasing pressure or gas density. Thus, both parameters are usually normalised to the number of atoms per volume unit,  $N$ . Therefore, the relation between the reduced yield ( $Y/N$ ) and the reduced electric field ( $E/N$ ) is valid for any macroscopic conditions of the gas phase. For convenience, this normalisation is sometimes performed to the gas pressure,  $p$ , instead. Nevertheless, in such cases, the gas temperature is a

parameter to be considered as well, since  $N$  depends on both temperature and pressure.

Between the excitation and ionisation thresholds, the  $Y/p$  as a function of  $E/p$  is nearly linear, since the amount of energy gained by the electron is directly proportional to the electric field. For low electric fields, a deviation from the linear trend arises due to a reduction of EL efficiency with  $E/p$  that is sharper for values below  $E/p \sim 2 \text{ kV/cm/bar}$ . For  $E/p$  values above the ionisation threshold, the electroluminescence yield has an exponential growth with the increase on the reduced electric field, following the exponential growth on the number of free electrons available for EL production. The linear trend was already measured experimentally in pure xenon and was described by [18] as:

$$\frac{Y}{p} \left( \text{photonselectron}^{-1} \text{cm}^{-1} \text{bar}^{-1} \right) = 140 \frac{E}{p} (\text{kVcm}^{-1} \text{bar}^{-1}) - 116 \quad (4.5)$$

The scintillation threshold was reported to be  $\sim 0.76 \text{ kV/cm/bar}$  and the ionisation threshold  $\sim 4.6 \text{ kV/cm/bar}$  [18].

### 4.3 Energy resolution

The energy resolution is the main key to delimit the intrinsic background in the TPC, the events from the double-beta decay with neutrino emission and the events from natural radiation origin entering the region of interest [26].

The energy measurement is provided by electroluminescence detection, i.e., the process of secondary light emission, which was demonstrated to be a very good option to embrace in order to achieve excellent energy resolution [119]. Furthermore, this technique provides large signals with negligible electronic noise, being an optimum amplification technique for an experiment of this nature, with very low event rates and high background levels [14].

The energy resolution of an EL-based detector like the gas proportional scintillation counter (GPSC) readout by a Large Area Avalanche Photodiode (LAAPD) used in this work is determined by the statistical fluctuations in the primary ionisation processes, in the production of EL scintillation and in the photosensor. Since these contributions are statistically independent, the variance of the total energy resolution can be obtained by summing the variances of the above contributions.

When x-rays with energy  $E_x$  are absorbed in xenon, an average number of primary electrons ( $\overline{N}_e$ ) is produced:

$$\overline{N}_e = \frac{E_x}{w} \quad (4.6)$$

where  $w$  is the mean energy required to produce a primary electron in xenon, with  $w \sim 22.4$  eV [120, 121].

As the primary electrons traverse the GPSC scintillation region, they produce an average number of scintillation photons per electron,  $\bar{N}_{EL}$ . A fraction of these scintillation photons will strike the active area of the photosensor, releasing an average number of primary charges inside the photosensor ( $\bar{N}_{pe}$ ).

The output signal of avalanche photodiodes can be affected by several fluctuation sources: statistical fluctuations associated with the number of electron-hole pairs created in silicon,  $N_{pe}$ , and with the avalanche process; gain non-uniformity in the Avalanche photodiode (APD) detection volume; and the dark noise of the diode-preamplifier system. The non-uniformity contribution to the statistical fluctuations is negligible for light detection, since the whole area of the LAAPD is irradiated and the final pulse results from an average response to the full amount of photons interacting in the photosensor. For the GPSC and LAAPD operation conditions used in this work, the dark noise contribution is also expected to be negligible, when compared to the remaining contributions [122]. Accordingly, the variance of the LAAPD output signal ( $\sigma_S^2$ ) is dominated by the fluctuations in charge-carrier creation and in avalanche multiplication [123, 124]:

$$\sigma_S^2 = \sigma_{N_{pe}}^2 + \bar{N}_{pe} \frac{\sigma_G^2}{G^2} \quad (4.7)$$

where  $G$  and  $\sigma_G^2$  are the LAAPD gain and respective variance. For light pulse detection, fluctuations on the number of primary electrons are described by Poisson statistics, as follows  $\sigma_{N_{pe}}^2 = \bar{N}_{pe}$ . Hence, equation 4.7 can be simplified into:

$$\sigma_S^2 = \bar{N}_{pe} f \quad (4.8)$$

with  $f$  being defined as the excess noise factor,  $f = 1 + \sigma_G^2/G^2$ . Since the multiplication process in the LAAPD results in electron avalanche fluctuations,  $f$  is higher than 1, depending on the LAAPD gain. In ref. [124], a  $f$  value of approximately 2 was estimated for a 16mm-diameter LAAPD operated at a gain of 150, being these the same specifications of our LAAPD.

Considering the aforementioned approximations, the energy resolution can be given by [24, 120]:

$$R_E = 2\sqrt{2\ln 2} \sqrt{\frac{\sigma_e^2}{\bar{N}_e^2} + \frac{1}{\bar{N}_e} \left( \frac{\sigma_{EL}^2}{\bar{N}_{EL}^2} \right) + \frac{\sigma_{pe}^2}{\bar{N}_{pe}^2} + \frac{1}{\bar{N}_{pe}} \left( \frac{\sigma_G^2}{G^2} \right)} \quad (4.9)$$

with the first term related with fluctuations in the number of primary

electrons produced per x-ray interaction ( $N_e$ ), the second term is related to fluctuations in the number of EL photons,  $N_{EL}$ , produced per primary electron and the last two terms are related to the main fluctuation sources in the photosensor, i.e. in the number of photoelectrons produced in the LAAPD by EL per x-ray interaction in the gas and in the number of collected electrons in the APD anode per photoelectron produced in the LAAPD (the APD gain,  $G$ ).

The fluctuations in  $N_e$  and in  $N_{EL}$  are not purely statistical, leading to a relative variance lower than that expected from the Poisson statistics. The Fano factor,  $F$ , and the  $J$  parameter are defined as the relative variance of  $N_e$  and  $N_{EL}$ , respectively. Thus, the above equation can be written as

$$R_E = 2\sqrt{2\ln 2} \sqrt{\frac{F}{\bar{N}_e} + \frac{1}{\bar{N}_e} \left( \frac{J}{\bar{N}_{EL}} \right) + \frac{\sigma_{pe}^2}{\bar{N}_{pe}^2} + \frac{1}{\bar{N}_{pe}} \left( \frac{\sigma_G^2}{G^2} \right)} \quad (4.10)$$

Within the reduced electric field region of interest of NEXT (1.5-3.5 kV/cm/bar), the second term in equation 4.10 is expected to be negligible, since  $N_{EL} > 100$  and  $J \ll F$ , both in pure xenon and xenon-helium mixtures [34]. Therefore, the expression for the energy resolution can be simplified into:

$$R_E = 2.355 \sqrt{\frac{F}{\bar{N}_e} + \frac{f}{\bar{N}_{pe}}} \quad (4.11)$$

If the reflections of scintillation photons on the GPSC materials and LAAPD window are neglected,  $\bar{N}_{pe}$  can be computed as follows:

$$\bar{N}_{pe} = \bar{N}_e \bar{N}_{EL} Q_e \frac{\Omega}{4\pi} \quad (4.12)$$

with  $\Omega$  being the solid angle subtended by the photosensor active area, and  $Q_e$  is the photosensor effective quantum efficiency. For the dimensions of our detector and photosensor, the average  $\Omega/4\pi$  along the EL gap (0.8 cm) is 0.23, which includes the anode grid optical transparency. The effective quantum efficiency (i.e. including the window transmission and intrinsic quantum efficiency) of our LAAPD for the xenon second continuum scintillation is approximately 1.05 according to the manufacturer [125]. The quantum efficiency is higher than 100% in this photosensor because VUV photons have enough energy to produce more than 1 electron-hole pair.

The first term in equation 4.11 does not depend on the detector readout technology, hence being often defined as the detector intrinsic energy resolution ( $R_{int}$ ):

$$R_{int} = 2.355 \sqrt{\frac{Fw}{E_x}} \quad (4.13)$$

On the other hand, the second term depends on both the photosensor and the number of produced EL photons, with the latter being directly proportional to the reduced electric field, as demonstrated in equation 4.5. If both sides of equation 4.11 are squared, and the definition of intrinsic energy resolution is used, a simple linear relation can be obtained:

$$R_E^2 = R_{int}^2 + \frac{2.355^2 w f}{E_x a} \frac{1}{N_{EL}} \quad (4.14)$$

where  $1/N_{EL}$  and  $R_E^2$  are the dependent and the independent variables, respectively and  $a$  is a constant equal to  $Q_e \frac{\Omega}{4\pi}$ . Therefore, by measuring the overall energy resolution for different reduced electric fields applied in the EL region,  $R_E^2$  can be plotted as a function of  $1/A$ , whereas  $A$  is the LAAPD signal amplitude, being directly proportional to  $N_{EL}$ . In this way, according to equation 4.14, the detector intrinsic energy resolution,  $R_{int}$ , and consequently, the Fano factor,  $F$ , can be estimated from the y-interception of a straight line fitted to data, i.e. at the limit of infinite light yield. This method has been successfully exploited in GPSCs, and is similar to the one used in the present work [24, 126].



# Chapter 5

## Helium

Helium used as an additive in xenon presents the potential to improve the desired topological signature in HPXe TPCs. It is intended to achieve a compromise in order to have enough helium, so it allows the electron diffusion reduction, and the smallest possible amount of helium, so it becomes possible to avoid additional pressure, without loose the source isotope inside the TPC, in order to attain a good sensitivity.

The choice of helium as an additive brings several advantages, such as the easiness to handle, and it is free of light quenching effects (i.e. the light suppression in the scintillation yield with xenon). As a noble gas it is free from vibrational and rotational states, as well as dissociation, by comparison with molecular additives. The scintillation yield is not significantly affected, since there are no energy losses to those vibrational and rotational states and the drift velocity can be twice higher than in pure xenon as well. Although having a minimum impact, it is still positive, in the data acquisition process.

In the drift region, the primary electrons attain a static equilibrium while drifting in a noble gas and the energy gained from the electric field is in balance with the energy lost in elastic collision with the gas atoms. Thus, the helium may be a mechanism to significantly reduce the electron cloud diffusion caused by pure xenon, allowing the electrons to cool down efficiently, due to its very small mass, when compared to xenon [29].

Moreover, for the concentrations in study, at  $\sim 2$  bar for a total of 10-15 bar, helium is a convenient way to detect leaks in the system, since it will easily escape in the case of existing microleaks, thus, with the detection of helium it is possible to prevent xenon losses as well. Furthermore, as a noble gas, the helium is chemically inert and uses the same purification system as xenon, being easily separated from each other. This allows the xenon recovery after the mixture procedure, simply by cooling, using liquid nitrogen, once the boiling temperature for helium is 4.22 K, xenon has a fusion temperature at 161.4 K and the liquid nitrogen has its ebullition point at 77 K.

The use of photomultipliers, in its turn, in a detector with helium filling might be a problem, since the helium can permeate through the PMT and damage it. Although, this can be avoided by shielding the PMT in vacuum with a sapphire window, which is impermeable to helium. Another alternative is the use of SiPMs instead of PMTs, which also simplifies the mechanical design.

## 5.1 Previous studies with helium

### 5.1.1 Diffusion

It has been noted that the addition of small concentrations of helium, namely 10-15 %, to high-pressure xenon may reduce the transverse electron diffusion from  $10.5 \text{ mm}/\sqrt{m}$  in pure xenon down to  $2.5 \text{ mm}/\sqrt{m}$ , while imposing only a relatively small effect on longitudinal diffusion remaining around  $4 \text{ mm}/\sqrt{m}$  [34].

#### Transverse diffusion

The electron energies under the typical drift fields operated in TPCs are far from the excitation levels of the noble gas atoms, which implies that electron-atom collisions are elastic. Thus, by using a classical kinematic calculation of two body collisions, an accurate estimate for the momentum transfer is allowed, whereas the momentum transfer efficiency depends on two bodies mass ratio.

It is expected the total energy loss of electrons remains approximately constant as the cross section at very low energies becomes larger for xenon than for helium atoms, due to its larger mass. However, the existence of the Ramsauer minimum [127] for xenon cross section, depicted in the figure 5.1a, is balanced with the addition of helium, neutralising the difference in atoms' mass, thus making the overall cooling of xenon-helium mixtures to be more effective in that region.

Therefore, the transverse diffusion is the dominating factor in the global 3D diffusion, which can be reduced in the presence of additives, being weakly affected by the electric field. The transverse diffusion coefficient is shown in fig 5.1b as a function of helium concentration, performed by simulation in [34].

From simulation studies, a transverse diffusion of  $2.5 \text{ mm}/\sqrt{m}$  is predicted for 15 % helium in xenon, using a field range of 300-500 V/cm. This parameter is weakly affected by the electric field, unlike the longitudinal diffusion discussed forward. This is an improvement with respect to pure xenon, whose transverse diffusion is  $10.5 \text{ mm}/\sqrt{m}$ . Thus, it is believed that

for a drift distance of 1 meter, the addition of 10-15 % successfully reduces the transverse diffusion effects [34].

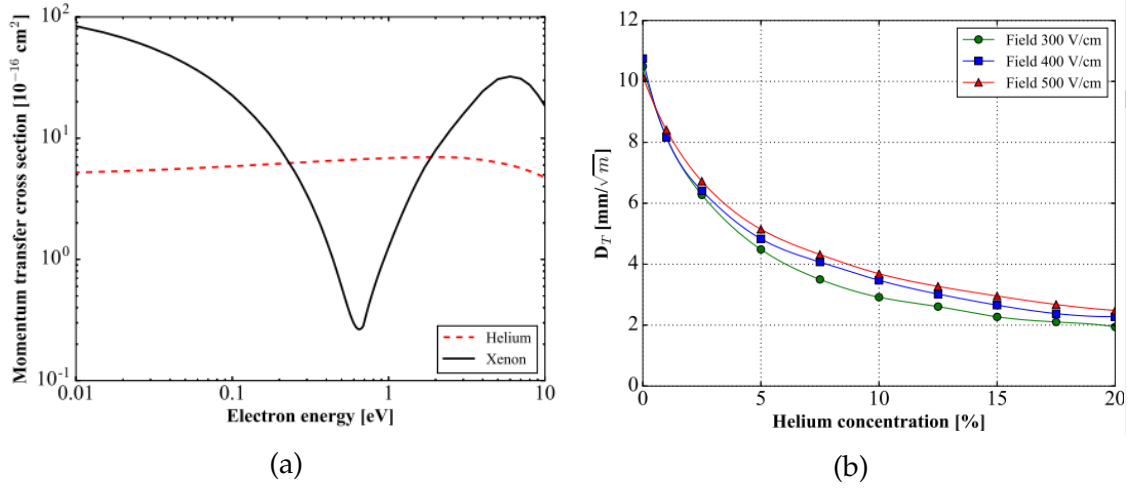


Figure 5.1: Left: Cross section of electron-xenon and electron-helium as function of electron energy [128]. Right: Transverse diffusion coefficient as function of helium concentration in xenon-helium admixtures [34].

MagBoltz simulations [129] verified that the Wannier relation is expected to be applied in the region of interest, 20-50 V/cm-bar for xenon-helium mixtures.

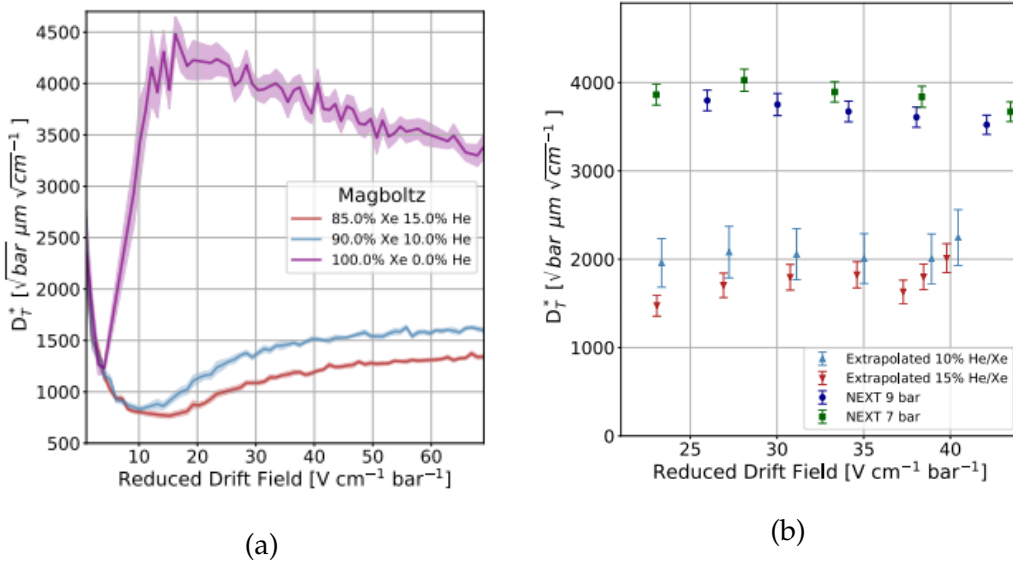


Figure 5.2: Left: Dependence of the reduced transverse diffusion coefficient on helium concentration predicted with Magboltz simulations. The line represents the value from the simulation and the shaded region is the error in the simulation. Right: Extrapolated transverse diffusion in pure xenon, compared to experimental data from NEXT-NEW TPC [35].

Figure 5.2a presents the results for the transverse diffusion from Magboltz for these admixtures with 10-15 % helium, while the results presented by [35] from the extrapolated transverse diffusion values, assuming the Wannier

relation on DL experimental data, for those same mixtures are depicted in 5.2b, leading to the conclusion that helium additives have potential to offer a factor of  $\sim 2$  improvement in terms of transverse diffusion control.

### Longitudinal diffusion

The electron cloud will scatter along the drift direction due to thermal diffusion. In the eV range, regarding the cloud centroid, the forward electrons will have higher velocities than the average, increasing the collisions frequency, thus reducing their instantaneous velocity, while the delayed electrons will experience fewer collisions, carrying bigger instantaneous velocity along their drift. These effects will squeeze the electron cloud, reducing the longitudinal diffusion.

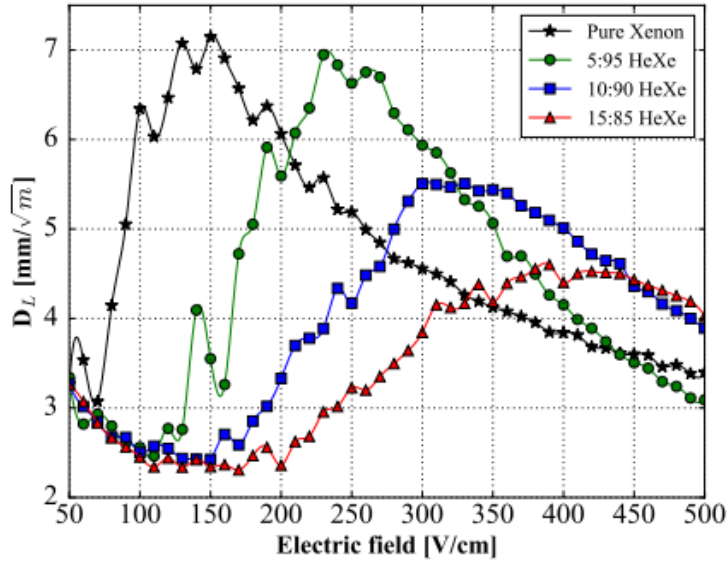
With helium admixtures the Ramsauer effect seems to be much broader than an actual peak, since the Ramsauer minimum of xenon is not dominant, Fig. 5.1a. In order to lower the longitudinal diffusion, for any admixture, it is required an electric field  $\sim 500$  V/cm (high enough), since, for example, with a mixture with 15 % helium, its 'Ramsauer induced peak' reaches a maximum at 400 V/cm. Thus, the electron's longitudinal diffusion is much more affected by the applied electric field than the transverse one.

Figure 5.3a, depicts the longitudinal diffusion variation as a function of electric field, presenting the simulation results from [34] for the several concentrations of helium in xenon. From these results, it is notable that in mixtures with 15 % helium, in the interest field range, the diffusion is substantially lower, relatively to pure xenon ( $4 \text{ mm}/\sqrt{m}$ ). For comparison, figure 5.3b presents experimental results achieved by [35] for the longitudinal diffusion.

A larger value for the  $D_L$  coefficient than previous theoretical predictions [129] was observed by [35] for both pure xenon and xenon-helium mixtures. Whereas in pure xenon a much pronounced rise was found at mid to low  $E/p$ , for helium mixtures, in concentrations of 10 % and 15 %, a similar effect appears at higher values of  $E/p$  than observed for pure xenon [35].

From these results it is believed that longitudinal diffusion was under-predicted for pure xenon at very low  $E/p$  and at higher  $E/p$  in mixtures with helium, for all relevant electric fields and pressures studied in that work. However, regarding the consequences of the helium cooling effect on the drift electrons, leading them to have lower average energies, those will result in the shifting to higher  $E/p$  in xenon-helium mixtures and the same impact is shown on the electron-xenon cross section at lower  $E/p$  [35].

Therefore, previous results from [35] reveal that the addition of helium at the 10-15% level will increase by around 50 % the longitudinal diffusion scale, when compared with pure xenon.



(a)

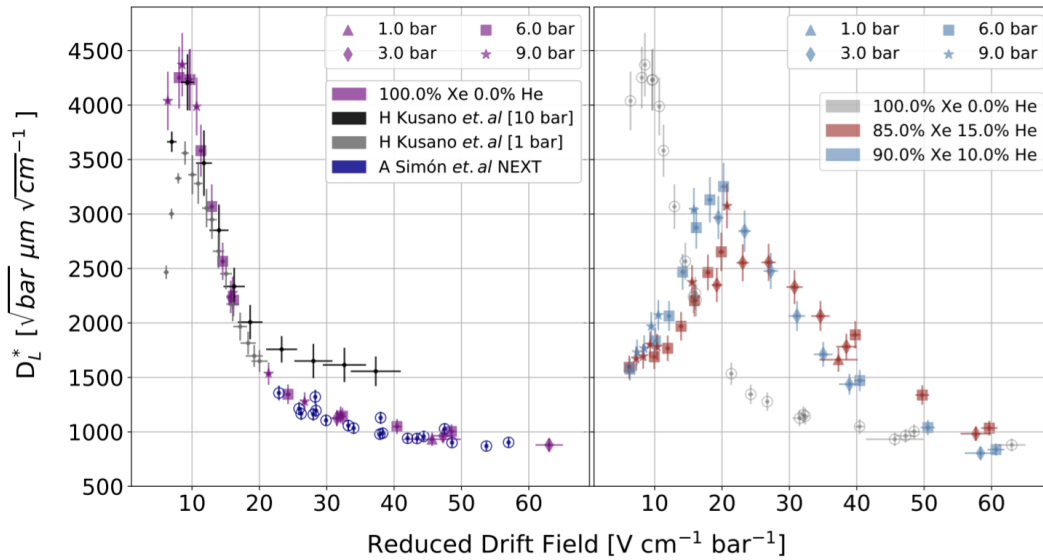


**Figure 9.** Comparison of  $D_L^*$  between pure xenon (left) and xenon-helium mixtures (right).

(b)

Figure 5.3: Longitudinal diffusion as function of the applied electric field for different concentrations of helium in xenon from [34] simulations (top) and the respective experimental results from [35] (bottom).

As apparent from figures 5.2 and 5.3, the predicted improvement in diffusion reduction is much larger for the transverse diffusion than for the longitudinal one. Yet, given the reduction in scale for the predicted  $D_T$  by electron cooling, as well as for the presented measurements of  $D_L$ , it is expected a  $\sim 2$  factor for spatial resolution improvements using xenon-helium gas mixtures [35].

### 5.1.2 Drift velocity

Not only is  $D_L$  and  $D_T$  changed by the addition of helium, but so is the drift velocity. The much faster electrons will naturally diffuse less, since the diffusion coefficient specifies the dependence of the diffusion process upon the time.

Simulation results from Magboltz for the drift velocity are presented in figure 5.4, where, for helium–xenon admixtures, it is predicted a drift velocity more than twice of that achieved in pure xenon [34].

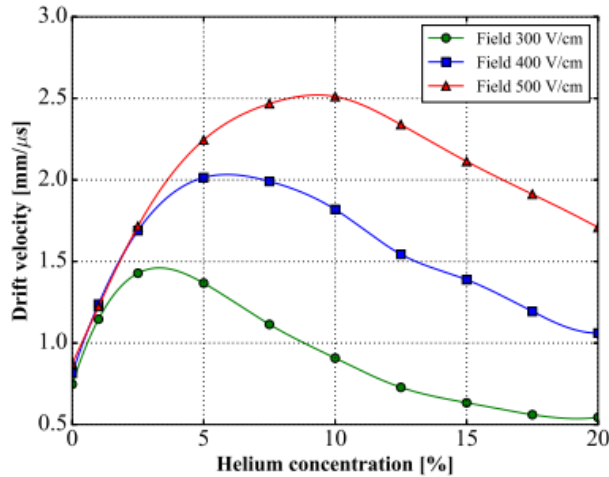


Figure 5.4: Drift velocity as function of helium concentration for xenon-helium mixtures for different electric fields [34].

Regarding the figure 5.4, for 15 % helium at 400 V/cm, a typical drift field used in NEXT-NEW, it is noted that the expected drift velocity is 1.7 times the one achieved in pure xenon at the same electric field [34].

The effect upon spatial resolution resulting from an electron-cooling additive can partially be caused by a change in the longitudinal diffusion. Nevertheless, further effects must be given consideration in terms of detector performance. Although this improvement on the drift velocity would have a minor positive impact in the data acquisition process, this will allow data buffers reduction, as well as the increase in electron lifetime at the same impurity concentrations [34].

### 5.1.3 Energy resolution

In former studies performed by simulation [34] it was reported that for xenon-helium mixtures below 20 % helium concentration, there is no perceptible effects on both the Fano factor and the  $w$ -value, since the number of ionisation electrons and the gas optical properties are not affected for this amount of helium added to xenon [34]. Since the energy resolution is firstly

affected by fluctuations in the electron-ion pairs production with the ionisation's variance being directly dependent on Fano and on the average number of produced electrons as well, the intrinsic resolution is stable for helium concentrations below that value and there are not expected any changes in the attained energy resolution for xenon-helium mixtures, with helium concentrations in the range of interest.

### 5.1.4 Primary scintillation

The scintillation properties of xenon-helium mixtures were studied in the past by [130], although only mixtures with a low xenon concentration have been studied. The scintillation properties were also analysed by [34] on its simulation studies where is referred that for the worst case scenario, as long as helium concentration does not overtake the 20 % value, the scintillation level will remain within 3 % of the respective value for pure xenon. Predicting so, the capability to detect the primary scintillation will not be affected for helium concentrations in the range of interest [34].

### 5.1.5 Electroluminescence yield

The energy resolution in proportional scintillation detection deteriorates for high electric fields applied to the scintillation region, for reduced electric fields above the gas ionisation threshold, when the electrons get enough energy to ionise the gas atoms and the statistical fluctuations in the number of electrons producing electroluminescence become dominant. Therefore, the regime of interest in terms of reduced electric field for pure xenon is in the range of 1.5-3.5 kV/cm/bar, identified in [120].

Since the first excited state of helium is 7.67 eV higher than the xenon's first ionisation level, it is expected for helium not to play a direct role in the secondary scintillation production of a xenon-helium EL TPC.

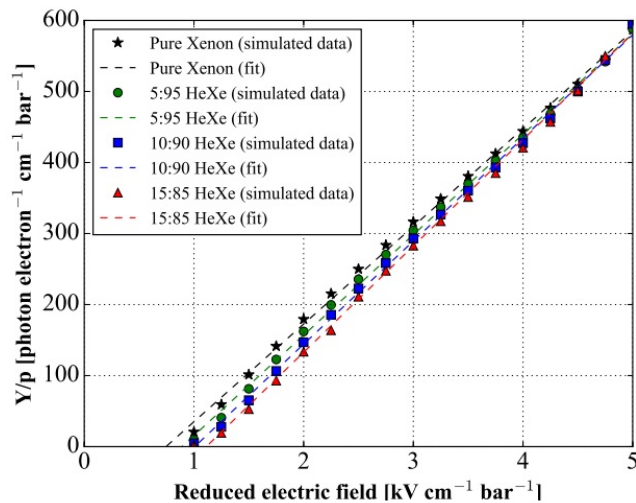


Figure 5.5: Results obtained from simulation for the reduced electroluminescence yield as function of the applied reduced electric field [34].

The idea that the EL yield for helium mixtures with xenon is not significantly affected with helium addition, relatively to EL yield obtained for pure xenon, was corroborated in the simulation results presented by [34], Fig. 5.5. The slight shift of EL threshold toward higher electric fields with helium addition is explained by helium's residual cooling effect. This shift can be overcome by increasing the voltage applied to the EL gap.

# Chapter 6

## Experimental setup and methodology

### 6.1 Experimental setup

The EL studies were performed in a small gas proportional scintillation counter, depicted schematically in fig. 6.1 which has a large area avalanche photodiode inside as VUV photosensor for EL readout.

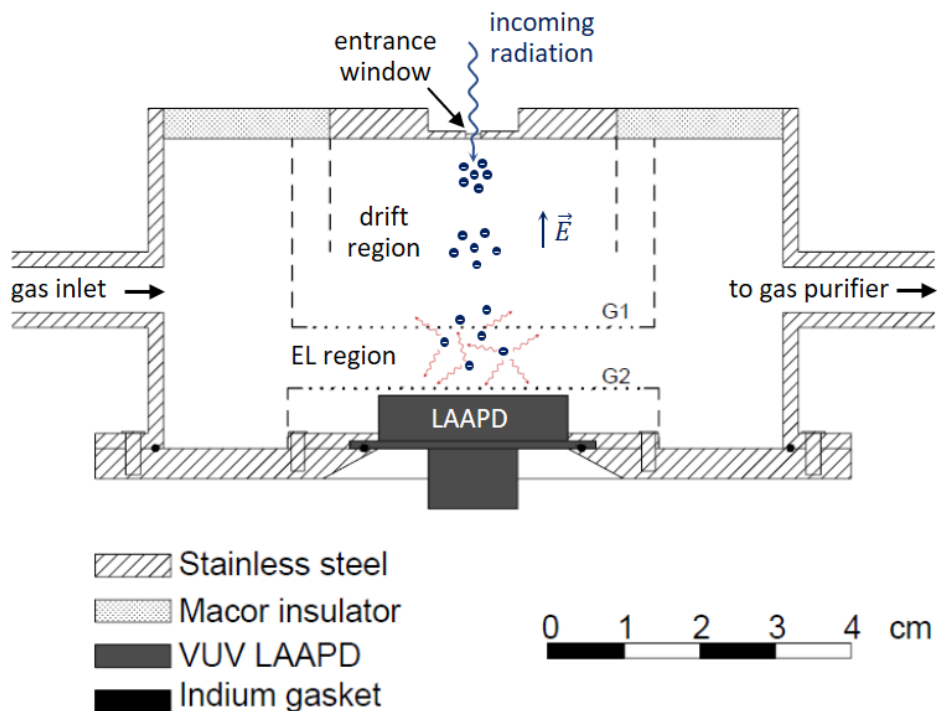


Figure 6.1: Schematic of a GPSC equipped with a large avalanche photodiode (LAAPD).

The LAAPD is a deep-UV enhanced series from Advanced Photonics Inc. [125]. This photosensor type was chosen because a PMT with a quartz window, sensible to scintillation in xenon, is permeable to helium. This GPSC

was already used for several studies using pure xenon and pure argon filling [126, 131].

The GPSC enclosure is a stainless-steel cylinder with a diameter of 10 cm and 5 cm in height. This is a standard uniform EL field type GPSC with an absorption (drift) region of 2.5 cm and a scintillation (EL) region 0.8 cm deep. It was filled at pressures around 1.2 bar, being the gas continuously purified through St707 SAES getters, that were kept at 150° C, and circulating by convection. The gas purifying system is a U-tubing connected to the GPSC, closing the gas inlet and outlet with a valve in each tip of the vertical arm enclosing the getters - a schematic diagram is presented in figure 6.2. The full system was rigorously vacuum tested for leaks.

The grids G1 and G2, which delimit the scintillation region, are made of stainless steel wire, with 80  $\mu\text{m}$  in diameter and a 900  $\mu\text{m}$  spacing, delimiting the scintillation region. The detector's radiation window is made of aluminized Melinex with a diameter of 2 mm and a thickness of 6  $\mu\text{m}$ . The holders of both radiation window and grid G1 are isolated with a Macor piece. A low vapour pressure epoxy was used to vacuum-seal the Macor piece, the radiation window and holder, as well as the voltage feedthrough of G1. On its turn, the LAAPD, placed just below G2, was vacuum-sealed with an indium ring compressed between the detector's stainless steel body and the photodiode enclosure.

Both the radiation window and its focusing electrode were operated at negative voltage, as well as the grid G1 and its respective holder. The LAAPD enclosure, its holder and mesh G2 were kept at ground potential. Thus, the electric field in the scintillation region is set by G1's voltage, whereas in the drift region the electric field is set by the voltage difference between the GPSC radiation window and the grid G1.

The LAAPD used in this setup is a windowless UV-enhanced and has an active diameter of 16 mm, from API. A maximum operation voltage of 1840 V was used, corresponding to a gain of approximately 150 and a dark current between 200-500 nA [125]. The LAAPD characteristics to xenon VUV EL detection is described in detail in [132].

In order to irradiate the GPSC along its axis, a 1 mm collimated 5.9 keV x-ray beam was used, emitted from a  $^{55}\text{Fe}$  radioactive source being the 6.4 keV Mn x-ray line ( $k_{\beta}$ ) efficiently absorbed by a chromium foil, 15  $\mu\text{m}$  thick. Thus, it will be easier to determine the energy resolution, since there is only a 5.9 keV full absorption peak in the region of interest. The signals extracted from LAAPD were fed through a low noise 1.0 V/pC charge sensitive pre-amplifier, Canberra 2006, which extracts the signal from the photosensor. These signals are conducted to a Hewlett Packard 5582A linear amplifier with

2  $\mu\text{s}$  shaping time constant, being pulse height analysed with a Nucleus PCA-II multi channel analyser (MCA) with 1024 channels, i.e., the MCA is used to construct a histogram of pulse heights, known as pulse-height distribution.

### 6.1.1 Gas mixture system

The gas mixture system was envisaged to accommodate two different volumes with well established volume ratios, both connected to the GPSC through vacuum valves, figure 6.2. Both volumes were used to store the intended amount of helium in order to be able to perform the studies of two consecutive xenon-helium mixtures with different helium content, following the detector characterisation with pure xenon, without any change in the GPSC operation conditions, namely the LAAPD bias, while the mixture is being made. The mixture was made simply by opening the respective valve of the given volume, connecting the helium storage volume to the GPSC volume.

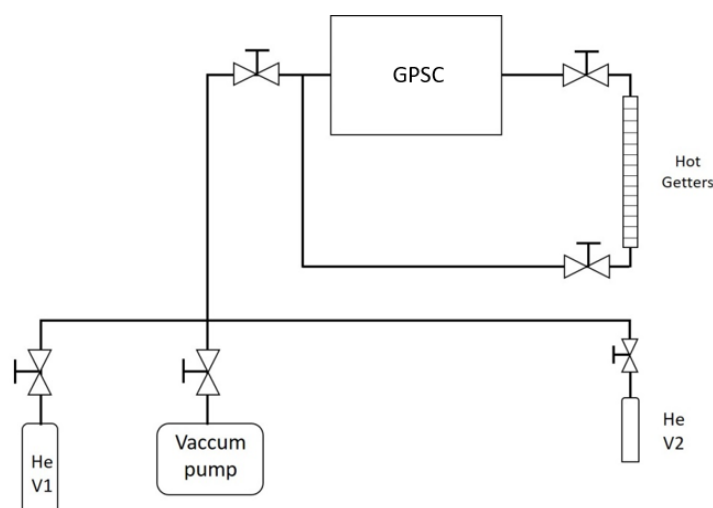


Figure 6.2: Experimental setup layout

The whole system was pumped down to a pressure of about  $2.0 \times 10^{-6}$  mbar for several hours. This is a standard procedure before adding any gas into the system. The proper amount of helium was stored in the volumes 1 and 2, both at well defined pressures, previously calculated, in order to achieve the desired xenon-helium concentrations. The xenon gas purity was 4.8 grade from Messer and helium was of grade 5.0.

## 6.2 Experimental methodology

### 6.2.1 Gas mixing procedure

After filling the two helium volumes, the GPSC and the tubings were filled with pure xenon. In each run, the data acquisition for the pure xenon and the two xenon-helium mixtures were performed 24 hours after the xenon was being circulating in the getters, allowing the system temperature to stabilise and the xenon to purify.

The LAAPD was previously polarised before each series of data taking set and was left to stabilise for a few hours, until its dark current and, therefore, its gain were stabilised around a given value. During the helium mixing process, in order to obtain a given xenon-helium mixture concentration, the LAAPD leak current and the GPSC response to the 5.9 keV x-rays was continuously monitored, i.e. the centroid and energy resolution of the total absorption peak were monitored while the LAAPD bias and the detector applied voltages were kept constant, without being turned off. This allowed us to know when the gas mixing process was concluded and the system stability was again reached. For the monitoring purpose, during the gas mixing process, values of 0.45 kV/cm/bar and 3 kV/cm/bar, were chosen for the drift and scintillation reduced electric fields, respectively, in the GPSC while a biasing voltage of 1840 V was applied to the LAAPD.

Therefore, in a single run, the GPSC EL output and the energy resolution dependence on the reduced electric field in the scintillation region were studied for pure xenon and for two different helium concentrations without the need to switch off the GPSC and LAAPD bias voltages. This method was adopted in order to minimise the influence of external factors and so avoid changes in the operation conditions. This procedure was repeated several times, being the helium concentration values chosen arbitrarily, in order to verify the results coherence and repeatability, as well as to validate them and evaluate any possible fluctuations in the data.

It is worth to mention the fact that all admixtures end up with a specific total pressure inside the detector, which is different from mixture to mixture due to the fact that the admixtures were performed by adding a specific helium volume to the total volume. Nevertheless, the initial helium pressures inside the two volumes were set taking also into account this issue and it was possible to keep all the studied pure xenon and xenon-helium gas mixture fillings within a 18 % variation, around an average pressure of 1.14 bar. A relative uncertainty below 4 % in the helium concentration results occurred from both the pressure gauge precision and the uncertainty in the volumes ratio.

## 6.2.2 Data taking and analysis methodology

Along each run, the gain and the APD stability were monitored, repeating the measurement for the same E/p in the drift and scintillation regions, for several times during the run. Any slight change in the dark current was registered for compensating its effect. During the studies, the room temperature was monitored and recorded as well, remaining less than  $\sim 2^\circ\text{C}$  around a medium value of  $23^\circ\text{C}$ .

A typical response of the GPSC to 5.9 keV is presented in Fig 6.3.

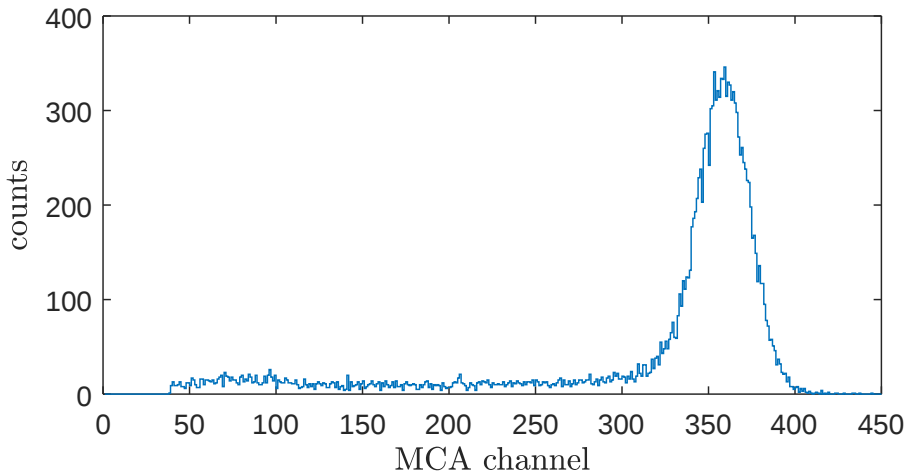


Figure 6.3: Pulse-height distribution for 5.9 keV x-rays absorbed in the GPSC active volume filled with Xe-15%He, for a reduced electric field of 2.4 kV/cm/bar.

When x-rays with energy  $E_x$  are fully absorbed in xenon by photoelectric effect, they will produce a primary electron cloud of  $N_e$  primary electrons, where  $N_e = E_x/w$  and  $w \approx 22$  eV/ion pair is the average energy needed to create an electron/ion pair in xenon [126]. The cloud of primary electrons will drift towards the scintillation region, under the influence of a weak electric field  $E/p \sim 0.45$  kV/cm/bar, kept below the gas excitation threshold promoted by electron impact in xenon. In the scintillation region, the electrons are accelerated by means of an intense electric field, chosen above the scintillation threshold but still below the electron impact ionisation threshold in xenon and each electron will gain enough kinetic energy to excite the gas atoms upon impact, resulting in VUV photon emission in consequence of the deexcitation processes.

Following the incidence of VUV photons in the LAAPD, free electrons are produced, which are driven towards the anode electrode and charge multiplication occurs in the intense electric field around the P-N junction, resulting in a sizeable charge signal in the LAAPD anode. All these processes are bound to be proportional, being the LAAPD output signal proportional to

the initial number of primary electrons and, thus, to the energy deposited in xenon by radiation interaction.

The number of scintillation photons per primary electron is large [126] (for the  $E/p$  range used in the present studies) and the statistical fluctuations related with light amplification process is negligibly small, when compared to that associated with the primary electron cloud formation. As a result, the energy resolution of a GPSC approaches the theoretical limit determined by the Fano factor and  $w$ -value in xenon, provided a low noise high-sensitivity photosensor to measure the VUV scintillation light.

The primary scintillation produced by x-ray interaction is more than 3 orders of magnitude lower than the EL output [14], therefore being within the electronic noise.

In order to measure both amplitude and energy resolution of the produced signals, the full absorption peaks were fitted to Gaussian functions, overlapping to a linear background, and then both FWHM and centroid were determined, being the centroid taken as pulse amplitude. The full absorption peak's position (centroid) and its relative FWHM were studied for pure xenon and for each xenon-helium mixture studied in this work, as a function of the reduced electric field in the scintillation region.

Since the main objective of the present work was to study the variation of the EL yield and GPSC energy resolution of xenon-helium mixtures relative to pure xenon, the EL yield was measured only with relative values. Each run, the reduced EL yield absolute values,  $Y/p$ , were determined by normalising the pulse amplitude measured for pure xenon at  $E/p$  of  $\sim 2.0$  kV/cm/bar to the respective absolute value obtained in simulation data [34]. The calculated normalisation constant was then used to normalise the remaining centroid values obtained for the different  $E/p$  for pure xenon and for the xenon-helium mixtures studied in the same run. This methodology, by performing in each run the study of EL yield for pure xenon allows to obtain absolute values for the EL yield of the different xenon runs, independently of the LAAPD operating conditions, e.g. temperature, dark current and gain, and therefore obtain results that are comparable to each other.

Despite the operating conditions have kept stabilised along each run, slight changes in the LAAPD dark current could happen, since each run took some hours of duration. In order to correct for the possible slight changes in gain due to the variations in the leak current in LAAPD, independent studies have been made in order to determine how the leak current changes affects the LAAPD gain. This was made by fine tuning the LAAPD bias voltage in order to obtain the observed changes in the LAAPD dark current, measuring the respective pulse amplitude variations, i.e. the variations in the 5.9 keV peak centroid

position.

In addition, before each data taking set, some measurements were taken for the same applied reduced electric field, while the leak current wasn't still stabilised. These measurements allowed us to have more data in order to understand how the gain would change in function of the leak current. Plotting the centroid channel data as function of the leak current, it was clear that there was a linear dependence of the centroid channel variation with the leak current, decreasing the gain with increasing leak current. For each  $nA$  variation in the leak current there was a 0.32 % variation in the gain value. There were no observed modifications to this behaviour along the whole data taken campaign. These applied corrections were correspondent at the level of less than 5 % of the respective value. Thus, it is a certainty that all data is correspondent to exactly the same operation conditions and comparable to each other.

### 6.2.3 Waveform analysis methodology

In the reported work the standard method was used, with the photosensor output connected to a pre-amplifier, followed by a linear amplifier and a Multi-Channel Analyser for pulse-height analysis. This setup doesn't allow the preservation of the photosensor signal temporal information (for instance the drift time information), which is crucial to understand the underlying dynamics related with the drift electrons as well as the scintillation production, like the drift velocity.

For that, we used a digital oscilloscope, WaveRunner 610Zi from Lecroy with 50  $\Omega$  DC coupling (used to match the cable impedance in order to avoid wave reflections). In this way, it becomes possible to access the signal amplitude as a function of the time. With the LAAPD low gain, the recorded waveforms, taken directly on its output, have a high noise level, making difficult to trigger the events in the oscilloscope. The solution that was used in order to overcome this problem was to connect the LAAPD to a pre-amplifier and then to a linear amplifier with a 50 ns shaping time, instead the 2  $\mu s$  used as shaping constant for the EL yield measurements. In its turn, the amplifier is connected to the oscilloscope. In this way, the output signal coming from the linear amplifier is similar to the waveforms at the LAAPD output, with just an additional distortion in the order of 50 ns.

The oscilloscope trigger was set on the rising edge with a threshold slightly higher than the baseline electronic noise, being the data recorded in the oscilloscope memory. In order to achieve good statistics, the maximum memory is used for each performed run, corresponding to  $10^5$  files, each one with a single waveform and the size of data is needed to be firstly reduced for

performance proposes. Accordingly, it was performed a reduction in memory size of 20 times, by averaging every 20 successive sampled points, reducing in this way the high frequency noise, even though degrading the time resolution of waveforms from 0.1 ns to 2 ns, still enough for the following analysis.

A typical waveform obtained with 5.9 keV x-rays is shown in the figure 6.4.

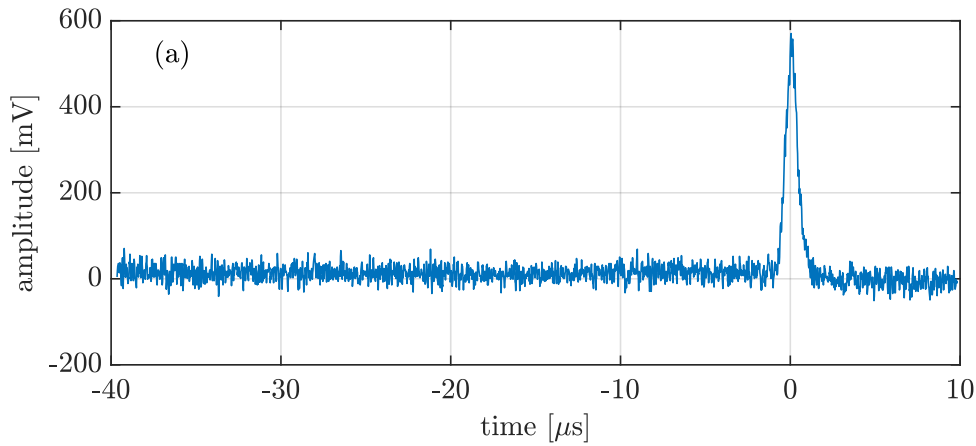


Figure 6.4: Typical waveform obtained with 5.9 keV x-rays.

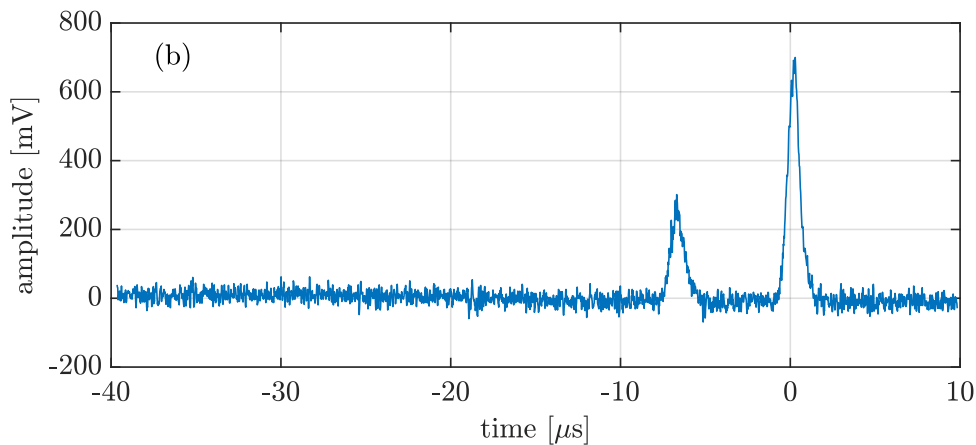


Figure 6.5: Example of a rejected waveform that significantly deviates in time from the trigger instant.

The waveforms that were not correctly sampled or correspond to background events were rejected through the use of an algorithm. This algorithm rejects all waveforms with sharp negative spikes and saturated signals, since they are mainly produced by high frequency interferences and high energy cosmic rays, respectively. Waveforms whose secondary scintillation signal is too short (e.g. single photon pulses) or too long, with a time  $> 5 \mu\text{s}$  (e.g., double event waveforms) are also rejected, being this duration measured between the 50%-rising edge and the 50%-falling edge with respect to the pulse height. Figure 6.5 illustrates one example of a rejected waveform due to its excessive secondary scintillation pulse duration.

This rejection method is decisive when detailed information about the waveform shape is required.

A second algorithm was used to align all recorded waveforms in time, based on the secondary scintillation 50%-rising edge with respect to the pulse height, corresponding approximately to the time when the electron cloud centroid reaches G1. This procedure is required to reduce the jitter introduced by the fixed threshold oscilloscope trigger.



# Chapter 7

## Experimental results: validation of the experimental methodology and obtained results

A detector with a gas mixture volume whose xenon amount is much higher than the helium amount will have scintillation features extremely close to those verified in a detector filled with only pure xenon, with just a small variation in the scintillation distribution (the energy spectrum), scintillation yield and in the detector energy resolution [34].

### 7.1 GPSC performance with pure xenon filling

Firstly, the GPSC performance was tested using pure xenon gas filling with a 5.9 keV x-rays source.

Our first results have shown that, given the experimental conditions of our setup, it was not possible to operate the GPSC at the same operational conditions, namely at the same LAAPD dark current and, therefore at the same LAAPD gain. Each time the LAAPD bias voltage was turned on, at a given day, in order to begin the GPSC performance studies, the LAAPD dark current stabilised in a different value.

This fact resulted in different GPSC gains, as shown in Fig. 7.1 where the centroid for the 5.9 keV peak, normalised by the gas pressure, is presented as a function of reduced electric field in the scintillation region. The different data sets refer to different days of data acquisition and slight different filling pressures, while using the same reduced electric field in the drift region, the same LAAPD bias voltage and the same electronic chain gain and pulse formatting. This was a major problem to overcome for the planned studies.

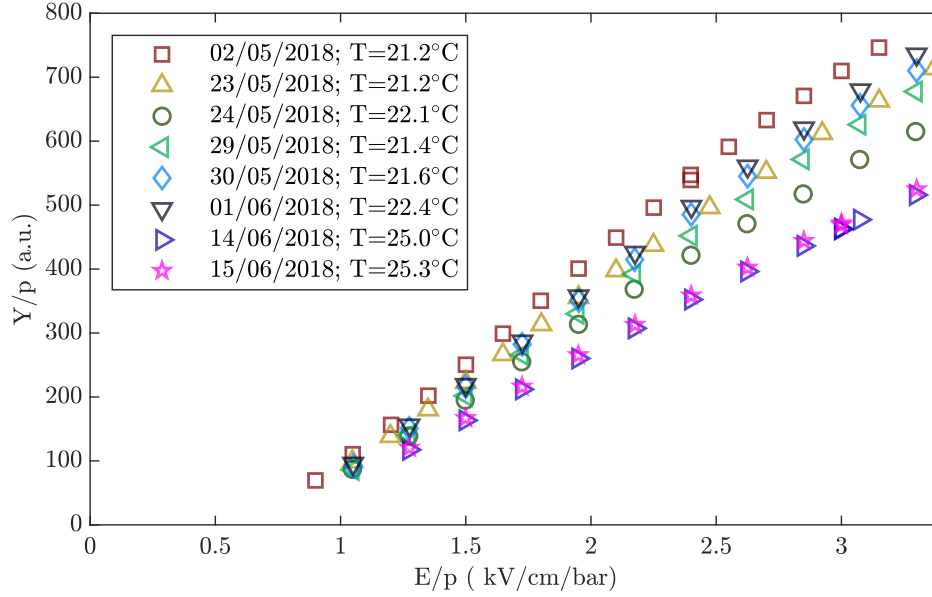


Figure 7.1: EL yield ( $Y/p$ ) in arbitrary units for pure xenon, normalised by pressure, as a function of reduced electric field ( $E/p$ ) applied to the scintillation region achieved for several runs with different LAAPD operation conditions.

However, since there should be a proportional relation between the centroid and the EL yield, one should be able to obtain the same values from different curves, upon normalising each curve to an absolute EL yield value (e.g. that obtained by simulations) at a given reduced electric field in the scintillation region. The different curves should, then, superimpose to the absolute EL yield curve and, thus, to each other.

Indeed, absolute values of reduced EL yield,  $Y/p$ , were obtained for each run, by normalising the pulse amplitude measured at an  $E/p$  of  $\sim 2.0$  kV/cm/bar to the corresponding absolute value obtained from simulation [34]. In each data set, the same normalisation constant has been used, then, to normalise the remaining centroid values obtained for different  $E/p$  values.

In fact, we proved that these were so and, therefore, reliable results that could be obtained with our setup. The consistency of experimental procedure performed in this work is demonstrated in figure 7.2 where the reduced EL yield ( $Y/p$ ) is depicted as a function of reduced electric field ( $E/p$ ) applied to the scintillation region for several runs performed with pure xenon in different days and at different pressures, after performing the normalisation, referred to above, in each individual data set. The average pressure is 1.12 bar and there is a variation of at most 13 % in pressure for the several performed runs.

A good reproducibility of the normalised experimental results is observed. From the data in Figure 7.2, we determined the values for the amplification parameter for EL, the slopes of the linear fits, obtaining an average value of  $136 \pm 1$  photons/kV. This value is in good agreement with those obtained

by simulation or by experimental measurements, e.g. [30, 32, 113, 133, 134]. The average scintillation threshold for EL, the linear fit interception with the horizontal axis, is  $0.69 \pm 0.04$  kV/cm/bar. This value is also in good agreement with both simulation studies and experimental values presented in literature [18, 20, 31, 120]].

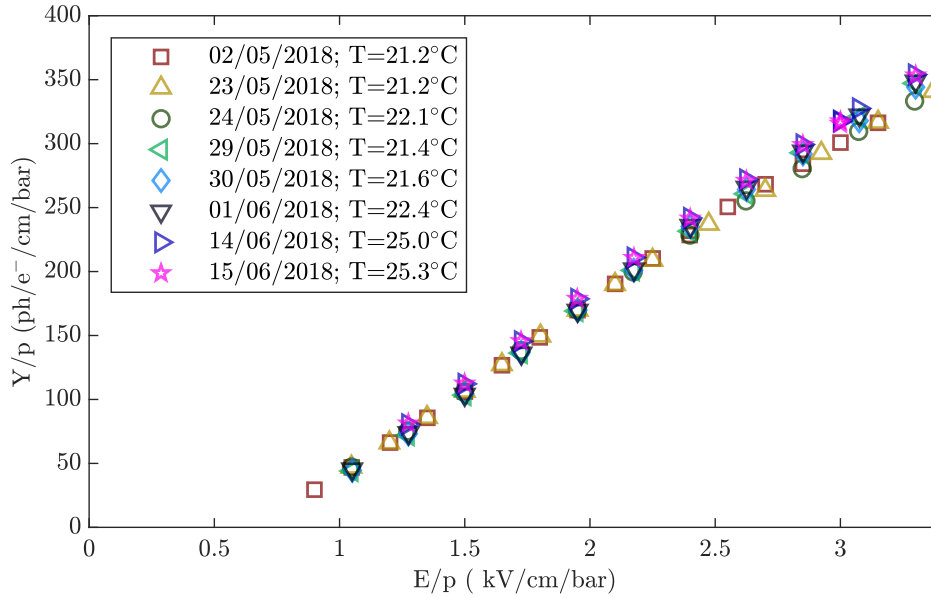


Figure 7.2: EL yield ( $Y/p$ ) as a function of reduced electric field ( $E/p$ ) applied to the scintillation region obtained with pure Xe in different days at different room temperatures. Absolute values were obtained from the normalisation procedure described in the text above.

In this way, we demonstrated that our experimental setup delivers stable and reliable results, despite the LAAPD gain fluctuations.

Although the LAAPD leak current fluctuations are larger along different days, the LAAPD gain correspondent variations are still significant between the data acquisitions performed on the same day with pure xenon and two xenon-helium mixtures. For this reason, these gain differences need to be corrected based on the leak current fluctuations, as previously described in section 6.2.2.

In order to demonstrate the reliability of this method, four runs of pure xenon were chosen, from different days and having different leak currents, as shown in Fig. 7.3a. There is an apparent correlation between the LAAPD leak current and the room temperature.

The first run corresponding to the black line was normalised to the simulation reduced EL yield from [34] for a reduced electric field of 2 kV/cm/bar and the same normalisation constant was used for all other centroid values, including data points of the remaining three runs. Then, the LAAPD gain was corrected for each run, taking into account the difference

between the respective leak current and the one for the reference line, in black.

The result of this procedure is shown in figure 7.3b, where the corrected data superimpose with that of the reference curve, only with a maximum deviation of 10 %. All the electroluminescence yield values obtained with xenon-helium mixtures in the present work were corrected in this way, having the pure xenon run performed a few hours earlier, as reference.

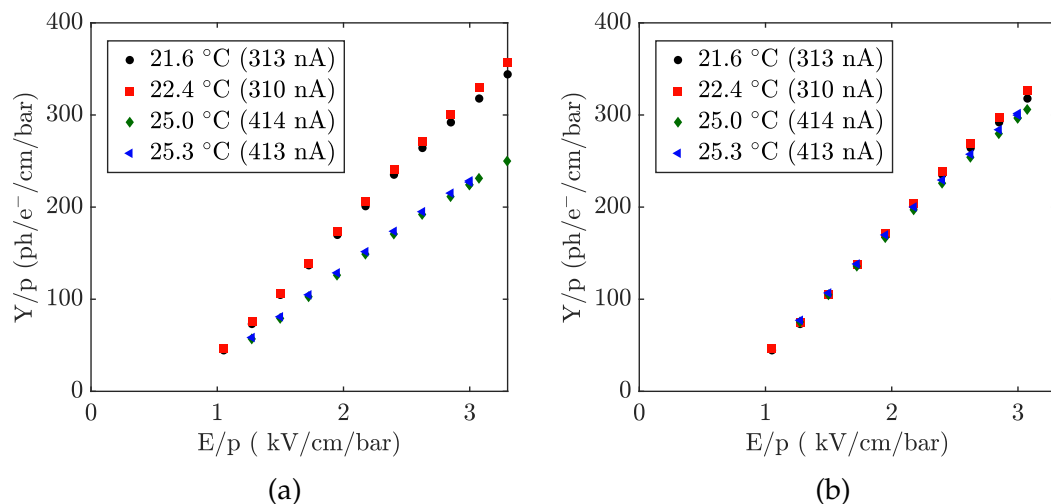


Figure 7.3: Reduced EL yield ( $Y/p$ ) for pure xenon as a function of reduced electric field ( $E/p$ ) applied to the scintillation region obtained from different days (with different room temperatures and leak currents). a) Data without leak current correction. b) The same curves with data corrected for leak current.

In this way, the present methodology used for correction of the LAAPD gain fluctuations, as well as for obtaining absolute EL yield values is successfully validated, being notable the experimental results reproducibility.

## 7.2 Intrinsic energy resolution

The energy resolution achieved with this GPSC for pure xenon must be compared with the results presented in the literature, already well established for xenon, so that both methodology and the detector's performance here developed can then be validated. This is important because if there was any problem with the gas purification or yet the detector's design was not suitable for the present studies, its performance wouldn't be at the best.

The study is performed with a single 5.9 keV x-ray line, whose energy spectrum was depicted in figure 6.3, presented in the previous chapter. As aforementioned, the full absorption peak has a Gaussian-like shape and the energy resolution for the detector in use is estimated from the relative FWHM

of the Gaussian function fitted to the full absorption peak.

The x-ray beam divergence is minimised using a narrow x-ray collimator (7 mm thick, with 2 mm in diameter), which was placed 2 mm way from the detector window, whereas the remaining geometrical effects can be neglected in a compact detector like this.

The electron loss for the detector window or to the gas impurities is minimal, and the gas purity is efficiently maintained by circulating through hot getters.

The energy resolution of our GPSC is depicted in Fig. 7.4 as a function of reduced electric field in the scintillation region, for different runs. A good energy resolution, around 8.56 %, was obtained at high E/p values, evidencing the good performance of our detector and the good gas purity level that could be achieved in it.

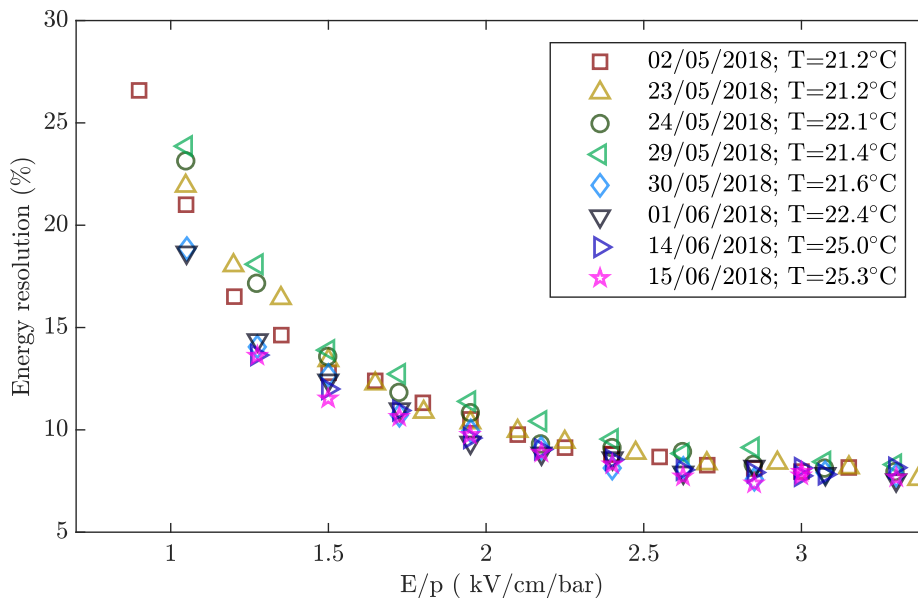


Figure 7.4: Energy resolution as a function of E/p, obtained for pure xenon.

In pure xenon, the relative fluctuations on EL photon production are low, when compared to fluctuations on primary charge production [120], which is, in fact, the main contribution for the above energy resolution at high E/p values. The detector energy resolution ( $R_E$ ) can be described by equation 4.11 described in subsection 4.3, assuming that no additional fluctuations are contributing to the energy resolution and/or are negligible when compared to the photosensor and primary charge production contributions.

The intrinsic energy resolution is defined as the relative statistical fluctuations in the number of the primary electrons produced upon x-ray interactions. In accordance with equation 4.14, a plot of the square of the energy resolution as a function of the reciprocal amplitude for variable reduced electric fields in the scintillation region will present a linear trend,

since the average number of VUV photons produced in the scintillation region,  $N_{EL}$ , is proportional to the peak centroid,  $A$ . The GPSC intrinsic energy resolution can be obtained by extrapolating the linear trend to infinite light yield, i.e.  $1/A \rightarrow \infty$ .

Typical plots of  $R_E^2$ , as a function of the peak centroid inverse,  $1/A$  are depicted in figure 7.5, together with a linear fit to data points in the linear region.

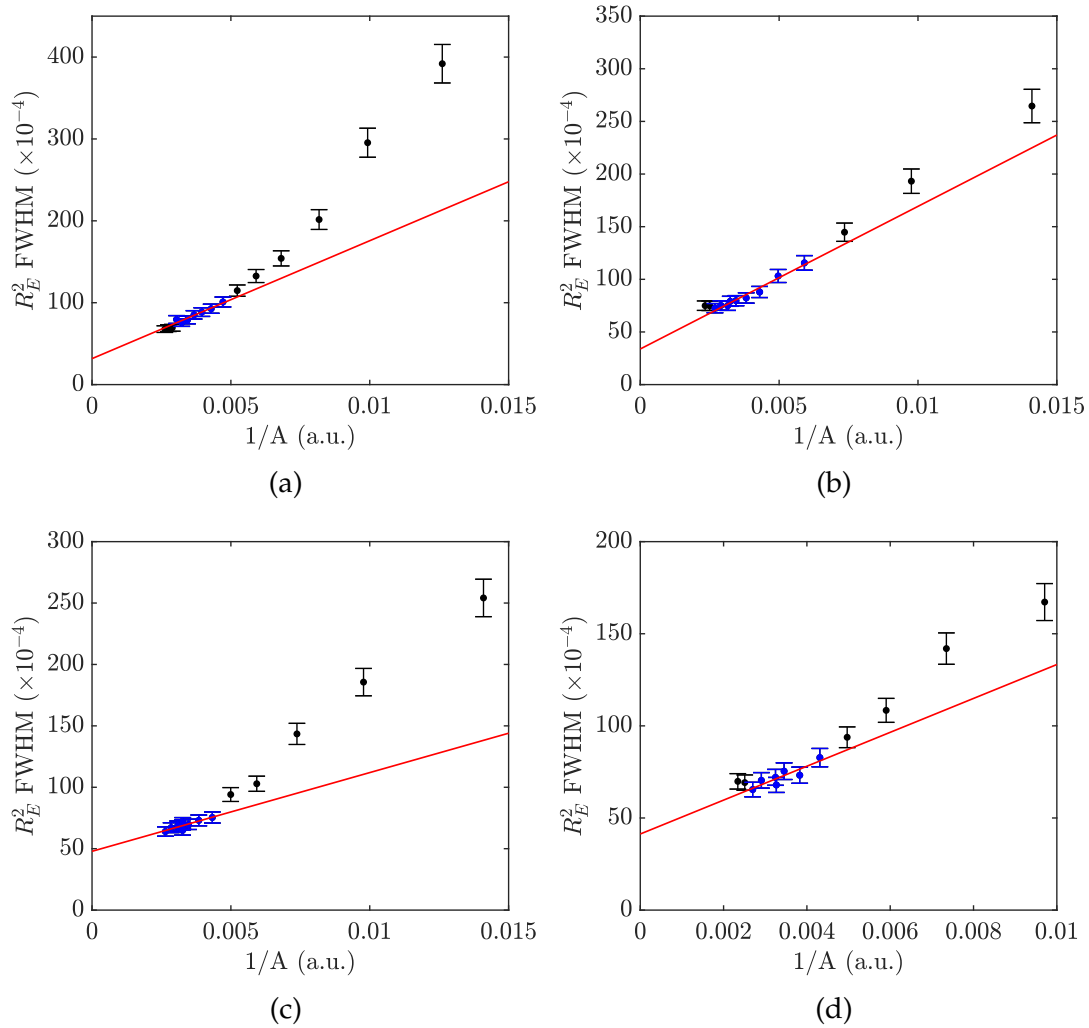


Figure 7.5:  $R_E^2$  as a function of  $1/A$ , obtained with pure xenon, for runs performed in different days. The solid line represents the linear fit to the data points in blue, with the remaining points excluded from the fit.

As shown in Fig. 7.5, the energy resolution degrades faster than that foreseen by the linear regression in the region of low reduced electric field intensities. This is due to fluctuations in electronic noise, whose contribution becomes significant as the signal to noise ratio degrades, and due to the loss of primary electrons to mesh G1. The electron transmission through G1 becomes less than unity for low values of scintillation-to-drift electric field ratio [135]. Eventually, in the region of high reduced electric field intensities,

the energy resolution also degrades, departing from the linear trend, due to additional fluctuations introduced by electron multiplication, above the gas ionisation threshold, and/or by the onset of micro-discharges due to insufficient electric insulation. A similar deviation from this linearity can be also observed in other GPSC studies [133].

The error in  $1/A$  is not represented due to the low statistical uncertainty in the Gaussian centroid, whereas the error in  $R_E^2$  corresponds to 6 %.

Thus, after performing several data-sets, the average intrinsic energy resolution estimated from the y-interception of the fitted lines, is  $(6.0 \pm 0.2)$  %. The error was estimated by considering two contributions: The first is related with the uncertainty in the choice of the most suitable fit interval and was estimated by varying slightly the linear fit region taking into account several data points, the other contribution is related with the statistical error associated with the fit parameters.

The Fano factor (F) is defined as the relative variance on the number of electrons produced during interaction, thus:  $F = \sigma_e^2 / \bar{N}_e$  and is a characteristic of the gas. As aforementioned, the Fano factor can be estimated from the intrinsic energy resolution, according to eq. 4.13.

For the used 5.9 keV x-rays, the average number of electrons in xenon per x-ray interaction with the gas,  $\bar{N}_e$  is 269 electrons, assuming an average energy  $w$  of 21.9 eV required in order to produce an ion-electron pair [114]. Therefore, using the equation 4.13, the calculated Fano factor was  $0.18 \pm 0.04$ . This Fano factor agrees with other results found in literature [30, 113, 114], showing the robustness of the analysis performed.

There is still additional systematic errors affecting the energy resolution which also may depend on the electric field variation, since it does not only affects the number of photons detected by the photosensor. Another factors may also affect the energy resolution, such as the electron loss to G1 mesh; electron attachment induced by impurities, which depends on the electron mean energy and on the number of collisions; the recombination of primary charges; geometrical effects that may depend on electron velocity and electron diffusion; the power supply stability or sparks occurring at high bias voltages. These field-dependent effects may also modify the linear trend slope, but they are expected to be negligible or have a small impact in the energy resolution for the reduced electric field region of interest.



# Chapter 8

## Experimental results: Xe-He mixtures

Understanding the impact of helium on xenon scintillation is the main motivation for the present work. Therefore, the experimental results obtained for electroluminescence yield and for detector's energy resolution are summarised in this chapter, being these two the most relevant parameters for the NEXT experiment.

### 8.1 Electroluminescence yield

Several mixtures were performed for each helium concentration to be studied in the present work, namely, three for 15 % helium, two for 20 % helium, and one either for 10 % as for 30 %. However, for this latter it were taken two measuring series with seven days apart from each other.

The detector response function, consisting in a Gaussian function summed to a linear function, is fitted to the 5.9 keV full absorption peak of MCA pulse height distribution. The relative  $Y/p$  is obtained from the Gaussian centroid divided by the working pressure for the several  $E/p$  values. The  $Y/p$  variation with  $E/p$  obtained for each run is then fitted by a straight line, since  $Y/p$  as a function of  $E/p$  is known to be approximately linear [18]. This fitting line is used to extrapolate the relative  $Y/p$  at a specific  $E/p$  value of 2 kV/cm/bar. The absolute pure xenon  $Y/p$  at the same  $E/p$  value from simulation in ref [34] is used to compute the normalisation constant, which is applied to all experimental relative  $Y/p$  values taken in the same run, as well as in the mixture runs performed on the same day. In addition,  $Y/p$  values obtained with xenon-helium mixtures were corrected for the LAAPD leak current, having as reference the pure xenon  $Y/p$  values obtained on the same day.

Figure 8.1 presents experimental EL yields obtained for all xenon-helium admixtures and pure xenon as function of the reduced electric field applied to the scintillation region.

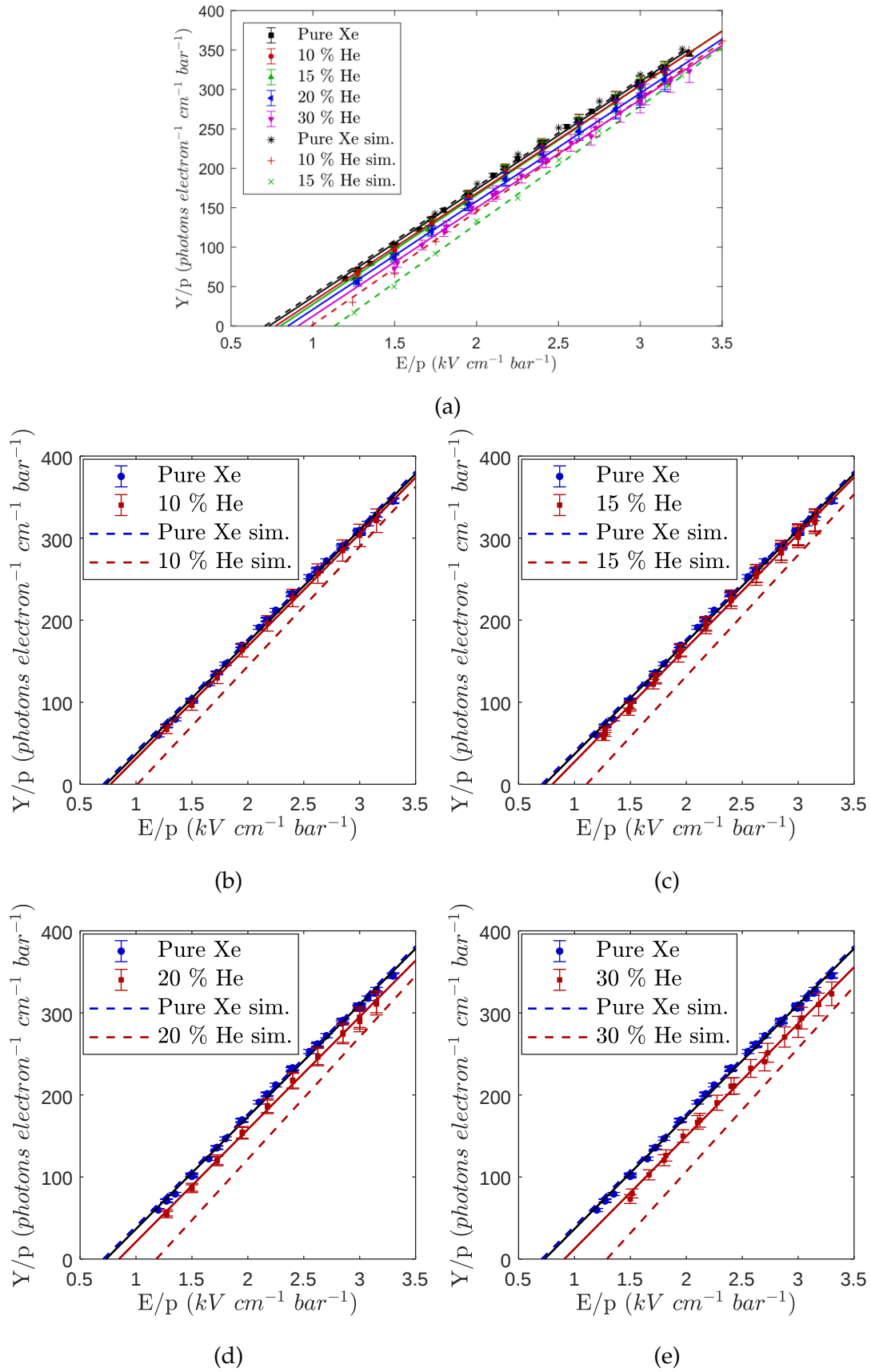


Figure 8.1: Reduced EL yield as function of  $E/p$  in the scintillation region for pure Xe and for the different Xe-He mixtures studied in the present work. The solid and dashed lines correspond to linear fits performed on the experimental and simulation data from [34], respectively. The full data set is depicted on the top plot. The different He concentrations are separated in the 4 bottom plots for readability purposes.

For each helium admixture and for pure xenon, a single linear function was fitted to the whole data set (i.e. joining together data from different days), showing the respective average linear trend. The error bars represent the data points uncertainties, being dominated by the systematic error estimated for the LAAPD leak current correction. For comparison purposes, the results obtained by simulation in [34] are also depicted - dashed lines. The simulated trend predicted for pure xenon is the same one used to compute the normalisation constant, allowing for a more intuitive comparison of experimental data with simulation.

Table 8.1 lists the experimental EL amplification parameter, i.e. the slope of the linear dependence of  $Y/p$  with  $E/p$ , and the scintillation threshold obtained from the linear fits shown in figure 8.1 .

Table 8.1: Electroluminescence amplification parameter and scintillation threshold obtained from the linear fits performed to experimental data for different helium concentrations.

He concentration	EL threshold	Amplification parameter
0 %	$0.73 \pm 0.01$	$137 \pm 1$
10 %	$0.77 \pm 0.03$	$137 \pm 2$
15 %	$0.80 \pm 0.02$	$139 \pm 1$
20 %	$0.85 \pm 0.02$	$137 \pm 1$
30 %	$0.91 \pm 0.03$	$137 \pm 2$

The EL yield as a function of helium concentration is shown in figure 8.2 for a reduced electric field of 2.5 kV/cm/bar in the EL region, as obtained from the linear fits parameters of table 8.1. For comparison reasons, the simulation results were included as well.

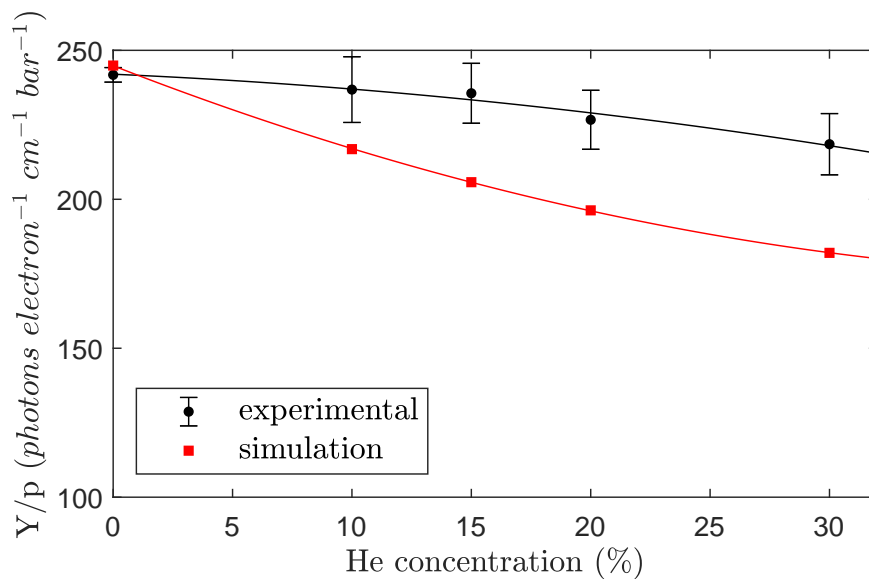


Figure 8.2: Experimental and simulated reduced EL yield as a function of He concentration for an  $E/p$  of 2.5 kV/cm/bar. Solid curves (2-degree polynomial fit) serve only to guide the eye.

From figures 8.1 and 8.2, one may observe that EL production decreases with the helium concentration, as expected. Nevertheless, the results obtained for each mixture are fairly identical within the E/p region of interest of NEXT, 1.5-3.5 kV/cm/bar, being the EL yield always under the one obtained for pure xenon.

Due to the lower mean kinetic energy of electrons promoted by collisions with helium atoms, the EL threshold increases with the helium concentration. However, this effect was found to be significantly smaller in our experimental data, when compared with simulations, as observed in figure 8.1.

For all helium concentrations and E/p values studied in this work, the impact of helium on the xenon electroluminescence yield was found to be lower than the impact predicted by simulations. For instance, whereas the simulation results foresee a drop of  $\sim 16\%$  in the EL yield for 15 % helium concentration at an E/p  $\sim 2.5$  kV/cm/bar, compared with the yield of pure xenon, for the experimental measurements this drop assumes a value of only  $\sim 3\%$ . A possible contribution for this difference to arise might be due to neutral bremsstrahlung, i.e. the bremsstrahlung emitted by electrons, scattered on neutral atoms, while drifting in the EL region [85]. This type of radiation might be extended from VUV to NIR [85], a region where the APD is also sensitive. This issue is something to be addressed in future studies.

## 8.2 Energy resolution

The GPSC energy resolution (FWHM) computed from the pulse height distribution obtained for several reduced electric fields in the scintillation region, is depicted in figure 8.3 for each mixture studied in the present work. Despite not being shown in this plot, an uncertainty of 3 % was estimated for the energy resolution values.

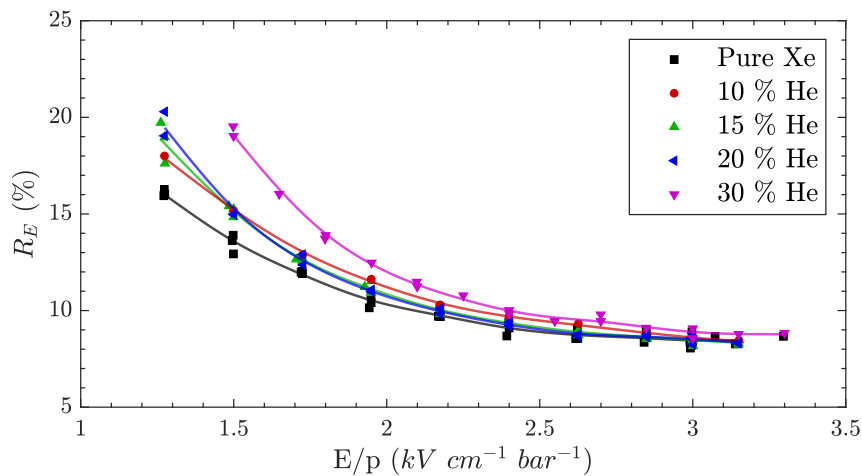


Figure 8.3: Energy resolution as function of the reduced electric field in the scintillation region, obtained for pure Xe and several Xe-He mixtures. Solid curves serve only to guide the eye.

Due to the experimental methodology used to prepare xenon-helium mixtures, the data acquisition with pure xenon was always performed at a higher pressure than the two xenon-helium mixtures studied in the respective same day. The distance travelled by electrons between collisions is shorter, as higher is the total pressure, resulting in more xenon atom excitations for the same  $E/p$  value and, consequently, the more scintillation photons are being produced. Therefore, different gas pressures will lead to different energy resolution values, since the relative fluctuations on the photosensor signal decrease with the number of collected photons (as demonstrated by equation 4.11). For this reason, the helium impact on the detector energy resolution cannot be directly evaluated from figure 8.3, since the operation pressures were considerably different, in some cases more than 25%.

According to equation 4.10 the GPSC energy resolution depends mainly on fluctuations in the primary charge production and in the LAAPD signal as well. The LAAPD contribution ( $R_{ph}$ ) to the overall energy resolution is directly proportional to the inverse of the square root number of produced photons ( $R_{ph} \propto 1/\sqrt{N_{EL}}$ ), with  $N_{EL}$  being linearly dependent on the gas pressure, as previously explained. Therefore, knowing the contribution of fluctuations in primary charge production (as obtained in section 7.2), and assuming that this does not depend on the gas pressure or mixture concentration, the energy resolution values of figure 8.3 can be corrected for the pressure differences, by scaling the LAAPD contribution with the pressure (the corrected  $R_{ph}$  being equal to  $R_{ph} \frac{\sqrt{P_{ref}}}{\sqrt{P}}$ ).

Figure 8.4 depicts the energy resolution corrected by the total gas pressure as a function of the reduced electric field, being assumed a reference pressure ( $P_{ref}$ ) of 1.14 bar, which corresponds to the average pressure over the full set of acquisitions.

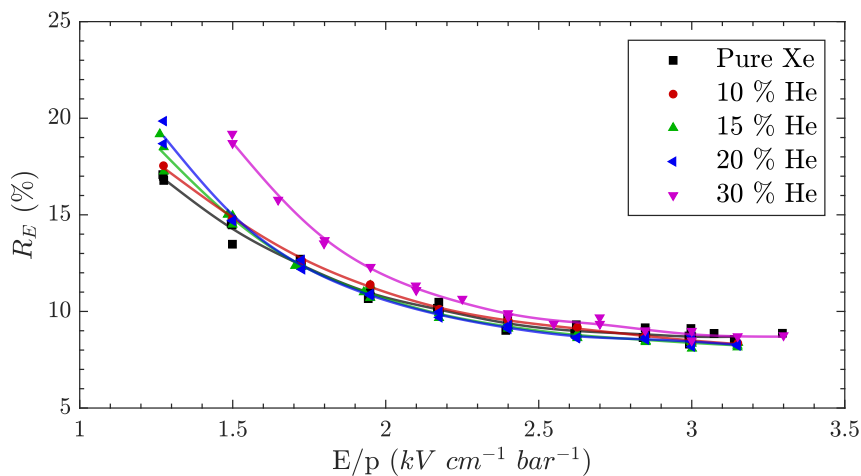


Figure 8.4: Energy resolution as function of  $E/p$  in the scintillation region, obtained for pure Xe and for the several Xe-He mixtures, with the values of each run corrected for the total pressure.

Taking into account that the Fano factor is not expected to change within the range of the studied concentrations, as foreseen in the simulation studies from [34], the noticed difference in the corrected data from figure 8.4 is only due to the lower number of produced scintillation photons as higher is the helium concentration. The energy resolution is only deteriorated for low electric fields, where the LAAPD contribution is dominant, while it is kept the same as in pure xenon, within the experimental uncertainties, for higher electric fields, where fluctuations related to Fano factor are dominant, given the large number of collected EL photons in the LAAPD.

### 8.2.1 Intrinsic energy resolution

The energy resolution obtained in mixtures is limited by the  $w$ -value correspondent to pure helium, around 46 eV. Hence, from the simulations studies [34] the intrinsic energy resolution of xenon-helium mixtures is expected to remain stable as long as the helium concentration is kept below 20%.

Figure 8.5 depicts the square of energy resolution as function of the centroid inverse (of the 5.9 keV peak) for helium concentrations of 10 %, 15 %, 20 % and 30 %. A linear function is fitted to the data points, excluding those with the highest and lowest amplitudes that depart from the linear trend. This is the same behaviour observed before in standard GPSCs. Due to the low statistical uncertainty in the Gaussian centroid, the error in  $1/A$  is not presented, whereas the error in  $R_E^2$  is correspondent to 6 %.

Table 8.2 summarises the average intrinsic energy resolution and Fano factor obtained for the several studied helium concentrations, obtained from the fit lines y-interception shown in 8.5.

Table 8.2: Intrinsic energy resolution and Fano factor obtained from linear fits in the experimental data for the mixtures performed.

He concentration	$R_{int}$	Fano factor
10 %	$5.8 \pm 0.5$	$0.17 \pm 0.04$
15 %	$6.0 \pm 0.3$	$0.18 \pm 0.04$
20 %	$6.1 \pm 0.3$	$0.18 \pm 0.04$
30 %	$5.9 \pm 0.5$	$0.17 \pm 0.04$

As observed, the impact of helium on the detector intrinsic energy resolution is negligible, at least within our experimental uncertainties. This result agrees with theoretical expectations from [34], where the Fano factor was found to be roughly constant for helium concentrations up to 30 %. The Fano factor values shown in table 8.2 are also similar to the ones

experimentally obtained with pure xenon in a driftless-GPSC [30, 32] and regular GPSCs [113, 133, 134].

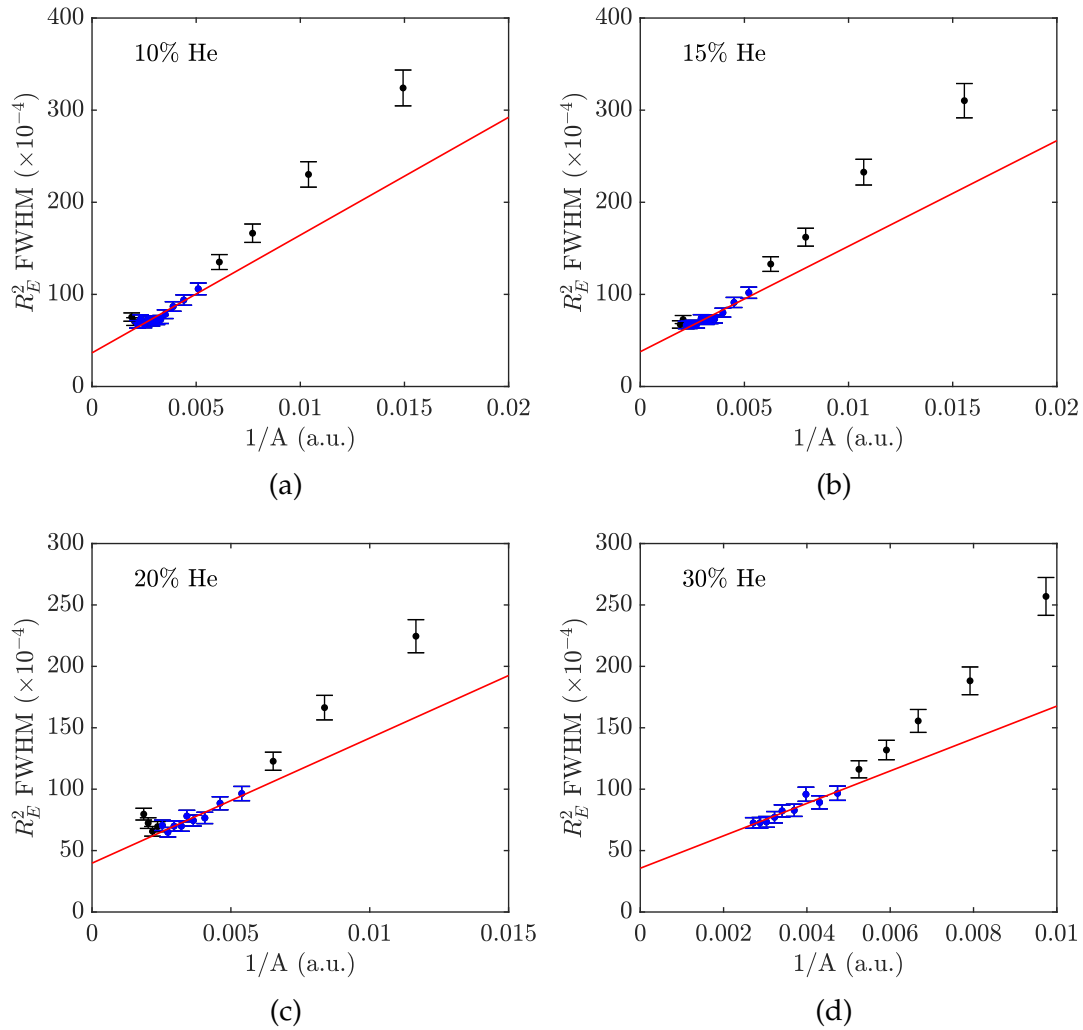


Figure 8.5: The square of the energy resolution,  $R_E^2$ , as function of the peak centroid's inverse of 5.9 keV pulse height distribution for Xe-He mixtures. The solid lines are linear fits to the selected data points (blue circles). a) 10% He, b) 15% He, c) 20% He, d) 30% He.

In the present study, the impact of helium on the relative fluctuations related to EL photon production (Q-factor) was not evaluated. According to simulations, the Q-factor is expected to deteriorate 20 % for an electric field of 2 kV/cm/bar, from pure xenon to a mixture with 15 % helium [34]. However, even in xenon-helium mixtures, the Q-factor is 3 orders of magnitude lower than the Fano factor, assuming the electric field region of interest of NEXT [34]. Thus requiring a highly sensitive experiment to measure this parameter.

The experimental results from figures 8.1 and 8.4 are a proof that helium addition to xenon in the range concentrations of 0-30 % does not significantly deteriorate the EL yield neither the associated statistical fluctuations, as it was foreseen in simulation results. Hence, concerning the EL performance, helium is a much better option to be used as additive to pure xenon in optical TPCs than molecular additives.



## Chapter 9

# Drift velocity and longitudinal diffusion

The main advantage of doping the NEXT detector's xenon filling with helium is the electron diffusion reduction, hence improving the TPC position resolution. The electron drift velocity enhancement is also beneficial, despite not being critical in a rare event experiment such as NEXT. Therefore, measuring these parameters experimentally is also relevant to fully understand the viability of xenon-helium mixtures in the NEXT context.

The transverse diffusion cannot be measured using a regular GPSC, due to the lack of a position sensitive readout. Nonetheless, the electron drift velocity and the longitudinal diffusion can be evaluated using the photosensor signal over time. In order to understand the helium impact on both parameters under the GPSC operation conditions, a Magboltz simulation was carried out for pure xenon and for a xenon-helium mixture with 30 % of helium concentration.

Figure 9.1 shows the simulated electron drift velocity, as well as the longitudinal electron diffusion (in units of length per squared root drifted path length) for a wide range of reduced electric fields [136]. As observed, for the typical drift reduced electric field (i.e., below 0.7 kV/cm/bar), the drift velocity is more than twice higher with the addition of helium, whereas the longitudinal diffusion is reduced by about 40 %.

The significant impact of helium, expected on these two electron drift parameters, for the relatively high helium concentration of 30 %, is a good motivation to use our GPSC, and therefore, to study the electron drift velocity and the longitudinal diffusion as well.

In a recent research, the electron drift velocity and the longitudinal diffusion were measured for several reduced electric fields, for pure xenon and xenon-helium mixtures with helium concentrations up to 15 %, at pressures in the range of 1-9 bar [35]. The electron drift velocity and

longitudinal diffusion were found to be in agreement with those Magboltz predictions, either in pure xenon or xenon-helium mixtures, except for very low electric fields, where the experimental longitudinal diffusion is significantly larger than the theoretical one.

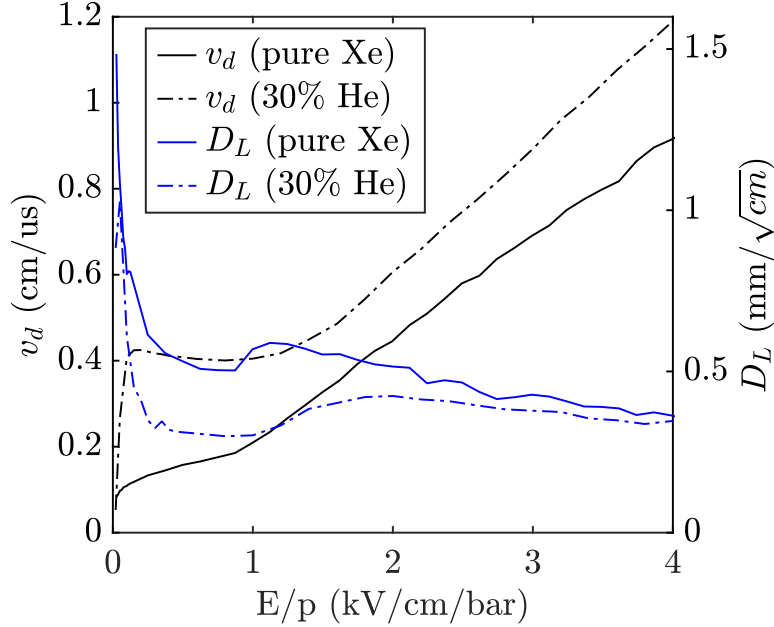


Figure 9.1: Magboltz simulation [129] of the drift velocity and  $D_L$  for pure xenon and for a mixture of 30%-He, both with a total a pressure of  $\sim 1.1$  bar [136].

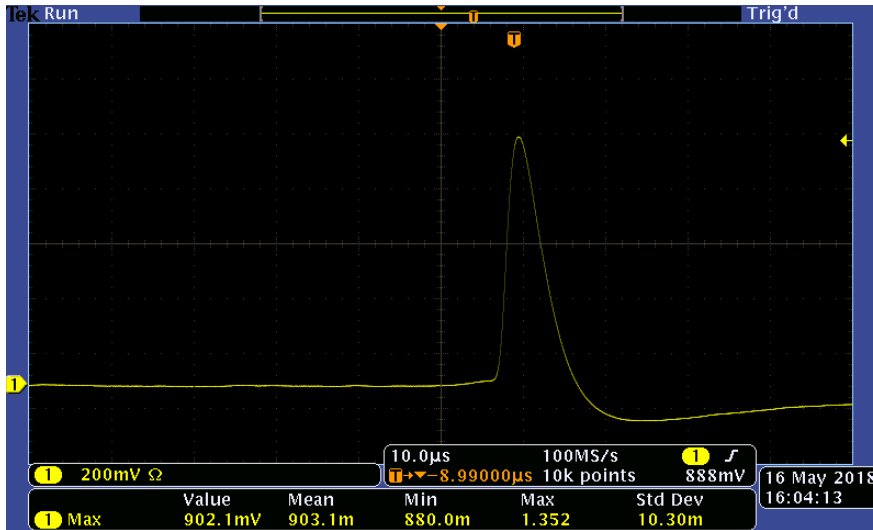
## 9.1 Primary scintillation: x-rays

In order to evaluate the electron drift velocity and longitudinal diffusion, the start of events needs to be established, being this only accessible through the detection of the primary scintillation signal. In the previous simulations it was verified that for helium concentrations lower than 20 %, the likelihood of primary scintillation is nearly the same as it is in pure xenon [34]. Hence, S1 is not expected to be quenched with a 30 %-He concentration.

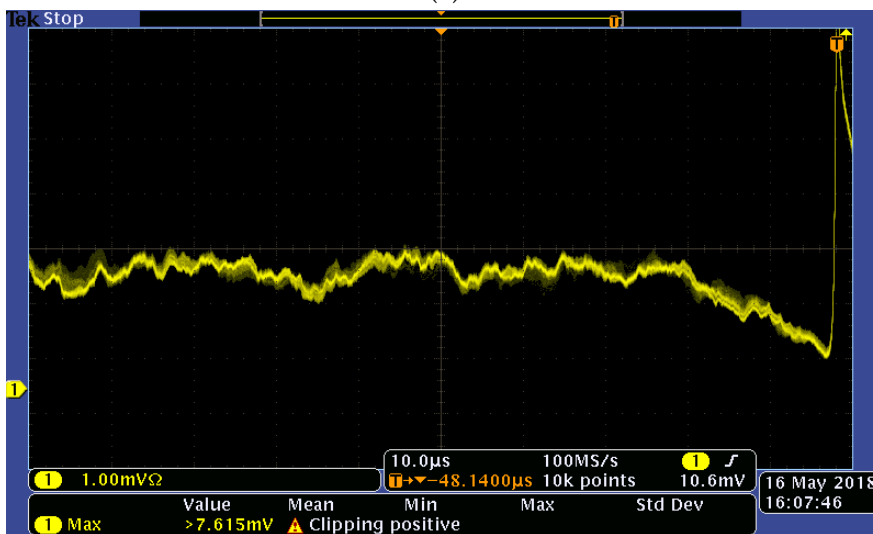
Since the primary scintillation produced by x-rays is more than 3 orders of magnitude lower than the secondary scintillation, the amplitude of S1 can be difficult to distinguish from electronic noise [132].

In a first attempt to detect this weak signal, a digital oscilloscope was used to record 512 waveforms at the linear amplifier output, averaging out the noise into a very low level. The secondary scintillation pulse was used as trigger, since it takes place a few microseconds later than the primary scintillation pulse, due to the transit time of primary electrons in the drift region. This technique was successfully used before in [14, 137]. Accordingly, in the present work it was used a Tektronix DPO 3054 oscilloscope, being the

reduced electric fields applied in the drift and scintillation regions of 0.6 and 2 kV/cm/bar, respectively, for a xenon-helium mixture with a 20 %-helium concentration. The result is shown in Figure 9.2, where the primary scintillation signal is not distinguishable from the electronic noise, despite the averaging method being used. This limitation can be explained by the low LAAPD gain of 150, together with low statistics of the sample acquired with the oscilloscope. In opposition to PMTs, LAAPDs do not have the ability to perform single-photon detection [14, 132].



(a)



(b)

Figure 9.2: (top): Secondary scintillation pulse observed in the oscilloscope, after averaging 512 events produced by 5.9 keV x-rays in the gas volume for Xe-20%He mixture. (bottom): baseline zoom of the waveform presented in a).

## 9.2 Primary scintillation: alpha particles

In contrast to x-rays, alpha particles have a shorter penetration in the gas, even for energies as high as 2 MeV. Such an increase in the deposited energy, from 5.9 keV to 2 MeV, makes the S1 detection less challenging, as the primary scintillation light emission will be more than 100 times larger. Therefore, an  $^{241}\text{Am}$  radioactive source was used to radiate the GPSC with 5.5 MeV alpha particles.

The alpha particles interaction with the gas produces an ionisation track rather than a localised electron cloud, as the one produced by low energy x-rays. Thus, in order to measure the electron drift velocity, the secondary scintillation signal must be considerably delayed from S1, otherwise S1 will be superimposed with the S2 Gaussian left-tail. Therefore, the alpha particles' penetration into the drift region must be short. Moreover, the precision of the longitudinal electron diffusion measurement is also enhanced with a short ionisation track, since the initial electron spread is summed in quadrature with the diffusion broadening. For this reason, the alpha particles energy must be finely controlled in order to keep minimal the length of ionisation tracks produced inside the detector.

The electron charge distribution deposited along the drift region by alpha particles was simulated using the package Stopping and Range of Ions in Matter (SRIM) [138]. In this way, the alpha particles penetration into the gas can be estimated, considering the energy lost in the several physical layers before reaching the gas volume.

Due to the protective gold film that covers the  $^{241}\text{Am}$  source surface, the alpha particles effective energy is about 4.8 MeV. Before reaching the gas volume, the alpha particles still need to cross 2 mm of atmospheric air, and a 6  $\mu\text{m}$  layer of Melinex, corresponding to the detector's window. An additional 10  $\mu\text{m}$  aluminium layer was placed between the radioactive source and the detector window, in order to further reduce the alpha particles energy, down to 1.8 MeV. In this way, the ionisation tracks produced in the gas were shortened into a few millimetres, according to the SRIM simulation.

Figure 9.3 illustrates the path (projected in the yz plane) travelled by 100 alpha particles, starting in the  $^{241}\text{Am}$  source (zero depth) until being fully stopped in the gas volume (red points), for a xenon-helium mixture with 30 % helium. As observed, the alpha particle tracks (represented in blue) only start diverging after 2 mm. Since this first layer consists in atmospheric air, the energy loss is still minimal until 2 mm, where the two denser layers (Melinex and aluminium) are placed, being then followed by the gas volume.

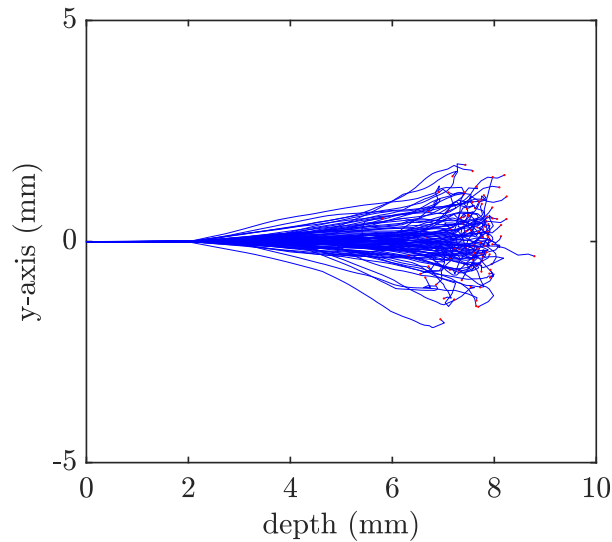


Figure 9.3: Projection of the tracks produced by 100 alpha particles on the yz-plan, obtained from a SRIM simulation for a Xe-30%He mixture. The blue tracks represent the path travelled by alpha particles, starting at the  $^{241}\text{Am}$  source, passing through 2 mm of air at 1 bar, 10  $\mu\text{m}$  of aluminium and 6  $\mu\text{m}$  of Melinex, until being fully stopped in the gas mixture, whose end-position is represented by red points.

In order to compute the experimental electron drift velocity, the estimation of the mean path length drifted by electrons along the drift region is needed. In addition, the electron cloud initial spread is required, so it becomes possible to estimate the longitudinal electron diffusion. Therefore, the deposited energy distribution by alpha particles in the gas volume projected along the z-axis was also simulated using SRIM. The result is shown in figure 9.4, for pure xenon and for a xenon-helium mixture with 30 % helium.

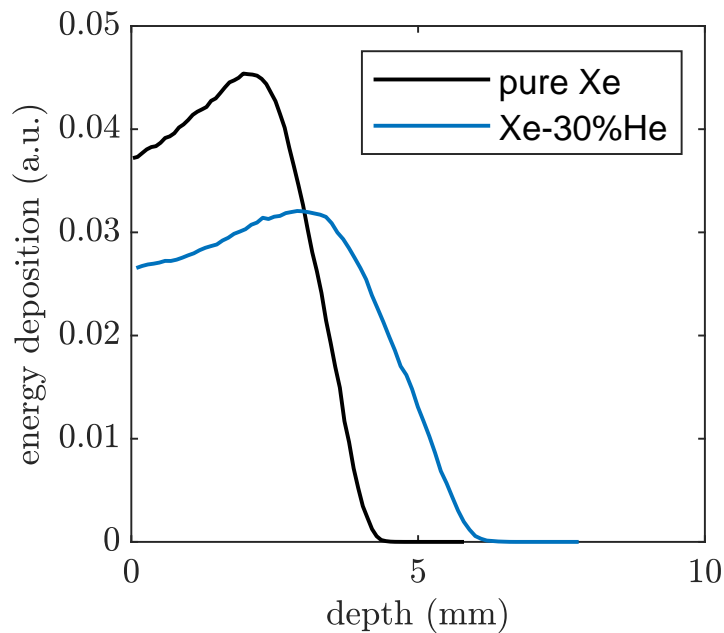


Figure 9.4: Relative energy deposited in the gas volume by alpha particles along the z-axis, obtained from a SRIM simulation, for pure xenon and for a Xe-30%He mixture at 1.1 bar.

The deeper penetration of alpha particles in the xenon-helium mixture observed in figure 9.4 is attributed to the lower gas density, since the atomic mass of helium atoms is significantly lower than the xenon atomic mass. The mean path length drifted by the ionisation electrons in the GPSC drift region was estimated to be around 2.22 cm for pure xenon and 2.17 cm for the 30 % helium mixture.

Despite the large amount of scintillation photons released during a single alpha particle interaction, S1 is still indistinguishable from the electronic noise, due to the low LAAPD gain. Therefore, we need to average the waveforms produced by several interactions, as performed in section 9.1. However, the more reliable data acquisition and analysis methodology described in section 6.2.3 is now used. This includes the algorithm to reject background events, and the careful waveform alignment based on the instant that the EL amplitude reaches 50 % of its maximum value.

Figure 9.5 depicts a typical waveform obtained by averaging 2000 waveforms produced by alpha particle interactions in the GPSC filled with pure xenon. In contrast to the figure 9.2, the primary scintillation signal is now clearly distinguishable from the baseline electronic noise, allowing to measure the electrons mean drift time. From the ratio between S1 and S2 areas, the primary scintillation signal can be estimated as a factor of  $6 \times 10^4$  lower than the one of electroluminescence. This result demonstrates the technical difficulty to detect the weak primary scintillation signal produced by 5.9 keV x-rays referred in section 9.1.

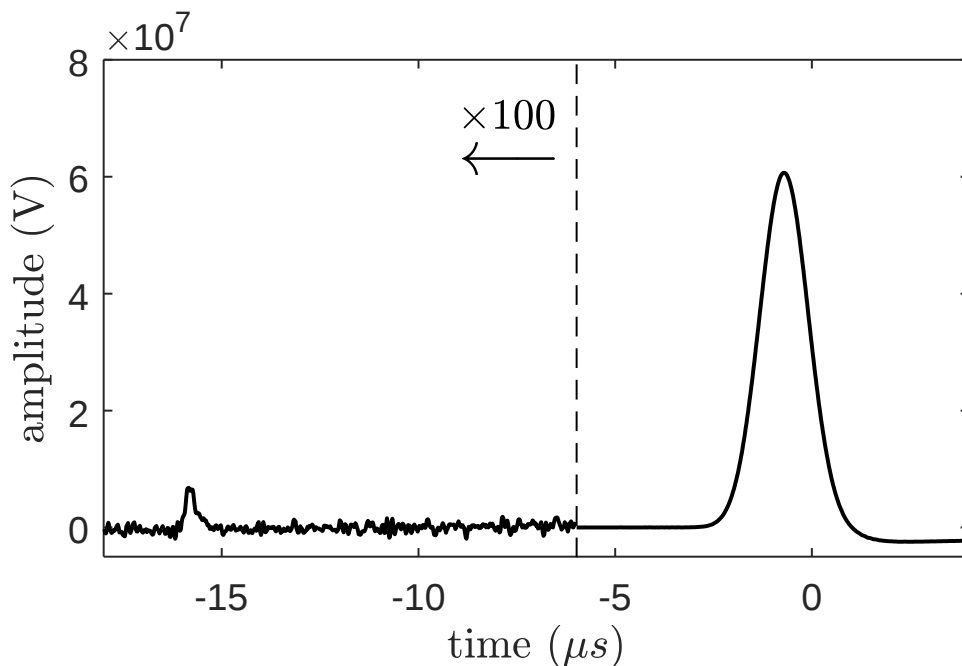


Figure 9.5: Typical average waveform produced by alpha particles in pure xenon at 1.1 bar, for a mean reduced electric field of 376 V/cm/bar in the drift region, and a reduced electric field of 2.7 kV/cm/bar in the EL region.

### 9.3 Electric field

The electric field in the EL region is approximately uniform, due to the large delimiting grids in combination with the short gap between them (see figure 6.1). On the other hand, the electric field in the drift region is not uniform, since no field grading structure was used. Nonetheless, the main source of electric field distortion in this region is the detector focus cup, which is usually used to focus the ionisation electrons into the EL gap central region, hence reducing geometrical effects. For this reason, the electric field inside the GPSC along the z-axis was simulated using the Elmer finite element solver [139, 140]. The result is shown in figure 9.6 for several voltage differences across the drift region.

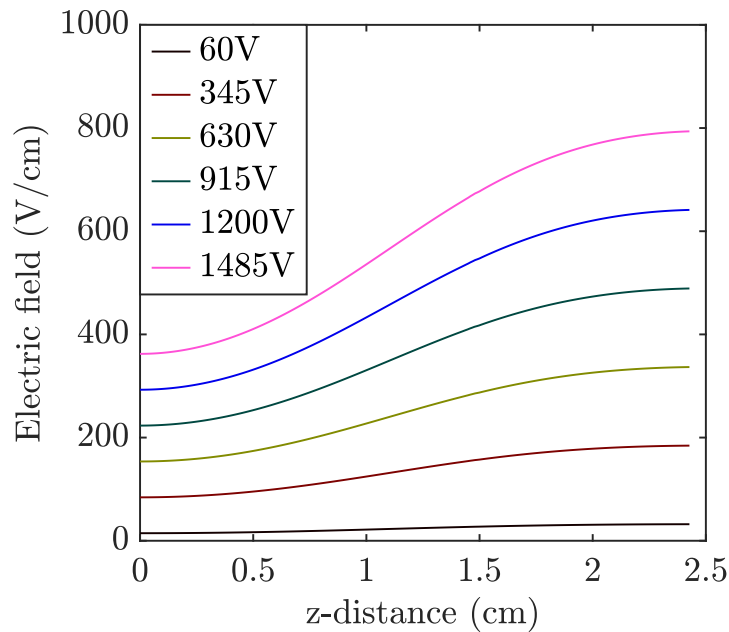


Figure 9.6: GPSC simulated electric field along the z-axis using the Elmer finite element solver [139, 140].

As expected, the electric field is weaker near the detector window, growing towards the EL region, with a significant variation of more than 50 %.

Since both the electron drift velocity and longitudinal diffusion depend on the reduced electric field, these parameters cannot be accurately measured under a non-uniform electric field. Nevertheless, the impact that helium has on the electrons' transport in the drift region can still be evaluated from the time elapsed between S1 and S2, which is inversely proportional to the mean electron drift velocity. In addition, the secondary scintillation pulse width, is strongly dependent on the longitudinal electron diffusion. Despite the duration of S2 to be affected by the drift of electrons in the absorption region, it is also determined by the drift velocity and longitudinal diffusion of

electrons inside the EL region. In order to minimise the electron transport contribution occurring in the EL region, the time elapsed from S1 to S2 is measured between the centroid of S1 and the instant when S2 reaches 50 % of its maximum amplitude (corresponding approximately to the time when the centroid of the electron cloud reaches the EL region), while S2 duration is measured in the rising edge between 10 % and 90 % of the signal maximum amplitude.

These two measurements alone don't allow to take quantitative conclusions concerning the fundamental electron drift parameters. Therefore, it is required a GPSC waveforms simulation in order to understand the helium impact on both the electron drift time and the secondary scintillation rise time. In this way, the electric field gradient simulated for the drift region (figure 9.6) can be used together with the theoretical electron drift velocity and longitudinal diffusion (figure 9.1) to modulate the detector response, which can then be compared with the experimental results.

## 9.4 Electron transport theory

The first step for the GPSC waveform modulation consists in the electron drift simulation in both absorption and EL regions, projected along the axis that follows the electron drift direction. The hydrodynamic approximation of Boltzmann equation can be used to describe the electron cloud evolution along its drift [10]:

$$\frac{\partial N_e}{\partial t} + v_d \frac{\partial N_e}{\partial z'} - D_T^* \left( \frac{\partial^2 N_e}{\partial x'^2} + \frac{\partial^2 N_e}{\partial y'^2} \right) - D_L^* \frac{\partial^2 N_e}{\partial z'^2} = -\eta v_d N_e \quad (9.1)$$

where  $N_e$  represents the electrons density per unit of volume,  $D_T^*$  is the transverse diffusion coefficient,  $D_L^*$  is the longitudinal diffusion coefficient,  $v_d$  is the drift velocity and  $\eta$  is the attachment coefficient. One should note that  $D_L^*$  and  $D_T^*$  represented in equation 9.1 are in natural units, i.e. the quadratic electron spread per unit of time ( $L^2 T^{-1}$ ), while the  $D_L$  values in figure 9.1 are represented in a more intuitive way, i.e. electron spread per root squared drifted path length ( $L L^{-1/2}$  or  $L^{1/2}$ ). Consequently, the  $D_L$  values shown in figure 9.1 need to be converted to the correct units in order to be used in equation 9.1, through  $D_L^* = v_d D_L^2 / 2$ . Now, solving equation 9.1, one may obtain the density of electrons:

$$N_e(x', y', z', t) = \frac{e^{-\frac{(x'-x)^2 + (y'-z)^2}{4D_T^*(t-t_0)}} e^{-\frac{((z'-z) + v_d(t-t_0))^2}{4D_L^*(t-t_0)}}}{(4\pi D_T^*(t-t_0)) (4\pi D_L^*(t-t_0))^{1/2}} \times \bar{n}_e e^{-\eta v_d(t-t_0)} \quad (9.2)$$

with  $(x', y', z', t)$  being measurable variables, while  $(x, y, z, t)$  correspond to the initial position and time of the ionisation cloud occurrence, containing  $\bar{n}_e$  electrons.

Neglecting the electron attachment, which is a good approximation for pure xenon and for xenon-helium admixtures as well, and projecting the electrons density,  $N_e$  along the drift direction i.e., on the  $z$  dimension, the equation 9.2 becomes simplified into a one-dimensional Gaussian function whose standard deviation is directly proportional to the square root of time ( $\sigma = \sqrt{2D_L\Delta t}$ ) and the centroid is directly proportional to the time, i.e.,  $centroid = v_d\Delta t$ . In this way, the evolution of the one-dimensional electron cloud can be easily simulated along the drift and EL regions, considering the initial distribution along  $z$  obtained from SRIM simulation (figure 9.4).

## 9.5 Geometric efficiency

Since the solid angle subtended by the LAAPD and the electron cloud varies along the EL gap, the waveform produced at the photosensor output cannot be determined only with the electrons longitudinal distribution. Therefore, the solid angle was also taken into account for the waveform simulation. Given the photosensor 16-mm diameter and the 8-mm EL gap, the geometrical efficiency is expected to be  $\sim 15\%$  when the electron cloud enters into the EL region and  $50\%$  when it reaches the anode. In addition to the solid angle, the geometric efficiency evolution also depends on light reflections in the detector materials and on the LAAPD window. However, these effects were not considered due to the complexity to accurately modulate VUV photon reflections on the several GPSC materials.

## 9.6 Electronics and xenon scintillation

The scintillation process in xenon is relatively fast, being dominated by the triplet state with a life time of  $\sim 100$  ns [109, 141]. Nevertheless, the effect of the xenon excimer deexcitation can be easily modulated by modifying the simulated waveform. For this purpose, a waveform numerical differentiation with a time decay of 100 ns was performed.

Another significant source of waveform distortion comes from electronics used at the LAAPD output. The first component in the signal processing chain is the pre-amplifier. This device decouples the LAAPD signal from the supplied high voltage, which is required for its operation. In addition, the pre-amplifier stores, in a capacitor, the charge produced by the LAAPD during each event detection, which is then discharged through a resistor.

Since the pre-amplifier discharge time constant used in this work is  $\sim 50 \mu\text{s}$ , a numerical integration of the simulated waveform is performed with a  $50 \mu\text{s}$  decay constant.

The next amplification stage consists in a linear amplifier, which is commonly used to mitigate the high probability of event overlapping due to the slow discharge rate of the pre-amplifier capacitor. Therefore, the linear amplifier differentiates the input signal using a high-pass filter (capacitor-resistor), which is followed by a low pass filter (resistor-capacitor). Accordingly, the linear amplifier output can be modulated in approximation using the differential equations 9.3 corresponding to the differentiation stage, and 9.4 corresponding to the integration stage, given by:

$$V_0 + \tau \frac{dV_0}{dt} = \tau \frac{dV_i}{dt} \quad (9.3)$$

$$V_0 + \tau \frac{dV_0}{dt} = V_i \quad (9.4)$$

with  $V_0$  the output voltage and  $V_i$  the input voltage signal. As described in 6.2.3, the linear-amplifier differentiation and integration time constants were set to 50 ns, in order to preserve as much as possible the original LAAPD waveform. Accordingly,  $\tau$  is assumed to be 50 ns in equations 9.3 and 9.4, which are computed numerically for the modulated pre-amplifier output, that is in its turn obtained from the simulated GPSC waveform.

## 9.7 Waveforms simulation

The distribution of ionisation electrons produced during the interaction of 5.9 keV x-rays with the gas at  $\sim 1$  bar ranges just a few tens of  $\mu\text{m}$  [121]. Therefore, the electron cloud size when it reaches the EL region is dominated by the electron diffusion.

However, the few mm long initial charge distribution produced by alpha particles cannot be neglected. For this reason, the longitudinal charge distribution simulated with SRIM, in section 9.2, is used as input for the electron transport model described in section 9.4.

The electron drift velocity and longitudinal diffusion coefficients interpolated from the Magboltz values shown in figure 9.1 are also introduced in this model, considering the reduced electric fields established across the EL and absorption regions, where the latter is interpolated from the simulated values shown in figure 9.6. The theoretical geometrical efficiency is used together with the electron transport model to simulate the waveform produced at the photosensor output, as described in section 9.5. Since the

experimental GPSC waveforms also contain the signal distortions introduced by the xenon scintillation process and the signal processing electronics, these effects are modulated numerically over the simulated photosensor waveform, as shown in section 9.6. In this way, the GPSC waveform can be simulated for the same working conditions used experimentally.

In order to validate the simulation method here developed, an experimental average waveform obtained with pure xenon is compared to the respective simulated one in figure 9.7.

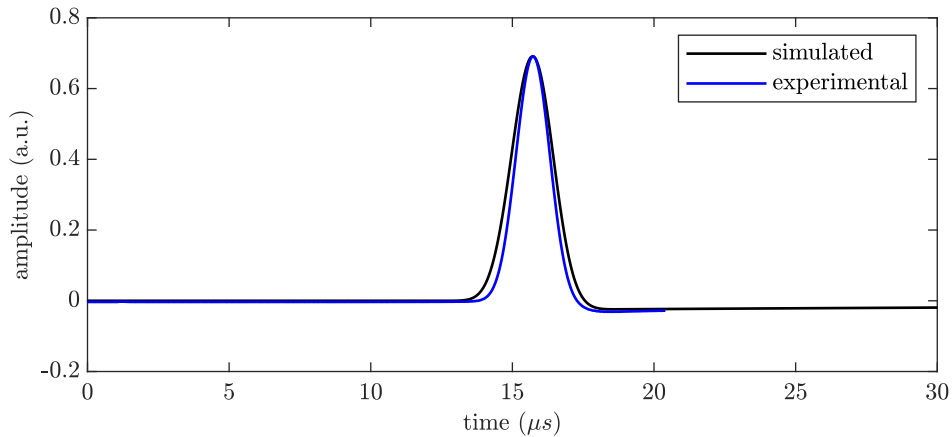


Figure 9.7: Simulated waveform and average experimental waveform, both obtained for pure xenon at 1.1 bar.

The experimental waveform consists in an average over 3500 events obtained with 1233 V applied across the drift region and 1997 V in the EL region, at a pressure of 1.1 bar. The experimental waveform is normalised to the theoretical one, so that the peak height and centroid are coincident for both waveforms.

From figure 9.7, one may observe a fair agreement between both waveforms. Nevertheless, the theoretical S2 is slightly longer than the experimental one, which is most likely due to the error in the SRIM simulation coming from the initial electron cloud distribution.

## 9.8 Results: electron drift time

The typical GPSC experimental waveform was obtained by averaging 3500 events acquired with pure xenon and a xenon-helium mixture with 30 % helium, in order to study the impact of helium in the electron drift time.

The figure 9.8 shows the drift time measured from the average GPSC waveform between the centroid of S1 and the 50 % rising edge of S2, for a wide range of voltages applied across the drift region.

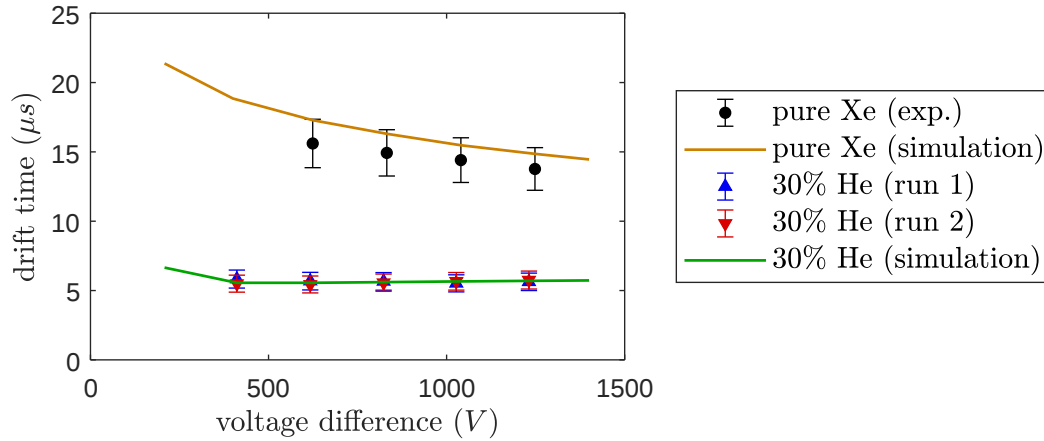


Figure 9.8: Electron drift time as a function of voltage differences applied to the drift region, for pure xenon and Xe-30 %He mixture.

The two different data series presented for the 30 % helium mixture were taken with a time interval of seven days. All data points were acquired with a total gas pressure of 1.1 bar, and for a reduced electric field applied in the EL region of 2.3 kV/cm/bar. The error bars in the graph show the systematic uncertainty for 90 % CL, being mainly related with the SRIM simulation of the alpha particles penetration in the drift region. For comparison purposes, the theoretical drift times obtained from the simulated waveforms are also plotted, for the same experimental working conditions.

Despite the two data sets plotted for the xenon-helium mixture being acquired with 7 days apart, there is no sizeable difference between them. This result confirms that the helium concentration inside the detector volume is stable and discards the xenon stratification hypothesis, at least within this time scale.

A good agreement between data and simulation can be observed in figure 9.8, with the larger mismatch of about 10 % being found for pure xenon, yet within the systematic error. As referred previously in this chapter, Magboltz simulation is expected to describe accurately the electron drift velocity, either for pure xenon or xenon-helium mixtures, within the range of reduced electric fields used in our waveform simulation [35]. Therefore, the results presented in figure 9.8 legitimate the reliability of the experimental methodology employed in the present work, being also a crosscheck for the helium concentration inside the detector volume, since this parameter was not directly measured during the experimental campaign.

## 9.9 Results: longitudinal electron cloud size

The S2 rising time was also measured from the same average waveforms used in figure 9.8, between 10 % and 90 % of the S2 peak height. Within the voltage range studied here, the rising time obtained with pure xenon was found to be almost twice the one obtained with the xenon-helium mixture. For example, the rising time is  $0.98 \mu\text{s}$  in pure xenon for an applied voltage of 1233 V, and  $0.60 \mu\text{s}$  in the mixture with 30% helium for the same voltage.

Nevertheless, this result does not allow the conclusion that the longitudinal diffusion is lower in the presence of helium, as expected from Magboltz simulations (figure 9.1). The major contribution for the difference observed in the rising time comes from the significantly higher average drift velocity in xenon-helium mixtures (figure 9.8).

Therefore, the S2 rising time values were multiplied by the experimental average drift velocity measured for the respective voltage difference, so the drift velocity influence could be reduced. Nonetheless, the parameter computed here (in units of  $L$ ) does not represent  $D_L$  (in units of  $L^{1/2}$ ), instead, it is directly proportional to the electron cloud longitudinal length when this reaches the EL region. In this way, from now on it will be called longitudinal electron cloud size, so misunderstandings can be avoided.

In figure 9.9, the longitudinal electron cloud size, obtained with pure xenon and a xenon-helium mixture with 30 % helium, is plotted as a function of the applied voltage, along with theoretical values (black and blue solid lines) computed from the simulated waveforms.

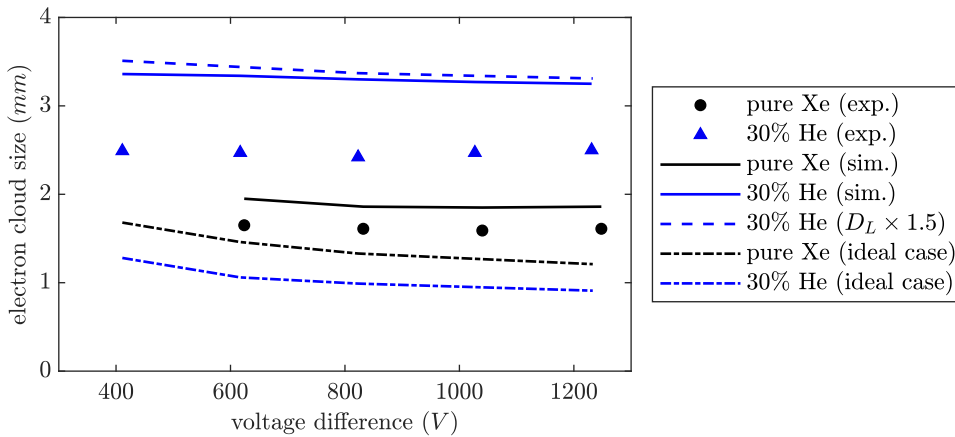


Figure 9.9: Longitudinal electron cloud size obtained with pure Xe and a Xe-30%He mixture for a wide range of voltages applied across the drift region. The simulated values are shown for several working conditions.

Regarding figure 9.9, one may notice that either the experimental or the simulated electron cloud size is actually larger in xenon-helium mixtures than it is in pure xenon, which contrasts with the expectations based on the

longitudinal electron diffusion values of figure 9.1. This apparent inconsistency is mostly attributed to the larger ionisation track produced by alpha particles in the mixture with helium, when compared with pure xenon (see figure 9.4). In addition to the real electron cloud size, the S2 rising time also depends on variation of the solid angle subtended by LAAPD along the electron drift. Therefore, the longitudinal electron diffusion contribution for the electron cloud size values shown in figure 9.9 is minor. In order to demonstrate this effect, the electron cloud size was also simulated assuming a longitudinal electron diffusion 1.5 times higher. The result is shown in figure 9.1 (dashed blue curve), showing that the effect of the significantly higher longitudinal electron diffusion upon the electron cloud size value is negligible.

In order to reach a better understanding on this issue, one may assume the ideal case, that is a punctual initial electron cloud distribution produced at the same depth in xenon and in the gas mixture, and a small EL gap of 1 mm. The simulation results considering the ideal case are also plotted in figure 9.9, for both pure xenon and the xenon-helium mixture. As expected, the electron cloud size is reduced in the presence of helium by a factor of  $\sim 0.75$ , which is in agreement with the reduction of a factor of  $\sim 0.58$  (due to the different units:  $\sqrt{0.58} \simeq 0.75$ ) expected from the theoretical longitudinal diffusion values (figure 9.1).

From these observations, one may conclude that the present apparatus and analysis methodology cannot be used to evaluate the electron longitudinal diffusion, due to the large geometrical effects and the long ionisation tracks produced by alpha particles. Even if these two effects were properly removed from the experimental values of S2 rising time, the error stemming from the SRIM and geometrical factor simulations would prevent us from detecting the subtle impact that the longitudinal diffusion has on the S2 pulse shape.

In figure 9.9, a moderate mismatch between experimental data (blue triangles and black circles) and the simulated curves (blue and black solid curves) may still be observed, specially for the xenon-helium mixture. A possible explanation for this inconsistency arises from the error on primary charge distribution from SRIM simulation. This result reinforces the poor reliability of the present methodology and experimental conditions to be used in order to evaluate the longitudinal electron diffusion.

# Chapter 10

## The relevance of helium contrasting with molecular mixtures

Despite the impact of helium on xenon electroluminescence performance have been found negligible in the present work, the helium addition in xenon results in the reduction of the overall  $^{136}\text{Xe}$  mass which, per se, contributes to the TPC sensitivity reduction to  $\beta\beta 0\nu$  detection.

The sensitivity to  $m_{\beta\beta}$ , the so-called effective Majorana mass of the electron neutrino in experiments searching for  $0\nu\beta\beta$ , i.e., the lower limit that an experiment may achieve for  $m_{\beta\beta}$  is given by [4]:

$$S(m_{\beta\beta}) = k\sqrt{\frac{\bar{N}}{\varepsilon Mt}} \quad (10.1)$$

where  $k$  is a constant,  $\bar{N}$  is the average upper limit on the number of observed events expected in the experiment under the no-signal hypothesis,  $\varepsilon$  is the signal detection efficiency,  $M$  is the source mass and  $t$  is the measurement time.

When a dominant background like  $2\nu\beta\beta$  is present, the average upper limit for  $\bar{N}$  is proportional to the square root of the mean number of background events, i.e.  $\bar{N} \propto \sqrt{b}$ . Besides, the number of background events is usually proportional to the exposure,  $M t$ , and to the width of the energy window,  $\Delta E$ , defined by the detector energy resolution:  $b = c \cdot M \cdot t \cdot \Delta E$ , where  $c$  is the expected background rate. Therefore, the sensitivity becomes dependent on [4]:

$$S(m_{\beta\beta}) \propto \frac{\Delta E^{\frac{1}{4}}}{M^{\frac{1}{4}}} \quad (10.2)$$

Thus, a loss of mass in xenon due to the addition of a significant helium amount will have consequences in the TPC sensitivity. Considering the 3-dimensional diffusion coefficient,  $D_{3d}$ , as a reference parameter, defined as the characteristic size of the electron diffusion ellipsoid,  $\sqrt[3]{xyz}$  after 1 m drift

through the TPC,  $D_{3d} = \sqrt[3]{D_L \times D_T^2}$  (mm/ $\sqrt{m}$ ) [32], an amount of 15 % helium will be needed in order to reduce this 3D diffusion coefficient from  $\sim 9.5$  mm/ $\sqrt{m}$  in pure xenon down to 2.65 mm/ $\sqrt{m}$ , according to [34].

Since there is no degradation in the TPC resolution, according to the present studies, the consequent reduction of  $^{136}\text{Xe}$  mass in 15 % will therefore result in a TPC sensitivity degradation of  $\sim 4.1$  %. Nevertheless, although the reduction in the target mass imply a reduction effect on the sensitivity, the improvement of the electron diffusion and, ultimately, on the topological discrimination efficiency to background, which is not considered in eq. 10.2, will enable a more sensitive search for  $\beta\beta 0\nu$ . In addition, the resulting increase in the electron drift velocity will have a positive reduction in electron attachment to impurities, which are non-trivially distributed throughout the detector, and will add some space- and time-dependent fluctuations to the charge yields as well as to charge loss.

The above mentioned sensitivity reduction needs to be compared with the results achieved with  $\text{CH}_4$  addition to pure xenon in concentrations of 0.15 %  $\text{CH}_4$  which is required to reach the same 3D diffusion of 2.65 mm/ $\sqrt{m}$  [32], assuming that a similar background suppression can be achieved for both types of low-diffusion mixtures. With the  $\text{CH}_4$  addition, it is considered that there is no variation in the  $^{136}\text{Xe}$  mass, and the energy resolution degradation measured in [32] leads to a  $\beta\beta 0\nu$  sensitivity reduction of  $\sim 1$  % and 3 %, for a light collection efficiency of 3 % and 0.5 %, respectively, yet considering an additional 0.5 % constant contribution to the overall energy resolution in the NEXT TPC [13].

However, in an experiment like this, where the backgrounds subtraction has a major importance, being dominated by the natural radioactivity from the TPC materials, such as  $^{208}\text{Tl}$  and  $^{214}\text{Bi}$  in the TPC components, as in NEXT-NEW [142], then the background counts will not depend upon the mass,  $M$ , being  $b = c \cdot t \cdot \Delta E$ , and consequently:

$$S(m_{\beta\beta}) \propto \frac{\Delta E^{\frac{1}{4}}}{M^{\frac{1}{2}}} \quad (10.3)$$

Therefore, assuming the number of background events is not affected by the lower  $^{136}\text{Xe}$  mass in xenon-helium mixtures, the TPC sensitivity degradation will be 8.5 % for Xe-15%He, to be compared with an impact on the TPC sensitivity of 1-3 %, estimated for  $\text{CH}_4$  mixtures of sub-percent concentration.

Therefore, a compromise has to be established, taking into account this reduction in sensitivity, as well as the advantages of using helium as an additive instead of molecular gases, and the gain in sensitivity due to a more efficient topological discrimination.

Thus, other practical aspects such as the primary scintillation quenching induced by  $\text{CH}_4$ , the long term purification and stability will need to be considered as well. These issues are to be investigated in larger TPC prototypes such as NEXT-DEMO and/or NEXT-NEW in subsequent R&D programs. A direct measurement of electron transverse diffusion is still pending, as well as the pressure scaling assumption that the 1 bar measurements can be extrapolated to 10 bar at the same  $E/p$ .



# Chapter 11

## General conclusions

In order to accomplish the tracking plane reconstruction, there are some inherent effects to the interaction of electrons which must be taken into account, such as bremsstrahlung photons, delta rays emitted by electrons, and electron cloud diffusion during drift, among others. It is then required a good resolution in order to record a precise position.

The signal topology is limited by the electron diffusion effect during drift, which it is believed that could be improved with additives. Some studies have been performed where the properties of the drift electrons in TPCs were measured, its diffusion, as it were the EL production effects and energy resolution as well.

Helium appears to be a better solution when compared to molecular additives, since it is a noble gas, not suffering effects of vibrational and rotational states, happening while using molecular species. The major problem while using molecular additives is the quenching effect, as well as attachment that drives to the reduction of S1 and S2, degrading the energy resolution. Nevertheless, those effects are not expected to happen with helium. Thus, with the use of helium as an additive to pure xenon, the detector performance in terms of electroluminescence is expected to be near the one obtained with pure xenon.

Thence, recently it were performed experimental studies where the electron diffusion was studied, by [35], for xenon admixtures with helium. The longitudinal diffusion in xenon-helium mixtures is found to be larger than anticipated in simulations by around 50 % and larger than in pure xenon. Still suggesting that using helium as an additive will allow a substantial improvement in the transverse diffusion reduction, thus remaining a promising prospect.

With this work is experimentally confirmed that the addition of helium to pure xenon at concentration levels of 0-30% does not reduce the gas-mixture electroluminescence yield in a significant way. With a reduced electric field of

2.5 kV/cm/bar in the scintillation region, there was a reduction by ~2%, 3%, 6% and 10% on the EL yield for 10%, 15%, 20% and 30% helium concentration, respectively. Moreover, no degradation was observed in the detector energy resolution with the helium addition to pure xenon.

Concerning electroluminescence threshold, values of 0.77 kV/cm/bar, 0.80 kV/cm/bar, 0.85 kV/cm/bar and 0.91 kV/cm/bar were achieved for 10 %, 15 %, 20 % and 30 % of helium, respectively. This threshold is slightly degraded by increasing the helium amount, being this difference negligible for the studied concentrations.

Nevertheless, it is clearly noted that the impact of the helium addition on the EL yield decrease is lower than that foreseen by recent simulation framework in the literature results. For reduced electric fields of 2.5-3.5 kV/cm/bar the energy resolution results achieved for all xenon-helium mixtures were extremely positive, with values of  $8.54 \pm 0.2 \%$ ,  $8.52 \pm 0.2 \%$ ,  $8.46 \pm 0.2 \%$  and  $8.93 \pm 0.2 \%$  for 10 %, 15 %, 20 % and 30 % helium, respectively, while for pure xenon the energy resolution obtained was  $8.56 \pm 0.2 \%$ . Therefore, these results prove, for the studied concentrations, that the addition of helium to xenon does not significantly affect the energy resolution.

These results, combined with those obtained for the drift-diffusion properties in the range of 1-10 bar by [35], reinforce the potential of xenon-helium admixtures for  $\beta\beta$  searches. Therefore, the present results reinforce the need for experimental studies of the electron transverse diffusion in these mixtures.

The helium addition to xenon results in a correspondent loss of xenon mass in the TPC, which should be compared to the negligible impact on the xenon mass loss in admixtures with molecular additives. In order to reach an electron diffusion value close to the thermal limit with molecular additives, it would be needed only sub-percent concentrations, while with helium would be necessary concentrations around 15-20%. This amount of helium would result in a sensitivity degradation of ~4-6% in the TPC to  $m_{\beta\beta}$ , in the case that background is dominated by  $2\nu\beta\beta$  decay. On the other hand, if the background is dominated by natural radioactivity of the TPC components, the degradation on the  $m_{\beta\beta}$  sensitivity due to xenon mass reduction would be ~8-12%. After all, these numbers may still be competitive in face of the advantages related with the use of helium as an additive, replacing a molecular one. However, if the helium concentration should have to rise until levels around 30 % in order to produce a significant reduction on electron diffusion, then the respective reduction in the  $m_{\beta\beta}$  sensitivity would be ~10 % and 20 % for the two above cases. Then, a careful evaluation of pros and cons

on the option presented in this work, namely in degradation of  $m_{\beta\beta}$  sensitivity due to lower  $\beta\beta$  source mass versus improvement of background discrimination in the TPC, should be taken into account.

The present results are an important benchmark for the simulation tools to be applied to future optical TPCs based on xenon-helium mixtures. Summing up, the purposed goal of reducing the electron diffusion for EL TPCs with xenon filling might be possible to achieve with the use of helium, as an alternative to molecular additives. Nevertheless, the amount of helium needed still have to be studied carefully, especially when high pressure operation is needed, in comparison with molecular additives, where the sub-percent levels needed are negligible, not compromising the amount of xenon available as source and detection medium.

The work presented in this thesis has its importance on several aspects referred as follows.

The experimental validation of the possibility to use xenon-helium mixtures with helium concentrations between 10 and 20 % without having a significantly reduction on electroluminescence, not compromising this parameter, then validating the use of xenon-helium mixtures as filling of NEXT's TPC.

The proof and showing that the experimental electroluminescence yield presents a lower variation than the one predicted by simulations, even for helium concentrations above 20 %.

The ability to show that the helium addition to xenon, at least in concentrations until 30 %, does not jeopardise the detector outcome in terms of its energy resolution.

## 11.1 Future work

For future work, following everything that has been done so far, some proposals are presented below.

The validation for the achieved conclusions in this work in a detector with bigger dimensions, such as NEXT-DEMO++, for pressures of 10-15 bar, measuring the longitudinal and transverse diffusion and evaluate any possible electroluminescence dependence and its statistical fluctuations as well, with the filling pressure. This work has already started.

To study the GPSC outcome with xenon-helium mixtures, with xenon concentrations of 5 to 30 % to low energy x-rays. This would be a similar study to the one performed for neon-xenon mixtures. With neon being much more expensive than helium and once there are already available solid-state

VUV photosensors with high quality, helium might be a more affordable alternative, yet being more efficient in order to minimise the effect on the loss of electrons to the GPSC window on the detection of low energy x-rays, whose gas penetration is much smaller. However, it is bigger on xenon-helium mixtures than it would be on neon-xenon admixtures.

The study on the unconformity found on electroluminescence experimental results, related to results achieved by simulation, becomes necessary, since those discrepancies need to be understood in order to perform forward simulations with high confidence level on the results for the electroluminescence produced on NEXT TPCs.

The study of Neutral Bremsstrahlung in pure xenon, as well as in xenon-helium mixtures. This effect was hypothetically pointed as a possibility which might explain the observed discrepancy between experimental results and the simulated ones, on the scintillation amount emitted by drift electrons in the scintillation region. The study on Neutral Bremsstrahlung emission is already in course for pure xenon.

The effects of molecular additives on the electron drift along the low-intensity electric field region (drift region), and on the primary scintillation yield achieved in each mixture are still to be analysed, since these studies were not possible to be performed before with the driftless-GPSC. Thus, we already added a standard GPSC to the experimental setup used in the studies with molecular additives, to be operated in parallel and simultaneously with the driftless-GPSC. The former studies will then be complemented with this analysis, as well as the time profile of EL pulses, in order to look for the possibility to extract information on the longitudinal diffusion and attachment. The comparison of attachment occurring in the 1-cm thick scintillation region of the standard-GPSC and that of 2.5-cm thick region in the driftless-GPSC will provide a deeper understanding of this effect. New additives are also being studied, in particular  $C_2H_6$ . This molecule belongs to the same family of  $CH_4$  and might be one of the potential candidates to be used in NEXT-100 detector, as already was assumed by the NEXT collaboration.

On the other hand, the determination of scintillation probability in those mixtures will serve as a test to the simulation model that has been developed by the NEXT Collaboration. The EL yield predicted by this model in Xe- $CH_4$  mixtures is lower than the one obtained experimentally and, from experimental results for Xe- $C_2H_6$  mixtures, it will be possible to understand if there is a problem in the model or else, if  $CH_4$  behaviour is an exception.

Following studies of Xe- $CH_4$ , Xe- $CO_2$  and Xe- $CF_4$  mixtures. These studies will be performed in a standard-GPSC and in the driftless-GPSC, for

comparison. The time-profile of the pulses will be evaluated (in particular for the Xe-CH<sub>4</sub> and Xe-CO<sub>2</sub> mixtures, for which such study has not yet been performed). The primary scintillation yield and possible quenching will be measured and the scintillation probability will be accessed.

Study of the gas pressure effect for the selected mixtures. These studies will be performed using both the standard-GPSC and the driftless-GPSC, operated at pressures of 1.01, 1.33 and 2.0 bar. This study is important in order to evaluate the methodology already followed to extrapolate the results obtained at 1 bar for the operation conditions of NEXT-100, namely 10 bar. In addition, it will be a test to the simulation model relative to quenching and attachment, contributing to the full understanding of those parameters behaviour.

Detailed research of NEXT-DEMO prototype, filled with the selected mixture, among the aforementioned possibilities, that has shown, in the first phase, the more promising potential for NEXT. If necessary, additional mixtures may also be tested in NEXT-DEMO detector. The parameters described below must be fully understood, in a first stage, operating the detector at a pressure of 1 to 5 bar, and, in a second stage, with pressures between 5 and 10 bar, in order to understand the dependence of these parameters on the gas pressure, such as the effect on the energy resolution achieved in NEXT-DEMO, the effect on the primary scintillation yield, the gas transparency to xenon scintillation, the effect on electron attachment in the drift region of the detector, and for drift distances up to 30 cm and determination of transverse and longitudinal diffusion coefficients as well. These activities already started at IFIC Laboratories, in University of Valencia (in collaboration with researchers from NEXT Collaboration).



# List of Figures

3.1	Drawing of the NEXT-100 lead castle shield in its open configuration [8]. . . . .	18
3.2	The concept in NEXT experiment [8]. . . . .	18
3.3	The NEXT-100 apparatus from [77]. . . . .	19
3.4	A $\beta\beta 0\nu$ event (at left) and a single electron background event (at right). Both events were simulated in Monte Carlo at 15 bar gas pressure [26]. . . . .	23
3.5	The effect of 2 mm (at the centre images) and 10 mm (at the right) diffusion where the details lost at the diffusion can be seen against the 'true' track [29]. . . . .	28
3.6	Reduced EL yield obtained for 5.9 keV x-rays, $Y/p$ , as a function of the reduced electric field, $E/p$ , for different types and concentrations of molecular gases added to pure xenon: (a) CO <sub>2</sub> ; (b) CH <sub>4</sub> ; (c) CF <sub>4</sub> . Total pressures of 1.13, 1.25 and 1.24 bar were used, for Xe-CO <sub>2</sub> , Xe-CH <sub>4</sub> and Xe-CF <sub>4</sub> mixtures, respectively. Solid lines show linear fits to the data, while dashed lines are simulation values obtained with the code developed in [31]. Results taken from [32]. . . . .	31
3.7	Energy resolution extrapolated for NEXT-100 for the $\beta\beta 0\nu$ energy as function of 3D diffusion for the labelled additive concentrations, with a drift reduced electric field of 20 V/cm/bar and and EL reduced electric field of 2.5 keV/cm/bar [106]. . . . .	33
5.1	Left: Cross section of electron-xenon and electron-helium as function of electron energy [128]. Right: Transverse diffusion coefficient as function of helium concentration in xenon-helium admixtures [34]. . . . .	47

5.2	Left: Dependence of the reduced transverse diffusion coefficient on helium concentration predicted with Magboltz simulations. The line represents the value from the simulation and the shaded region is the error in the simulation. Right: Extrapolated transverse diffusion in pure xenon, compared to experimental data from NEXT-NEW TPC [35]. . . . .	47
5.3	Longitudinal diffusion as function of the applied electric field for different concentrations of helium in xenon from [34] simulations (top) and the respective experimental results from [35] (bottom). . . . .	49
5.4	Drift velocity as function of helium concentration for xenon-helium mixtures for different electric fields [34]. . . . .	50
5.5	Results obtained from simulation for the reduced electroluminescence yield as function of the applied reduced electric field [34]. . . . .	51
6.1	Schematic of a GPSC equipped with a large avalanche photodiode (LAAPD). . . . .	53
6.2	Experimental setup layout . . . . .	55
6.3	Pulse-height distribution for 5.9 keV x-rays absorbed in the GPSC active volume filled with Xe-15%He, for a reduced electric field of 2.4 kV/cm/bar. . . . .	57
6.4	Typical waveform obtained with 5.9 keV x-rays. . . . .	60
6.5	Example of a rejected waveform that significantly deviates in time from the trigger instant. . . . .	60
7.1	EL yield ( $Y/p$ ) in arbitrary units for pure xenon, normalised by pressure, as a function of reduced electric field ( $E/p$ ) applied to the scintillation region achieved for several runs with different LAAPD operation conditions. . . . .	64
7.2	EL yield ( $Y/p$ ) as a function of reduced electric field ( $E/p$ ) applied to the scintillation region obtained with pure Xe in different days at different room temperatures. Absolute values were obtained from the normalisation procedure described in the text above. . . . .	65
7.3	Reduced EL yield ( $Y/p$ ) for pure xenon as a function of reduced electric field ( $E/p$ ) applied to the scintillation region obtained from different days (with different room temperatures and leak currents). a) Data without leak current correction. b) The same curves with data corrected for leak current. . . . .	66
7.4	Energy resolution as a function of $E/p$ , obtained for pure xenon.	67

7.5	$R_E^2$ as a function of $1/A$ , obtained with pure xenon, for runs performed in different days. The solid line represents the linear fit to the data points in blue, with the remaining points excluded from the fit. . . . .	68
8.1	Reduced EL yield as function of $E/p$ in the scintillation region for pure Xe and for the different Xe-He mixtures studied in the present work. The solid and dashed lines correspond to linear fits performed on the experimental and simulation data from [34], respectively. The full data set is depicted on the top plot. The different He concentrations are separated in the 4 bottom plots for readability purposes. . . . .	72
8.2	Experimental and simulated reduced EL yield as a function of He concentration for an $E/p$ of 2.5 kV/cm/bar. Solid curves (2-degree polynomial fit) serve only to guide the eye. . . . .	73
8.3	Energy resolution as function of the reduced electric field in the scintillation region, obtained for pure Xe and several Xe-He mixtures. Solid curves serve only to guide the eye. . . . .	74
8.4	Energy resolution as function of $E/p$ in the scintillation region, obtained for pure Xe and for the several Xe-He mixtures, with the values of each run corrected for the total pressure. . . . .	75
8.5	The square of the energy resolution, $R_E^2$ , as function of the peak centroid's inverse of 5.9 keV pulse height distribution for Xe-He mixtures. The solid lines are linear fits to the selected data points (blue circles). a) 10% He, b) 15% He, c) 20% He, d) 30% He. . . . .	77
9.1	Magboltz simulation [129] of the drift velocity and $D_L$ for pure xenon and for a mixture of 30%-He, both with a total a pressure of $\sim 1.1$ bar [136]. . . . .	80
9.2	(top): Secondary scintillation pulse observed in the oscilloscope, after averaging 512 events produced by 5.9 keV x-rays in the gas volume for Xe-20%He mixture. (bottom): baseline zoom of the waveform presented in a). . . . .	81
9.3	Projection of the tracks produced by 100 alpha particles on the yz-plan, obtained from a SRIM simulation for a Xe-30%He mixture. The blue tracks represent the path travelled by alpha particles, starting at the $^{241}\text{Am}$ source, passing through 2 mm of air at 1 bar, 10 $\mu\text{m}$ of aluminium and 6 $\mu\text{m}$ of Melinex, until being fully stopped in the gas mixture, whose end-position is represented by red points. . . . .	83

9.4	Relative energy deposited in the gas volume by alpha particles along the z-axis, obtained from a SRIM simulation, for pure xenon and for a Xe-30%He mixture at 1.1 bar. . . . .	83
9.5	Typical average waveform produced by alpha particles in pure xenon at 1.1 bar, for a mean reduced electric field of 376 V/cm/bar in the drift region, and a reduced electric field of 2.7 kV/cm/bar in the EL region. . . . .	84
9.6	GPSC simulated electric field along the z-axis using the Elmer finite element solver [139, 140]. . . . .	85
9.7	Simulated waveform and average experimental waveform, both obtained for pure xenon at 1.1 bar. . . . .	89
9.8	Electron drift time as a function of voltage differences applied to the drift region, for pure xenon and Xe-30 %He mixture. . . . .	90
9.9	Longitudinal electron cloud size obtained with pure Xe and a Xe-30%He mixture for a wide range of voltages applied across the drift region. The simulated values are shown for several working conditions. . . . .	91

# Bibliography

- [1] D. R. Nygren. Columnar recombination: a tool for nuclear recoil directional sensitivity in a xenon-based direct detection WIMP search. *J. Phys. Conf. Ser.*, 460:012006, 2013.
- [2] G. Mohlabeng, K. Kong, J. Li, A. Para, and J. Yoo. Dark Matter Directionality Revisited with a High Pressure Xenon Gas Detector. *JHEP*, 07:092, 2015.
- [3] N.S. Phan, R.J. Lauer, E.R. Lee, D. Loomba, J.A.J. Matthews, and E.H. Miller. GEM-based TPC with CCD Imaging for Directional Dark Matter Detection. *Astropart. Phys.*, 84:82–96, 2016.
- [4] NEXT Collaboration, J. Martín-Albo, et al. Sensitivity of NEXT-100 to Neutrinoless Double Beta Decay. *JHEP*, 05:159, 2016.
- [5] K. Nakamura et al. AXEL—a high pressure xenon gas TPC for neutrinoless double beta decay search. *Nucl. Instrum. Meth. A*, 845:394–397, 2017.
- [6] M. Redshaw, E. Wingfield, J. McDaniel, and E.G. Myers. Mass and Double-Beta-Decay  $Q$  Value of  $^{136}\text{Xe}$ . *Phys. Rev. Lett.*, 98:053003, 2007.
- [7] NEXT Collaboration, J. Martín-Albo, and J.J. Gómez-Cadenas. Status and physics potential of NEXT-100. *J. Phys. Conf. Ser.*, 460:012010, 2013.
- [8] NEXT Collaboration, J.J. Gomez-Cadenas, et al. Present status and future perspectives of the NEXT experiment. *Adv. High Energy Phys.*, 2014:907067, 2014.
- [9] Yu Gavriluk, A. Gangapshev, V. Kazalov, V. Kuzminov, S. Panasenko, S. Ratkevich, D. Tekueva, and S. Yakimenko. Results of In-Depth Analysis of Data Obtained in the Experimental Search for  $2\text{K}(2\nu)$ -Capture in  $^{78}\text{Kr}$ . *Physics of Particles and Nuclei*, 49:540–546, 07 2018.
- [10] D. Gonzalez-Diaz, F. Monrabal, and S. Murphy. Gaseous and dual-phase time projection chambers for imaging rare processes. *Nucl. Instrum. Meth. A*, 878:200–255, 2018.

- [11] NEXT Collaboration, Diego González-Díaz, et al. Accurate  $\gamma$  and MeV-electron track reconstruction with an ultra-low diffusion Xenon/TMA TPC at 10 atm. *Nucl. Instrum. Meth. A*, 804:8–24, 2015.
- [12] NEXT Collaboration, D. Lorca, et al. Characterisation of NEXT-DEMO using xenon  $K_{\alpha}$  X-rays. *JINST*, 9(10):P10007, 2014.
- [13] J. Renner et al. Energy calibration of the NEXT-White detector with 1% resolution near  $Q_{\beta\beta}$  of  $^{136}\text{Xe}$ . *Journal of High Energy Physics*, 10(10):230, Oct 2019.
- [14] L.M.P. Fernandes, E.D.C. Freitas, M. Ball, J.J. Gomez-Cadenas, C.M.B. Monteiro, N. Yahlali, D. Nygren, and J.M.F.dos Santos. Primary and secondary scintillation measurements in a xenon Gas Proportional Scintillation Counter. *JINST*, 5:P09006, 2010. [Erratum: *JINST* 5, A12001 (2010)].
- [15] C. Balan, E.D.C. Freitas, T. Papaevangelou, I. Giomataris, H.Natal da Luz, C.M.B. Monteiro, and J.M.F.dos Santos. Micromegas operation in high pressure xenon: Charge and scintillation readout. *JINST*, 6:P02006, 2011.
- [16] NEXT Collaboration, V. Alvarez, et al. Near-Intrinsic Energy Resolution for 30 to 662 keV Gamma Rays in a High Pressure Xenon Electroluminescent TPC. *Nucl. Instrum. Meth. A*, 708:101–114, 2013.
- [17] NEXT Collaboration, L. Serra, D. Lorca, J. Martin-Albo, M. Sorel, and J.J. Gomez-Cadenas. Latest results of NEXT-DEMO, the prototype of the NEXT 100 double beta decay experiment. In *37th International Conference on High Energy Physics*, 10 2014.
- [18] C.M.B. Monteiro, L.M.P. Fernandes, J.A.M. Lopes, L.C.C. Coelho, J.F.C.A. Veloso, J.M.F. dos Santos, K. Giboni, and E. Aprile. Secondary scintillation yield in pure xenon. *Journal of Instrumentation*, 05(5):05001, May 2007.
- [19] C.M.B. Monteiro, J.A.M. Lopes, J.F.C.A. Veloso, and J.M.F. dos Santos. Secondary scintillation yield in pure argon. *Physics Letters B*, 668(3):167 – 170, 2008.
- [20] C.A.B. Oliveira et al. A simulation toolkit for electroluminescence assessment in rare event experiments. *Phys. Lett. B*, 703:217–222, 2011.
- [21] E.D.C. Freitas, C.M.B. Monteiro, M. Ball, J.J. Gomez-Cadenas, J.A.M. Lopes, T. Lux, F. Sanchez, and J.M.F. dos Santos. Secondary scintillation

- yield in high-pressure xenon gas for neutrinoless double beta decay ( $0\nu\beta\beta$ ) search. *Phys. Lett. B*, 684:205–210, 2010.
- [22] C.M.B. Monteiro, A.S. Conceicao, F.D. Amaro, J.M. Maia, A.C.S.S.M. Bento, L.F.R. Ferreira, J.F.C.A. Veloso, J.M.F. dos Santos, A. Breskin, and R. Chechik. Secondary scintillation yield from gaseous micropattern electron multipliers in direct dark matter detection. *Phys. Lett. B*, 677:133–138, 2009.
- [23] C.M.B. Monteiro, L.M.P. Fernandes, J.F.C.A. Veloso, C.A.B. Oliveira, and J.M.F. dos Santos. Secondary scintillation yield from GEM and THGEM gaseous electron multipliers for direct dark matter search. *Physics Letters B*, 714(1):18–23, 2012.
- [24] J. M. F. dos Santos, J. A. M. Lopes, J. F. C. A. Veloso, P. C. P. S. Simões, T. H. V. T. Dias, F. P. Santos, P. J. B. M. Rachinhas, L. F. Requicha Ferreira, and C. A. N. Conde. Development of portable gas proportional scintillation counters for x-ray spectrometry. *X-Ray Spectrometry*, 30(6):373–381, 2001.
- [25] C.M.B. Monteiro, L.M.P. Fernandes, J.F.C.A. Veloso, and J.M.F. dos Santos. Secondary scintillation readout from GEM and THGEM with a large area avalanche photodiode. *Journal of Instrumentation*, 7(06):P06012, jun 2012.
- [26] NEXT Collaboration, P. Ferrario, et al. First proof of topological signature in the high pressure xenon gas TPC with electroluminescence amplification for the NEXT experiment. *JHEP*, 01:104, 2016.
- [27] NEXT Collaboration, J. Renner, et al. Background rejection in NEXT using deep neural networks. *JINST*, 12(01):T01004, 2017.
- [28] NEXT Collaboration, F. Monrabal, et al. The Next White (NEW) Detector. *JINST*, 13(12):P12010, 2018.
- [29] C.D.R. Azevedo, L.M.P. Fernandes, E.D.C. Freitas, D. Gonzalez-Diaz, F. Monrabal, C.M.B. Monteiro, J. M. F. dos Santos, J.F.C.A. Veloso, and J. J Gomez-Cadenas. An homeopathic cure to pure Xenon large diffusion. *JINST*, 11(02):C02007, 2016.
- [30] NEXT Collaboration, C.A.O. Henriques, et al. Secondary scintillation yield of xenon with sub-percent levels of CO<sub>2</sub> additive for rare-event detection. *Phys. Lett. B*, 773:663–671, 2017.
- [31] C.D.R. Azevedo et al. Microscopic simulation of xenon-based optical TPCs in the presence of molecular additives. *Nucl. Instrum. Meth. A*, 877:157–172, 2018.

- [32] NEXT Collaboration, C.A.O. Henriques, et al. Electroluminescence TPCs at the Thermal Diffusion Limit. *JHEP*, 01:027, 2019.
- [33] R.C. Lanza, W. Rideout, F. Fahey, and R.E. Zimmerman. Gas Scintillators for Imaging of Low Energy Isotopes. *IEEE Transactions on Nuclear Science*, 34(1):406–409, 1987.
- [34] R. Felkai et al. Helium–Xenon mixtures to improve the topological signature in high pressure gas xenon TPCs. *Nucl. Instrum. Meth. A*, 905:82–90, 2018.
- [35] NEXT Collaboration, A.D. McDonald, et al. Electron Drift and Longitudinal Diffusion in High Pressure Xenon-Helium Gas Mixtures. *JINST*, 14(08):P08009, 2019.
- [36] Particle Data Group Collaboration, J. Beringer, et al. Review of Particle Physics (RPP). *Phys. Rev. D*, 86:010001, 2012.
- [37] M.C. Gonzalez-Garcia and Michele Maltoni. Phenomenology with Massive Neutrinos. *Phys. Rept.*, 460:1–129, 2008.
- [38] P. Hernandez. Neutrino physics. In *5th CERN - Latin American School of High-Energy Physics*, volume CERN-210-001, pages 229–278, 10 2010.
- [39] M. Fukugita and T. Yanagida. Baryogenesis Without Grand Unification. *Phys. Lett. B*, 174:45–47, 1986.
- [40] Sacha Davidson, Enrico Nardi, and Yosef Nir. Leptogenesis. *Phys. Rept.*, 466:105–177, 2008.
- [41] J.J. Gomez-Cadenas, J. Martin-Albo, M. Mezzetto, F. Monrabal, and M. Sorel. The Search for neutrinoless double beta decay. *Riv. Nuovo Cim.*, 35(2):29–98, 2012.
- [42] J.J. Gomez-Cadenas, J. Martin-Albo, M. Sorel, P. Ferrario, F. Monrabal, J. Munoz-Vidal, P. Novella, and A. Poves. Sense and sensitivity of double beta decay experiments. *JCAP*, 06:007, 2011.
- [43] NEXT Collaboration and P. Ferrario. NEXT-DEMO: a prototype for the NEXT experiment. *JINST*, 7:C11013, 2012.
- [44] H.V. Klapdor-Kleingrothaus et al. Latest results from the Heidelberg-Moscow double beta decay experiment. *Eur. Phys. J. A*, 12:147–154, 2001.
- [45] J. Engel and P. Vogel. Viewpoint: The Hunt for No Neutrinos. *Physical Review Letters*, 11(30), 2018.

- [46] NEMO-3 Collaboration, R. Arnold, et al. Results of the search for neutrinoless double- $\beta$  decay in  $^{100}\text{Mo}$  with the NEMO-3 experiment. *Phys. Rev. D*, 92(7):072011, 2015.
- [47] SuperNEMO Collaboration, R. Arnold, et al. Probing New Physics Models of Neutrinoless Double Beta Decay with SuperNEMO. *Eur. Phys. J. C*, 70:927–943, 2010.
- [48] CUORE Collaboration, D.R. Artusa, et al. Exploring the Neutrinoless Double Beta Decay in the Inverted Neutrino Hierarchy with Bolometric Detectors. *Eur. Phys. J. C*, 74(10):3096, 2014.
- [49] F. Bellini. The search for Majorana neutrinos with neutrinoless double beta decays: From CUORICINO to LUCIFER experiment. *AIP Conference Proceedings*, 1498(1):237–245, 2012.
- [50] N. D. Khanbekov. AMoRE: Collaboration for searches for the neutrinoless double-beta decay of the isotope of  $^{100}\text{Mo}$  with the aid of  $^{40}\text{Ca}^{100}\text{MoO}_4$  as a cryogenic scintillation detector. *Physics of Atomic Nuclei*, 76(9):1086–1089, 2013.
- [51] K. Zuber. COBRA: Double beta decay searches using CdTe detectors. *Phys. Lett. B*, 519:1–7, 2001.
- [52] COBRA Collaboration, T. Bloxham, et al. First results on double  $\beta$ -decay modes of Cd, Te, and Zn Isotopes. *Phys. Rev. C*, 76:025501, 2007.
- [53] C. Arnaboldi, F.T. Avignone III, J. Beeman, M. Barucci, et al. CUORE: a cryogenic underground observatory for rare events. *Nuclear Instruments and Methods in Physics Research Section A: Accelerators, Spectrometers, Detectors and Associated Equipment*, 518(3):775 – 798, 2004.
- [54] C. Brofferio, O. Cremonesi, and S. Dell’Oro. Neutrinoless Double Beta Decay Experiments With  $\text{TeO}_2$  Low-Temperature Detectors. *Front. in Phys.*, 7:86, 2019.
- [55] E. Fiorini and T.O. Niinikoski. Low Temperature Calorimetry for Rare Decays. *Nucl. Instrum. Meth. A*, 224:83, 1984.
- [56] C. Enss and Dan Mccammon. Physical Principles of Low Temperature Detectors: Ultimate Performance Limits and Current Detector Capabilities. *Journal of Low Temperature Physics*, 151:5–24, 04 2008.
- [57] C. Arnaboldi et al. Production of high purity  $\text{TeO}_2$  single crystals for the study of neutrinoless double beta decay. *J. Cryst. Growth*, 312(20):2999–3008, 2010.

- [58] CUORE Collaboration, D.Q. Adams, et al. Improved Limit on Neutrinoless Double-Beta Decay in  $^{130}\text{Te}$  with CUORE. *Phys. Rev. Lett.*, 124(12):122501, 2020.
- [59] SNO+ Collaboration, S. Andringa, et al. Current Status and Future Prospects of the SNO+ Experiment. *Adv. High Energy Phys.*, 2016:6194250, 2016.
- [60] S. Andringa. SNO+ present status and prospects. *Journal of Physics: Conference Series*, 1137:012053, jan 2019.
- [61] SNO+ Collaboration and V. Fischer. Search for neutrinoless double-beta decay with SNO+. In *13th Conference on the Intersections of Particle and Nuclear Physics*, 9 2018.
- [62] SNO+ Collaboration and Josephine Paton. Neutrinoless Double Beta Decay in the SNO+ Experiment. In *Prospects in Neutrino Physics*, 3 2019.
- [63] KamLAND-Zen Collaboration, A. Gando, et al. Measurement of the double- $\beta$  decay half-life of  $^{136}\text{Xe}$  with the KamLAND-Zen experiment. *Phys. Rev. C*, 85:045504, 2012.
- [64] KamLAND-Zen Collaboration and Yoshihito Gando. First results of KamLAND-Zen 800. *J. Phys. Conf. Ser.*, 1468(1):012142, 2020.
- [65] KamLAND-Zen Collaboration, K. Asakura, et al. Results from KamLAND-Zen. *AIP Conf. Proc.*, 1666(1):170003, 2015.
- [66] KamLAND-Zen Collaboration, A. Gando, et al. Limit on Neutrinoless  $\beta\beta$  Decay of  $^{136}\text{Xe}$  from the First Phase of KamLAND-Zen and Comparison with the Positive Claim in  $^{76}\text{Ge}$ . *Phys. Rev. Lett.*, 110(6):062502, 2013.
- [67] EXO-200 Collaboration, J. B. Albert, G. Anton, I. Badhrees, et al. Search for Neutrinoless Double-Beta Decay with the Upgraded EXO-200 Detector. *Phys. Rev. Lett.*, 120:072701, Feb 2018.
- [68] nEXO Collaboration, J.B. Albert, et al. Sensitivity and Discovery Potential of nEXO to Neutrinoless Double Beta Decay. *Phys. Rev. C*, 97(6):065503, 2018.
- [69] GERDA Collaboration, M. Agostini, et al. Final Results of GERDA on the Search for Neutrinoless Double- $\beta$  Decay. *Submitted on 13 Sep 2020 arXiv e-prints*, 9 2020.

- [70] GERDA Collaboration, M. Agostini, et al. Improved Limit on Neutrinoless Double- $\beta$  Decay of  $^{76}\text{Ge}$  from GERDA Phase II. *Phys. Rev. Lett.*, 120(13):132503, 2018.
- [71] N. Abgrall et al. The MAJORANA DEMONSTRATOR Neutrinoless Double-Beta Decay Experiment. *Advances in High Energy Physics*, 2014:1–18, 2014.
- [72] Majorana Collaboration, S.I. Alvis, et al. A Search for Neutrinoless Double-Beta Decay in  $^{76}\text{Ge}$  with 26 kg-yr of Exposure from the MAJORANA DEMONSTRATOR. *Phys. Rev. C*, 100(2):025501, 2019.
- [73] I.J. Arnquist et al. The Majorana Demonstrator’s Search for Double-Beta Decay of  $^{76}\text{Ge}$  to Excited States of  $^{76}\text{Se}$ . *Submitted on 13 Aug 2020 arXiv e-prints*, 8 2020.
- [74] J. Hyvärinen and J. Suhonen. Neutrinoless  $\beta\beta$  decays to excited  $0^+$  states and the Majorana-neutrino mass. *Phys. Rev. C*, 93(6):1–15, 2016.
- [75] J. Menendez, A. Poves, E. Caurier, and F. Nowacki. Disassembling the nuclear matrix elements of the neutrinoless  $\beta\beta$  decay. *Nuclear Physics A*, 818(3):139 – 151, 2009.
- [76] Hao Qiao, Chunyu Lu, Xun Chen, Ke Han, Xiangdong Ji, and Siguang Wang. Signal-background discrimination with convolutional neural networks in the PandaX-III experiment using MC simulation. *Sci. China Phys. Mech. Astron.*, 61(10):101007, 2018.
- [77] J.J. Gomez-Cadenas. The NEXT experiment. *Nuclear and Particle Physics Proceedings*, 273-275:1732 – 1739, 2016. 37th International Conference on High Energy Physics (ICHEP).
- [78] NEXT Collaboration, J.J. Gomez-Cadenas, J. Martin-Albo, and F. Monrabal. NEXT, high-pressure xenon gas experiments for ultimate sensitivity to Majorana neutrinos. *JINST*, 7:C11007, 2012.
- [79] NEXT Collaboration, V. Alvarez, et al. The NEXT-100 experiment for neutrinoless double beta decay searches (Conceptual Design Report). *arXiv e-prints*, page arXiv:1106.3630, 6 2011.
- [80] A. Herzenberg. Attachment of Slow Electrons to Oxygen Molecules. *The Journal of Chemical Physics*, 51(11):4942–4950, 1969.
- [81] M. Huk, P. Igo-Kemenes, and A. Wagner. Electron attachment to oxygen, water, and methanol, in various drift chambers gas mixtures.

*Nuclear Instruments and Methods in Physics Research Section A: Accelerators, Spectrometers, Detectors and Associated Equipment*, 267(1):107–119, 1988.

- [82] NEXT Collaboration and Paola Ferrario. The NEXT double beta decay experiment. *PoS*, EPS-HEP2017:105, 2017.
- [83] D. Nygren. High pressure xenon gas electroluminescent TPC for  $0\nu\beta\beta$  decay search. *Nuclear Instruments and Methods in Physics Research A*, 603(3):337–348, 2009.
- [84] NEXT Collaboration, C.A.O. Henriques, et al. First evidence of neutral Bremsstrahlung emission in xenon. *Submitted to Phys. Rev. X*, 2020.
- [85] A. Buzulutskov, E. Shemyakina, A. Bondar, A. Dolgov, E. Frolov, V. Nosov, V. Oleynikov, L. Shekhtman, and A. Sokolov. Revealing neutral bremsstrahlung in two-phase argon electroluminescence. *Astropart. Phys.*, 103:29–40, 2018.
- [86] NEXT Collaboration and F. Monrabal. The NEXT experiment to search for the neutrinoless double beta decay of Xe-136. *PoS*, ICHEP2016:497, 2017.
- [87] NEXT Collaboration, P. Novella, et al. Radiogenic Backgrounds in the NEXT Double Beta Decay Experiment. *JHEP*, 10:051, 2019.
- [88] NEXT Collaboration, P. Novella, et al. Measurement of radon-induced backgrounds in the NEXT double beta decay experiment. *JHEP*, 10:112, 2018.
- [89] NEXT Collaboration, V. Álvarez, et al. Operation and first results of the NEXT-DEMO prototype using a silicon photomultiplier tracking array. *JINST*, 8:P09011, 2013.
- [90] R. Luscher et al. Search for  $\beta\beta$  decay in Xe-136: New results from the Gotthard experiment. *Phys. Lett. B*, 434:407–414, 1998.
- [91] NEXT Collaboration, V. Alvarez, et al. NEXT-100 Technical Design Report (TDR): Executive Summary. *JINST*, 7:T06001, 2012.
- [92] V. Álvarez et al. Initial results of NEXT-DEMO, a large-scale prototype of the NEXT-100 experiment. *Journal of Instrumentation*, 8(4):P04002, April 2013.
- [93] NEXT Collaboration, J. Renner, et al. Initial results on energy resolution of the NEXT-White detector. *JINST*, 13(10):P10020, 2018.

- [94] NEXT Collaboration, P. Ferrario, et al. Demonstration of the event identification capabilities of the NEXT-White detector. *JHEP*, 10:052, 2019.
- [95] NEXT Collaboration, A. Simón, et al. Electron drift properties in high pressure gaseous xenon. *JINST*, 13(07):P07013, 2018.
- [96] V. Palladino and B. Sadoulet. Application of Classical Theory of Electrons in Gases to Drift Proportional Chambers. *Nucl. Instrum. Meth.*, 128:323, 1975.
- [97] L. G. H. Huxley and R. W. Crompton. *Fundamental Principles of Optical Lithography*. Wiley, New York, 1974.
- [98] P. Segur, M. Yousfi, M. H. Kadri, and M. C. Bordage. A survey of the numerical methods currently in use to describe the motion of an electron swarm in a weakly ionized gas. *Transport Theory and Statistical Physics*, 15(6-7):705–757, 1986.
- [99] Thomas Klikauer. Reflections on Phishing for Phools – The Economics of Manipulation and Deception. *tripleC: Communication, Capitalism & Critique.*, 14:260–264, 04 2016.
- [100] R.E. Robson, M. Hildebrandt, and B. Schmidt. Electron transport theory in gases: Must it be so difficult? *Nucl. Instrum. Meth. A*, 394:74–86, 1997.
- [101] T. Takahashi, S. Himi, M. Suzuki, J. Ruan(Gen), and S. Kubota. Emission spectra from Ar-Xe, Ar-Kr, Ar-N<sub>2</sub>, Ar-CH<sub>4</sub>, Ar-CO<sub>2</sub> and Xe-N<sub>2</sub> gas scintillation proportional counters. *Nuclear Instruments and Methods in Physics Research*, 205(3):591 – 596, 1983.
- [102] F. P. Santos, T. H. V. T. Dias, A. D. Stauffer, and C. A. N. Conde. Three-dimensional Monte Carlo calculation of the VUV electroluminescence and other electron transport parameters in xenon. *Journal of Physics D: Applied Physics*, 27(1):42–48, jan 1994.
- [103] Rob Veenhof. Choosing a gas mixture for the ALICE TPC. *ALICE Internal Note*, 2003.
- [104] K. N. Pushkin, N. Hasebe, S. Kobayashi, C. Tezuka, M. Mimura, T. Hosojima, M. N. Kobayashi, T. Doke, M. Miyajima, T. Miyachi, E. Shibamura, S. E. Ulin, and V. V. Dmitrenko. Scintillation yield in high pressure xenon and xenon doped with methane. In *IEEE Symposium Conference Record Nuclear Science 2004.*, volume 1, pages 550 – 553 Vol. 1, 11 2004.

- [105] L.G. Christophorou, D.L. McCorkle, D.V. Maxey, and J.G. Carter. Fast gas mixtures for gas-filled particle detectors. *Nuclear Instruments and Methods*, 163(1):141 – 149, 1979.
- [106] C. A. O. Henriques. *Studies of xenon mixtures with molecular additives for the NEXT electroluminescence TPC*. PhD thesis, University of Coimbra, 04 2019.
- [107] Y. Tanaka, A. S. Jursa, and F. J. LeBlanc. Continuous Emission Spectra of Rare Gases in the Vacuum Ultraviolet Region. II. Neon and Helium. *J. Opt. Soc. Am.*, 48(5):304–308, May 1955.
- [108] M. Suzuki and S. Kubota. Mechanism of proportional scintillation in argon, krypton and xenon. *Nuclear Instruments and Methods*, 164(1):197 – 199, 1979.
- [109] J. W. Keto, R. E. Gleason, and G. K. Walters. Production Mechanisms and Radiative Lifetimes of Argon and Xenon Molecules Emitting in the Ultraviolet. *Phys. Rev. Lett.*, 33:1365–1368, Dec 1974.
- [110] C.A.B. Oliveira, V. Gehman, A. Goldschmidt, D. Nygren, and J. Renner. Measurements of Charge and Light in Pure High Pressure Xe towards the Study of Xe+TMA Mixtures with Dark Matter Directionality Sensitivity and Supra-intrinsic Energy Resolution for  $0\nu\beta\beta$  Decay Searches. *Physics Procedia*, 61:742 – 749, 2015. 13th International Conference on Topics in Astroparticle and Underground Physics, TAUP 2013.
- [111] M. Suzuki, J. Ruan(Gen), and S. Kubota. Time dependence of the recombination luminescence from high-pressure argon, krypton and xenon excited by alpha particles. *Nuclear Instruments and Methods in Physics Research*, 192(2):565 – 574, 1982.
- [112] F.L.R. Vinagre and Carlos Conde. A technique for the absolute measurement of the w-value for X-rays in counting gases. *Nuclear Instruments and Methods in Physics Research Section A: Accelerators, Spectrometers, Detectors and Associated Equipment*, 450:365–372, 08 2000.
- [113] S.J.C. do Carmo, F.I.J.M. Borges, F. L. R. Vinagre, and C. Nieto Conde. Experimental Study of the w-Values and Fano Factors of Gaseous Xenon and Ar-Xe Mixtures for X-Rays. *IEEE Transactions on Nuclear Science*, 55(5):2637–2642, 2008.
- [114] T.H.V.T. Dias, J.M.F. dos Santos, P.J.B.M. Rachinhas, F.P. Santos, C.A.N. Conde, and A.D. Stauffer. Full-energy absorption of x-ray energies

- near the Xe L- and K-photoionization thresholds in xenon gas detectors: Simulation and experimental results. *Journal of Applied Physics*, 82(6):2742–2753, 1997.
- [115] NEXT Collaboration, L. Serra, et al. An improved measurement of electron-ion recombination in high-pressure xenon gas. *JINST*, 10(03):P03025, 2015.
- [116] P. Lindblom and O. Solin. Atomic near-infrared noble gas scintillations I: Optical spectra. *Nuclear Instruments and Methods in Physics Research Section A: Accelerators, Spectrometers, Detectors and Associated Equipment*, 268(1):204 – 208, 1988.
- [117] M. S. S. C. P. Leite. Radioluminescence of rare gases. *Port. Phys*, 11:53–73, 1980.
- [118] A. Policarpo. Light Production and Gaseous Detectors. *Physica Scripta*, 23(4A):539–549, apr 1981.
- [119] A. Bolotnikov and B. Ramsey. The spectroscopic properties of high-pressure xenon. *Nuclear Instruments and Methods in Physics Research Section A: Accelerators, Spectrometers, Detectors and Associated Equipment*, 396(3):360 – 370, 1997.
- [120] C.A.B. Oliveira, M. Sorel, J. Martin-Albo, J.J. Gomez-Cadenas, A.L. Ferreira, and J.F.C.A. Veloso. Energy Resolution studies for NEXT. *JINST*, 6:P05007, 2011.
- [121] T. H. V. T. Dias, F. P. Santos, A. D. Stauffer, and C. A. N. Conde. Monte Carlo simulation of x-ray absorption and electron drift in gaseous xenon. *Phys. Rev. A*, 48:2887–2902, Oct 1993.
- [122] M. Moszynski, M. Szawłowski, M. Kapusta, M. Balcerzyk, and D. Wolski. Large area avalanche photodiodes in X-rays and light detection. *Nuclear Science, IEEE Transactions on*, 1:1297 – 1302, 09 2000.
- [123] Glenn F. Knoll. *Radiation Detection and Measurement, 3rd ed.* John Wiley and Sons, New York, 3rd edition edition, 2000.
- [124] M. Moszynski, M. Szawłowski, M. Kapusta, and M. Balcerzyk. Large area avalanche photodiodes in scintillation and X-rays detection. *Nuclear Instruments and Methods in Physics Research Section A: Accelerators, Spectrometers, Detectors and Associated Equipment*, 485:504–521, 01 2000.
- [125] Advanced Photonix Inc. Non-Cooled Large Area DUV Silicon Avalanche Photodiode, 2012.

- [126] J. Matias-Lopes, J.M.F. Santos, R.E. Morgado, and C. Conde. A xenon gas proportional scintillation counter with a UV - Sensitive large-area avalanche photodiode. In *2000 IEEE Nuclear Science Symposium. Conference Record (Cat. No.00CH37149)*, volume 1, pages 5/72 – 5/76 vol.1, 02 2000.
- [127] Stephen G. Kukulich. Demonstration of the Ramsauer-Townsend Effect in a Xenon Thyatron. *American Journal of Physics*, 36(8):701–703, 1968.
- [128] P. Babington. Interactions of photons and electrons with atoms. *Springer-Verlag Berlin Heidelberg*, 17A:XII, 164, 2000.
- [129] S. Biagi. Magboltz — transport of electrons in gas mixtures. <http://magboltz.web.cern.ch/magboltz/>.
- [130] k. Saito, S Sasaki, H Tawara, T. Sanami, and E. Shibamura. Study of scintillation in helium mixed with xenon to develop thermal neutron detectors. *Nuclear Instruments and Methods in Physics Research Section A: Accelerators, Spectrometers, Detectors and Associated Equipment*, 581(1):119 – 122, 2007. VCI 2007.
- [131] C. Monteiro, J. Matias-Lopes, P. C. Simões, J.M.F. Santos, and C Conde. An argon gas proportional scintillation counter with UV avalanche photodiode scintillation readout. *IEEE Trans Nucl. Sci.*, 1:5/67–5/71 vol.1, 01 2000.
- [132] L.M.P. Fernandes et al. Characterization of large area avalanche photodiodes in X-ray and VUV-light detection. *Journal of Instrumentation*, 08(8):08005, August 2007.
- [133] D.F. Anderson, T.T. Hamilton, and R. Novick W.H.-M. Ku. A large area gas scintillation proportional counter. *Nuclear Instruments and Methods*, 163(1):125–134, 1979.
- [134] T.Z. Kowalski, A. Smith, and A. Peacock. Fano factor implications from gas scintillation proportional counter measurements. *Nuclear Instruments and Methods in Physics Research Section A: Accelerators, Spectrometers, Detectors and Associated Equipment*, 279(3):567 – 572, 1989.
- [135] F. I. G. M. Borges and C. A. N. Conde. Electron transport and grid transmission in noble gas radiation detectors. in *Proc. SASP'94*, Eds. T. D. Mark, R. Schrittwiser, and D. Smitt. *Intermoos, Austria: Institute für Ionen Physik, Universität Innsbruck, Mar.*, 20(24):436–437, 1994.

- [136] C. Azevedo, C. A. O. Henriques, and Damien. Magboltz simulation of the drift velocity and DL for pure xenon and the mixture of Xe-He30%. *Private Communication*, 2019.
- [137] S. do Carmo, F.I.G.M. Borges, F. Santos, T. Dias, and Carlos Conde. Absolute primary scintillation yield of gaseous xenon under low drift electric fields for 5.9 keV X-rays. *Journal of Instrumentation*, 3:P07004, 07 2008.
- [138] J. F. Ziegler, M. D. Ziegler, and J. P. Biersack. SRIM - The Stopping and Range of Ions in Matter. *Nuclear Instruments and Methods in Physics Section B: Beam Interactions with Materials and Atoms, 19th International Conference on Ion Beam Analysis*, 268:1818, 2010.
- [139] CSC Company. Elmer FEM solver. <https://www.csc.fi/web/elmer>.
- [140] P. Silva. GPSC electric field simulation. *Private Communication*, 2019.
- [141] E. Morikawa, R. Reiningger, P. Gürtler, Saile V., and P. Laporte. Argon, krypton, and xenon excimer luminescence: From the dilute gas to the condensed phase. *J. Chem. Phys*, 91(3):1469–1477, aug 1989.
- [142] M. Nebot-Guinot, P. Ferrario, J. Martín-Albo, J. Muñoz Vidal, and J.J. Gómez-Cadenas. Backgrounds and sensitivity of the NEXT double beta decay experiment. *Nuclear and Particle Physics Proceedings*, 273-275:2612 – 2614, 2016. 37th International Conference on High Energy Physics (ICHEP).